# Coupled Field Modeling of Gas Tungsten Arc Welding

Debamoy Sen

Dissertation submitted to the faculty of the
Virginia Polytechnic Institute and State University
in partial fulfillment of the requirements for the degree of

Doctor of Philosophy
In
Mechanical Engineering

Kenneth Ball, co-Chair
Mark Pierson, co-chair
Danesh Tafti
Francine Battaglia
Robert Hendricks

July 3, 2012
Blacksburg, Virginia

**Keywords:** Gas Tungsten Arc Welding, Weld Pool Dynamics, Structural Analysis, Material Modeling, Marangoni Convection, Plasma Induced Shear, Electromagnetic force, Buoyancy, Thermal Stress, Residual Stress

# Coupled Field Modeling of Gas Tungsten Arc Welding

**Debamoy Sen**

## Abstract

Welding is used extensively in aerospace, automotive, chemical, manufacturing, and power-generation industries. Thermally-induced residual stresses due to welding can significantly impair the performance and reliability of welded structures. Numerical simulation of weld pool dynamics is important as experimental measurements of velocities and temperature profiles are difficult due to the small size of the weld pool and the presence of the arc. It is necessary to have an accurate spatial and temporal thermal distribution in the welded structure before stress analysis is performed. Existing research on weld pool dynamics simulation has ignored the effect of fluid flow in the weld pool on the temperature field of the welded joint. Previous research has established that the weld pool depth/width (D/W) ratio and Heat Affected Zone (HAZ) are significantly altered by the weld pool dynamics. Hence, for a more accurate estimation of the thermally-induced stresses it is desired to incorporate the weld pool dynamics into the analysis. Moreover, the effects of microstructure evolution in the HAZ on the mechanical behavior of the structure need to be included in the analysis for better mechanical response prediction. In this study, a 3D-model for the thermo-mechanical analysis of Gas Tungsten Arc (GTA) welding of thin stainless steel butt-joint plates has been developed. The model incorporates the effects of thermal energy redistribution through weld pool dynamics into the structural behavior calculations. Through material modeling the effects of microstructure change/phase transformation are indirectly included in the model. The developed weld pool dynamics model includes the effects of current, arc length, and electrode angle on the heat flux and current density distributions and includes all the major weld pool driving forces are included. The weld D/W predictions are validated with experimental results. They agree well. The effects of welding parameters on the weld D/W ratio are documented. The workpiece deformation and stress distributions are also highlighted. The transverse and longitudinal residual stress distribution plots across the weld bead are provided. The mathematical framework developed here serves as a robust tool for better prediction of weld D/W ratio and thermally-induced stress evolution/distribution in a welded structure by coupling the different fields in a welding process.

# Dedication

*This dissertation is dedicated to my family who has always been incredibly supportive of my educational pursuits. Thank you for believing in me and pushing me to succeed in all my endeavors.*

# Acknowledgements

First and foremost I would like to express my gratitude to my advisors, Dr. Kenneth Ball and Dr. Mark Pierson, for their guidance, support, and motivation throughout my doctoral study. I could not have asked for better advisors supervising my entirely enjoyable and successful graduate career. They have always been available for guidance as well as pushing me forward in research.

I would like to express my deep appreciation to the other members of my committee, Dr. Danesh Tafti, Dr. Francine Battaglia and Dr. Robert Hendricks for their valuable advice and comments, which helped guide the direction of my work. I would also like to acknowledge the support of our research sponsor: Center for Advanced Engineering Research, Lynchburg, Virginia.

Finally, I owe thanks to my parents who instilled in me an indelible love for knowledge, my brother, Anandamoy and sister-in-law, Nabanita who were the driving force behind my academic pursuits, and all members of my family, especially Pubali for her constant support.

# Table of Contents

# List of Figures

# List of Tables

# Chapter 1

---

# Introduction

Welding is used extensively in aerospace, automotive, chemical, manufacturing, electronic, and power-generation industries. Welded structures are an essential part of many buildings, bridges, ships, pressure vessels, and other engineering structures. The process of welding is an integral manufacturing procedure in many engineering and structural components, having a direct influence on the integrity of the components and their thermal and mechanical behavior during service. Due to the high temperatures introduced during welding and the subsequent cooling of the welded structure, welding can produce undesirable residual stresses and deformations. Thermally-induced residual stresses can have detrimental effects, such as stress corrosion cracking and reduced fatigue strength. Welding is an inherently multi-physics problem, encompassing a large array of physical phenomena - fluid flow in the weld pool, heat flow in the structure, microstructural evolution/phase transformations, thermal stress development, and distortion of the welded structure. Though simulations do not replace experiments, it is pertinent to simulate the process of welding to delineate the underlying physical processes and thereby predict the behavior of the welded structures.

## 1.1 Fusion Welding

Fusion welding is the most commonly used technique in industry today because it is the easiest to learn and offers greater mobility for workers at a job site [1]. In fusion welding, a localized intense heat source is moved along the joint and this result in the melting and subsequent solidification of the adjacent areas of two parts. As the power density of the heat source increases, the heat input to the workpiece that is required for welding decreases. Increasing heat input to workpiece leads to greater damage to the workpiece, including weakening and distortion. Advantages of increasing the power density of the heat source are deeper welds, higher welding speeds, and better weld quality with less damage to the workpiece.

The three major types of fusion welding processes are: (i) Gas welding, (ii) Arc welding, and (iii) High-energy beam welding. Gas welding has low power density of the heat source, thus requiring greater heat input to the workpiece. High-energy beam welding has high power density of the heat source and requires very low heat input to the workpiece. Arc welding heat source characteristics fall intermediate between these two extremes. Arc-welding processes consist of an electrode and a workpiece of opposite polarities. When an arc is struck between these two electrodes, current will flow through the partially ionized gas, and the heat generated in the arc sustains the high temperatures needed to maintain the gas in the partially ionized state. As a result, thermal energy is transferred to the workpiece, causing it to melt; the subsequent solidification of this molten region, termed the weld pool, forms the weldment or actual joint. Two particular arc welding processes are (i) Gas Tungsten Arc (GTA) welding, where the tungsten electrode is non-consumable, and (ii) Gas Metal Arc (GMA) welding, where the electrode is consumable and the molten metal droplets thus produced are used to fill the joint. Though arc welding methods have been in use for decades, there is not much theoretical knowledge about the details of the actual physical processes. Significant empirical experience exists, and simulation tools have been used to examine some of the underlying physics. Most of this expertise and simulation is limited to well-known standard aspects of the arc welding process. However, many applications now are becoming much more complex and require greater insight into the physical processes for better welding parameter selection. It is desired to correlate and optimize the welding parameters to meet the recent challenges in welding: (i) thinner sheets – metal sheets are becoming thinner and thinner, and the goal in the automotive industry is to weld shin sheets down to 0.5 mm thickness, (ii) more materials – aluminum and magnesium are becoming popular in automotive manufacturing and these need to be welded quickly and reliably, (iii) visually perfect weld – manual refinishing operations are expensive and hence strong weld deformation needs to be avoided, and (iv) speed – welding needs to be fast and robust at all times.

### 1.2 Gas Tungsten Arc (GTA) Welding

GTA Welding, also known as Tungsten Inert Gas (TIG) welding, is the most widely used method to join materials in manufacturing industries [1]. Figure 1.1 gives a pictorial

representation of the GTA welding process. The torch holding the tungsten electrode is connected to a shielding gas cylinder as well as one terminal of the power source. The workpiece is connected to the other terminal of the power source. The shielding gas goes through the torch body and is directed by a nozzle toward the weld pool to protect it from air. Figure 1.2 highlights an enlarged view of the welding region.

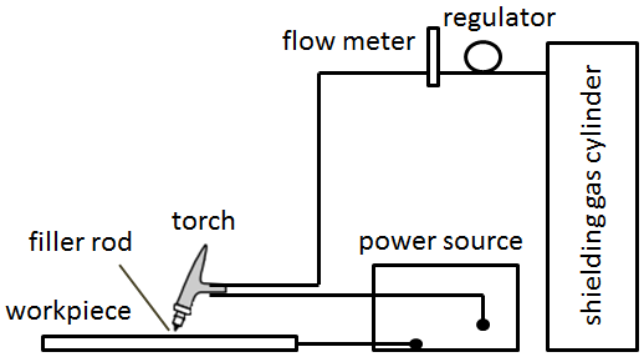


Figure 1.1: GTA welding process setup.

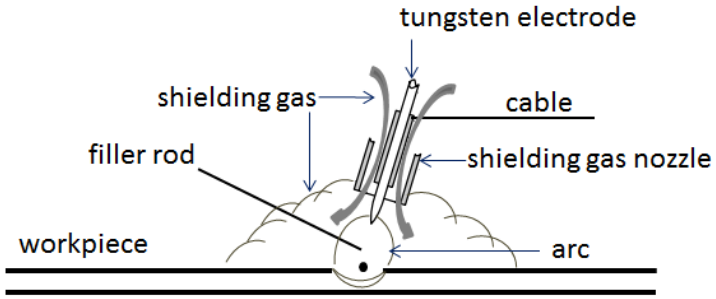


Figure 1.2: Enlarged view of GTA welding region.

Three different polarities can be used in GTA welding: (a) Direct-Current Electrode Negative (DCEN), (b) Direct-Current Electrode Positive (DCEP), and (c) Alternating Current (AC). DCEN is the most common polarity used in the GTA welding process [1]. The electrode is connected to the negative terminal of the power supply. Electrons emitted from the tungsten electrode accelerate while traveling through the arc. When the electron enters the workpiece, an amount of energy, called the work function, associated with the electron is released. In DCEN

configuration, more power is located at the work end of the arc. This leads to a relatively deep and narrow weld. In case of DCEP, the heating effect of electrons is at the tungsten electrode rather than at the workpiece. Consequently, a shallow weld is produced. DCEP however provides a good oxide cleaning action. The AC configuration gives reasonable depth of weld with oxide cleaning action and is used mainly for welding aluminum alloys. Both argon and helium can be used as shielding gases, with argon providing better shielding characteristics – (i) arc initiation is easier as is it easier to ionize, and (ii) argon being heavier than helium provides more effective shielding.

GTA welding is suitable for the joining of thin sections as limited heat inputs are associated with the process. It can also be used to weld butt joints of thin sheets by fusion alone, i.e. without the addition of filler metals. It is a very clean welding process and can be used to weld reactive metals too, like titanium and zirconium. However, it is a slow process and requires the use of filler materials for welding sections thicker than 5mm [1]. It is to be noted that the actual current is also strongly influenced by the material being joined, welding speed etc.

The GTA welding transport processes for the weld pool are: (i) heat and current flux distributions to the weld pool, (ii) interaction of the arc with the free surface and possible surface deformation, (iii) convective heat transfer due to fluid flow in the weld pool, (iv) thermal conduction into the solid workpiece, (v) convective and radiative heat losses, (vi) transient solidification and melting, (vii) electromagnetic stirring due to the divergent current path, (viii) Thermocapillary or Marangoni convection due to surface tension gradient , and (ix) buoyancy in the weld pool. The various weld pool dynamics phenomena in GTA welding are not fully understood. The prime concern is to be able to predict the depth and width of the weld pool and develop a clear understanding of how the properties of the materials govern the choice of actual welding parameters, i.e. welding current, speed, gas purge flow etc. [1]. It has been found that conduction and convection in the weld pool determines how the weld pool shape develops. While conduction depends on the properties of the metal plate being joined, the convection in the melt pool is determined by the various driving forces (transport processes), namely, buoyancy force, electromagnetic force (Lorentz force), surface tension force (i.e. shear stress induced by surface tension gradient at the weld pool surface, known as Marangoni convection), plasma (arc) drag force, force due to arc pressure, etc. For the GTA weld pool, heat transfer and fluid flow are

driven by a complex interplay of all these driving forces. Hence, to obtain a good quality weld in GTA welding processes, it is absolutely necessary to choose an appropriate set of welding parameters.

### 1.3 Heat Flow in Welding

A schematic representation of the qualitative energy balance of the welding process [1] that accounts for the arc and melting efficiencies is schematically shown in Fig. 1.2. The majority of the total energy from the process is provided by the welding arc, while a small portion is generated at the electrode. The energy generated by the arc and the electrode is distributed in two ways: (i) a portion is lost to the environment, represented by $E_{losses}$, and (ii) remainder is transferred to the workpiece, represented by $E_{w/p}$. The net energy delivered to the workpiece is also distributed in two ways: (i) a portion is used for melting of the fusion zone, represented by $E_{FZ}$, and (ii) remainder is transmitted to the adjacent substrate outside of the fusion zone, represented by $E_{sub}$, contributes to the formation of the heat-affected zone (HAZ).

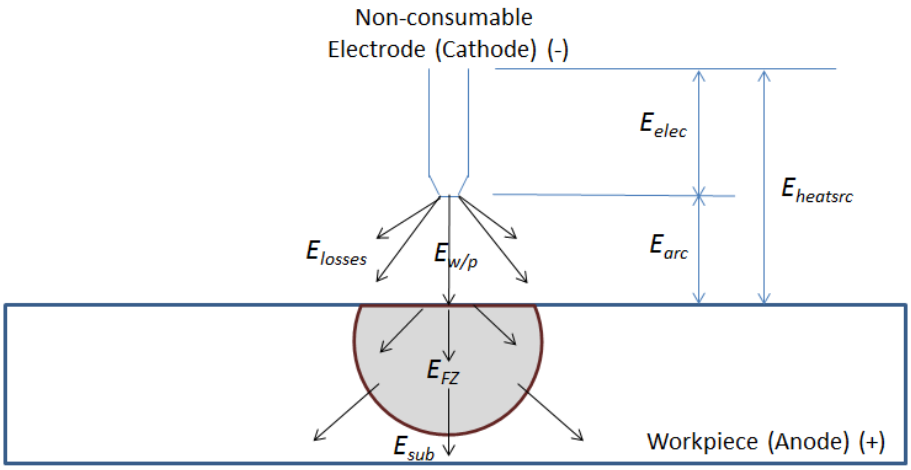


Figure 1.3: Energy distribution in the welding process.

The rate of energy generated by the arc is given by the product of the welding current and arc voltage. The heat input per unit length of the weld is given by the ratio of the product of the arc power and arc efficiency to the travel (welding) speed. The net arc power and heat input per unit length of the weld are used extensively in heat flow models. The heat flow associated with welding can strongly affect the phase transformations during welding and thereby influence the resultant microstructure evolution and properties of the weld. It is also responsible for weld distortions and residual stresses. Knowledge of arc efficiency is required for determination of the net energy delivered to the workpiece and accurate utilization of heat flow models. It is to be noted that the arc efficiency is only slightly affected by the welding parameters for a given process. The arc efficiency, $\eta_{arc}$ and the melting efficiency, $\eta_{melt}$ are both given as

$$\eta_{arc} = \frac{E_{w/p}}{E_{heatsrc}} = \frac{E_{FZ} + E_{sub}}{E_{heatsrc}} \tag{1.1}$$

$$\eta_{melt} = \frac{E_{FZ}}{E_{w/p}} = \frac{E_{FZ}}{E_{FZ} + E_{sub}} \tag{1.2}$$

where, $E_{w/p}$ is the energy from heat source that is transferred to the workpiece, $E_{FZ}$ is the energy required to melt the fusion zone, and $E_{sub}$ is the energy lost to the adjacent substrate outside the fusion zone.

For the analysis of heat flow in welding, simplifications have been made over the years in the representation of the heat source power density distribution. The most widely used approximation of the heat source power density distribution has been the Gaussian distribution [1]. It has been observed that decreasing the power density of the heat source decreases the weld penetration. Also, in GTA welding with DCEN, the shape of the electrode tip affects both the shape and power density distribution of the arc. As the electrode tip becomes blunter, the diameter of the arc decreases and the power density distribution increases, i.e., the arc becomes more constricted as the conical tip angle of the tungsten electrode increases.

It has been found that both conduction and convection takes place in the weld pool, while there is only conduction in the solid workpiece. Also, convection and radiation losses occur from the surface of the workpiece. The workpiece (substrate) displays the characteristics of a heat sink. The cooling rate of the workpiece increases with the thickness of the workpiece. This is due to the fact that a thicker workpiece acts as a better heat sink to cool the weld down.

### 1.4 Fluid Flow in Weld Pools

The driving forces for fluid flow in the weld pool include the buoyancy force, the Lorentz force, the shear stress acting on the pool surface due to the arc plasma, and the shear stress induced by the surface tension gradient, as represented schematically in Fig. 1.4. Even though the arc pressure acts on the pool surface, but its effect on the fluid flow is small, especially below 200A [1]. Each of the driving forces is discussed below.

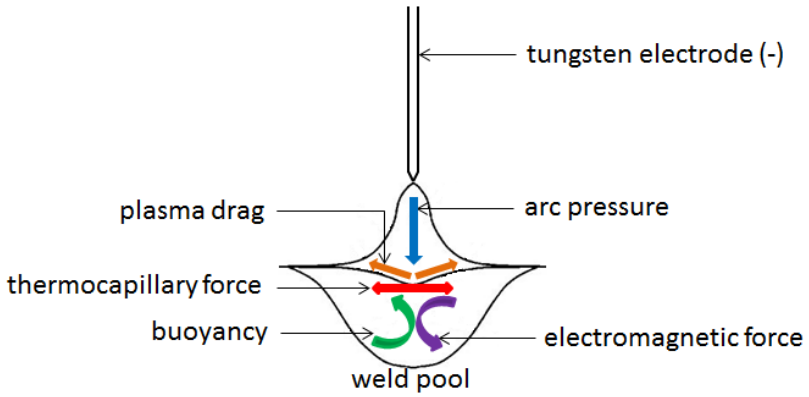


Figure 1.4: Driving forces for fluid flow in the weld pool.

#### 1.4.1 Buoyancy Force

With increase in temperature the density of the liquid metal decreases. Since the arc/heat source is located in the central region of the weld pool surface, the liquid metal is warmer at the center and relatively cooler at the periphery. Due to gravity, the heavier liquid metal falls along the weld pool boundary and rises along the pool axis, as shown in Fig. 1.5. The buoyancy force

tends to make the weld shallow and wide [1]. This driving force is included in the governing equations in the computer modeling of fluid flow in the weld pool.

Figure 1.5: Weld pool convection due to buoyancy driving force.

### 1.4.2 Lorentz Force

The DCEN configuration of GTA welding is used to discuss this force. The electric current in the workpiece converges toward the tungsten electrode, i.e. near the center of the weld pool surface. This converging current field, together with the magnetic field it induces, causes a downward and inward Lorentz force, as shown in Fig. 1.6(a). As a result, the liquid metal is pushed downward along the pool axis and rises along the pool boundary, as shown in Fig. 1.6(b). The Lorentz force tends to make the weld narrow and deep, under the DCEN configuration [1]. This driving force is included in the governing equations in the computer modeling of fluid flow in the weld pool.

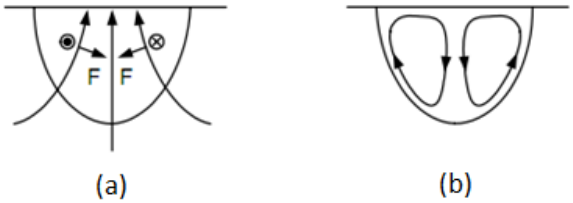


Figure 1.6: Weld pool convection due to Lorentz force.

### 1.4.3 Shear Stress Induced by Arc Plasma

The arc plasma moves outward along the weld pool surface and exerts an outward shear stress at the weld pool surface, as shown in Fig. 1.7(a). This shear stress causes the liquid metal to flow from the center of the weld pool surface to the pool edge and return below the pool surface, as shown in Fig. 1.7(b). The plasma induced shear stress tends to make the weld wide

and shallow [1]. This driving force is included in the boundary conditions in the computer modeling of fluid flow in the weld pool.


Figure 1.7: Weld pool convection due to plasma induced shear stress.

### 1.4.4 Shear Stress Induced by Surface Tension Gradient

The weld pool surface has high temperature gradients. In the presence of surface-active agent, the surface tension gradient in the weld pool can be positive or negative depending on the percentage weight of the active agent and surface temperature of the weld pool. To discuss the convective motion set up by the surface tension gradient, we consider that it is negative and that it decreases with increasing temperature. Under such conditions, the warmer liquid metal with a lower surface tension near the central region of the weld pool will be pulled outward by the cooler liquid metal with a higher surface tension near the periphery of the weld pool. This sets up an outward shear stress at the weld pool surface, as shown in Fig. 1.8(a). This causes the liquid metal to flow from the central region of the weld pool surface to the edge and return below the pool surface, setting up a convective motion, as shown in Fig. 1.8(b). This tends to make a wide and shallow weld [1]. On the contrary, if the surface tension gradient was positive, a radially inward convective motion would have been set up, resulting in a deep and narrow weld. This driving force is included in the boundary conditions in the computer modeling of fluid flow in the weld pool.


Figure 1.8: Weld pool convection due to negative surface tension gradient.

## 1.5 Residual Stresses and Distortion

Residual stresses are stresses that would exist in a body if all the external loads were removed. These stresses are locked into the component/structure. Residual stress is a process-induced stress and its type depends on the processing (mechanical/thermal) undergone by the part. Examples of mechanical processing would be bending, forging, rolling, etc. Welding is an example of thermal processing of a part. During welding, the workpiece is subjected to high energy input, and is stressed beyond the elastic limit and enter into plasticity and result in residual stresses. Welding induced residual stresses remain in the material as a result of liquid-to-solid transformation associated with the solidification and subsequent non-uniform cooling of the weld region altered by phase transformations in the solid state.

The thermal cycle imposed on welded structures during GTA welding causes thermal expansions and contractions that vary with time and location. Consequently, thermal stresses appearing in the hot regions near the weld are restrained by the cooler regions further away. Plastic deformation, occurring due to these thermal stresses, leads to thermally-induced residual stresses in the welded components that remain after the temperatures have returned to ambient levels [1]. The two factors that control the thermally-induced residual stresses are thermal treatment (heating or cooling) and restraint. Both the thermal treatment and restraint of the component must be present to generate residual stresses. Hence, the use of welding in fabrication or repair of the industrial structures introduces thermal residual stresses in the weld itself and in the base metal. Moreover, the residual stress field combines with stresses from in-service loads, strongly influencing the behavior of welded components under operational loads. Tensile residual stress reduces crack initiation life, accelerates growth of pre-existing or service-induced defects and increases the susceptibility to failure by fracture [1]. They can significantly reduce the life of a component and in most cases cannot bear a load matching the original specifications of the metal's strength. Compressive residual stresses are generally beneficial, but cause a decrease in the buckling load. Residual stresses are extremely hard to detect as they are present in the material component without application of any external loads. There are various ways to measure the magnitude of residual stresses in a component ranging anywhere from hole-drilling, which measures the stress relieved by drilling a hole using strain gauge rosettes, to the neutron diffraction method.

Hence, knowledge of thermally-induced residual stress characteristics is essential for the structural integrity assessment of welded structures. Once residual stress distributions are known, subsequent simulations of stress relief by mechanical loading or by post-weld heat treatments can be performed. One of the methods to reduce these stresses in the post weld stage is to shot peen the welded surface [1]. During the process of shot peening, tiny spherical balls are projected onto the surface of the material. The tensile residual stresses induced by the welding application are then diminished due to the compressive stresses that the shot peening process creates. One of the most common ways to decrease the influence of residual stresses in the welded structure is to heat treat it. After the components have been welded together, heating it for an extended period of time and the quenching it rapidly can recover some of the mechanical properties that have been lost due to welding.

Due to solidification shrinkage and thermal contraction of the weld metal during welding, the workpiece has a tendency to distort. Fig. 1.9(a)-(e) depicts several types of weld distortions.

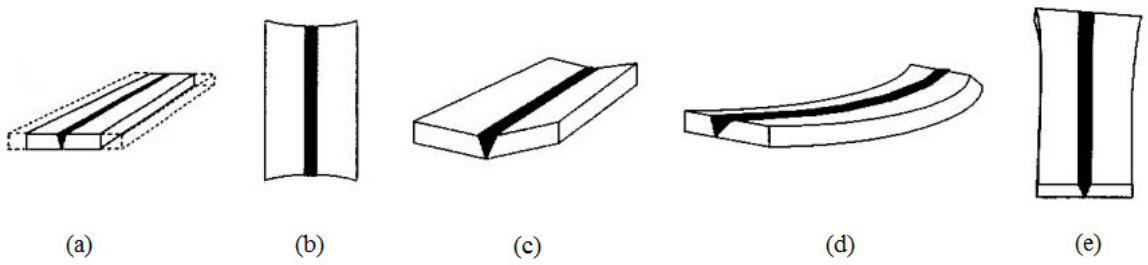


Figure 1.9: Deformation patterns.

The welded workpiece can shrink in the transverse direction, as shown in Fig. 1.9(a). It can also shrink in the longitudinal direction along the weld, as shown in Fig. 1.9(b). Upward angular distortion usually occurs when the weld is made from the top of the workpiece alone, as shown in Fig. 1.9(c). The weld in such a case tends to be wider at the top than at the bottom, causing more solidification shrinkage and thermal contraction at the top of the weld than at the bottom. Consequently, due to this non-uniform transverse shrinkage over the thickness, the resultant angular distortion is upward. It is noted that for butt welds, the angular distortion increases with

workpiece thickness because of increasing amount of the weld metal and hence increasing solidification shrinkage and thermal contraction. If the plate being welded is thin relative to the weld size, then it may bow as the shrinkage is above the neutral axis of the plate, as shown in Fig. 1.9(d). Another deformation mode is warping, and is shown in Fig. 1.9(e). The variations of the deformation behavior can be even more pronounced as there is a number of contributing competitive factors. The weld pool is a soft region and does not directly affect the overall deformation. Although the laid weld is shrinking there is a certain volume that has been heated due to the weld. This volume contributes through its thermal expansion/contraction to the deformation. These regimes affect the overall deformations together with boundary conditions representing the fixtures. The relation between the welding speed and the heat diffusivity is one major factor that can change the behavior.

Several techniques can be used to reduce weld distortion. Reducing the volume of the weld metal can reduce the amount of angular distortion and lateral shrinkage. Employing single-pass deep penetration welding reduces angular distortion. With increase in joint preparation angle the angular distortion increase. As a result butt joints undergo little angular distortion. Presetting the components being welded is another method to reduce distortion of the final welded component. Preheating, thermal management during welding, and post-weld heating can also reduce angular distortion.

## 1.6 Thermal Cycle and Microstructure Evolution

During welding, parts of the base metal lying adjacent to the fused zone are subjected to one or more thermal cycles. In this heat-affected-zone (HAZ) significant change in the microstructure and properties takes place due to transformations induced by the thermal cycles. The microstructure that develops in different parts of the HAZ depends upon the chemical composition (hardenability) of the material, the thermal cycle, and the austenite grain size [1]. These variables are to some extent interrelated, as the grain size depends upon both the chemical composition and the thermal cycle. The temperature changes in welding are very fast and the phase changes depend on the cooling and heating rates and other factors. One of the approaches to account for this is to describe the different microstructure regions near a weld by comparing the peak temperature with the equilibrium Fe-C diagram. Chapter 2 gives a detailed background

on effect of cooling rate (solidification mode) on microstructure evolution and post-solidification phase transformations.

### 1.7 The Multi-Physics of Welding

The welding process comprises several highly coupled (and non-linear) physical phenomena - fluid flow in the weld pool, heat flow in the welded structure, microstructural evolution/phase transformations, thermal stress development, and distortion of the welded structure. Modeling of welding processes encapsulating these complex phenomena is an inherent multi-physics problem. The mechanical response of welds is sensitive to the close coupling between thermal energy distribution, microstructure evolution and mechanical (deformation/stress) behavior. Figure 1.10 describes the coupling between the different fields in the modeling of welding. The solid arrows denote strong coupling and the dotted arrows denote weak coupling.

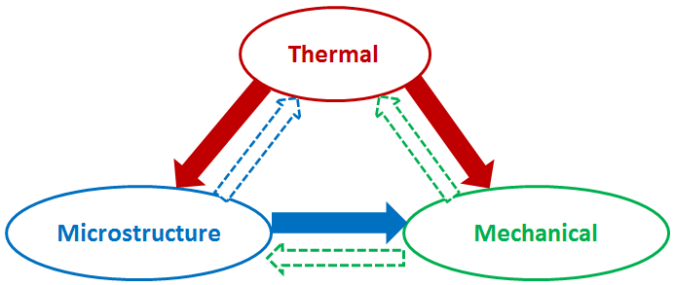


Figure 1.10: Coupling between different fields in welding analysis.

It can be noted that the effect of thermal energy on the microstructure and mechanical response is dominant. However, the effect of microstructure evolution on thermal energy is negligible, and hence the thermo-metallurgical problem is treated as one-way coupled. Due to a weak coupling from mechanics to thermals (i.e. heat generation due to deformation being negligible), the thermo-mechanical problem is treated as one-way coupled, i.e. the temperature field is predicted prior to the stress field calculation. The effect of microstructural evolution and phase transformations can strongly affect the mechanical behavior; however the reverse effect is negligible. Hence, the metallurgical-mechanical problem can also be treated as one-way coupled.

In general, when the objective of the analysis is to determine the thermal effects of welding on mechanical response (i.e. residual stress and distortions) of welded joints, the simplest approach is to consider only the one-way coupled thermo-mechanical problem. Such an analysis would help delineate the effects of thermal evolution of the welded joint on the developed stresses and deformations. However, the residual stress distribution and distortion measurements predicted under such an approach would not be absolutely accurate when compared to experimental data on stress distribution and deformation as the strong influence of microstructure change on mechanical behavior is not taken into account. Still, it is desired to carry out such thermo-mechanical simulations as they help obtain better insight on the importance of various welding parameters and their effect on the developed thermal stresses.

For thermo-mechanical or thermo-metallurgical-mechanical analysis of a welding process, the effect of fluid flow in the weld pool during welding needs to be incorporated for an even more accurate estimation of mechanical behavior. The fluid flow occurring in the weld pool strongly influences the thermal energy distribution in the welded joint. Proper estimation of temperature distribution in the welded structure is necessary for accurate prediction of thermally-induced stresses in the workpiece. The field of weld pool dynamics has a strong two-way coupling with the thermal field, as shown in Fig. 1.10. The strongly coupled weld pool dynamics field thus can be integrated with other coupled fields in the welding process, through the thermal field, for better prediction of mechanical response of welded joints.

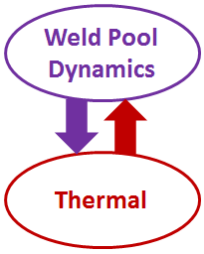


Figure 1.11: Strong two-way coupling between weld pool dynamics and thermal fields.

It is to be noted that the field of microstructure can be accounted for through techniques of material modeling, and made part of the overall solution. In material modeling, the material

properties are defined as a function of both temperature and microstructure change. Such an analysis would indirectly incorporate microstructural aspects in the material description through the exploitation of microstructure dependency on temperature and deformation.

# Chapter 2

# Microstructure Evolution

During welding the workpiece material undergoes significant change in the microstructure and properties due to transformations induced by the thermal cycles. In order to better understand microstructure change and their effects on the mechanical response of welded structures, some basic understanding of solidification is necessary. Solidification mode varies across the weld metal and is affected by welding parameters. Moreover, the post-solidification phase transformations also change the solidification microstructure and properties of the weld metal.

## 2.1 Basic Solidification Concepts

When a liquid of uniform composition solidifies, the resultant solid is seldom uniform in composition [1]. The solute atoms in the liquid are redistributed during solidification. The redistribution of the solute depends on both thermodynamics, i.e., the phase diagram, and kinetics, i.e., diffusion, undercooling, fluid flow, etc. Solute redistribution during solidification results in microsegregation across cells or dendritic arms. In addition to microsegregation, solute segregation can also occur as a result of growth rate fluctuations caused by thermal fluctuations, this phenomena being known as banding. During the solidification of a pure metal the solid/liquid (S/L) interface is usually planar, unless severe thermal undercooling is imposed. During the solidification of an alloy, however, the S/L interface and hence the mode of solidification can be planar, cellular, or dendritic depending on the solidification condition and the material system involved. It has also been observed that higher the cooling rate, i.e., the shorter the solidification time, the finer the cellular or dendritic structure becomes. The growth of a dendrite during solidification is shown schematically in Fig. 2.1. The window for viewing is kept stationary as the dendrite tip advances during various stages of solidification. The large dendrite arms grow at the expense of smaller ones as solidification proceeds. Thus, slower the cooling rate during solidification, the longer the time available for coarsening and the larger the

dendrite arm spacing [1]. The effect of the temperature gradient $G$ and the growth rate $R$ on the solidification microstructure of alloys is represented in Fig. 2.2. Together, $G$ and $R$ dominate the solidification microstructure. The ratio $G/R$ determines the mode of solidification while the product $G*R$ governs the size of the solidification structure [1].

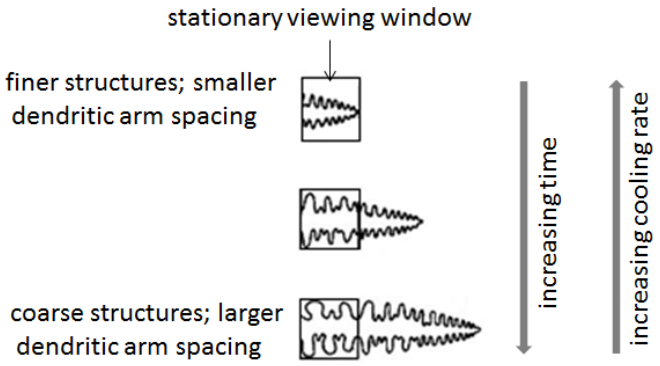


Figure 2.1: Schematic representation of dendritic growth of an alloy at a fixed position at the various stages of solidification.

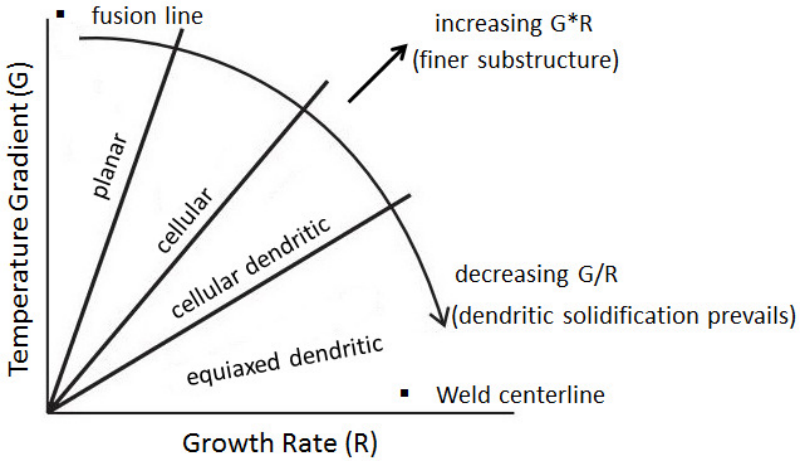


Figure 2.2: Effect of temperature gradient $G$ and growth rate $R$ on the morphology and size of solidification microstructure.

## 2.2 Solidification Modes

The solidification mode changes from planar to cellular and from cellular to dendritic as the constitutional supercooling at the pool boundary increases [1].While the solidification mode can vary from one weld to another, it can also vary within a single weld from the fusion line to the centerline. During rapid solidification of the weld pool, the critical parameters in determining the fusion zone microstructure are temperature gradient $G$, solidification growth rate $R$, undercooling $\Delta T$, and alloy composition. Figure 2.3 shows the average temperature gradient at the weld centerline $G_{\mathrm{CL}}$ and the fusion line $G_{\mathrm{FL}}$ of the weld pool along a given plane, defined as

$$G_{\mathrm{CL}} = \frac{T_{\mathrm{P}} - T_{\mathrm{L}}}{a} \tag{2.1}$$

$$G_{\mathrm{FL}} = \frac{T_{C} - T_{\mathrm{L}}}{b} \tag{2.2}$$

where, $T_{\mathrm{P}}$ is the peak temperature, $T_{\mathrm{L}}$ is the liquidus temperature, $T_{\mathrm{C}}$ is the temperature of the location of the heat source. $a$ is the distance between the location of the peak temperature and boundary at the weld pool centerline, and $b$ is the distance between the axis of heat source and fusion line boundary. It is to be noted that the location of the maximum width of the pool may lie in front/behind the heat source depending on the welding speed and other parameters. Both $G_{\mathrm{CL}}$ and $G_{\mathrm{FL}}$ decrease as the welding speed increases. Under steady state condition during welding, the shape of the weld pool remains constant, and hence the solidification rate varies with position along the fusion boundary. As seen from Fig. 2.3, the direction of movement of the solidification front is along the maximum thermal gradient normal to the S/L interface. Hence, the steady state solidification rate $R$ is related to the welding speed as

$$R = V \cos\alpha \tag{2.3}$$

where, $\alpha$ is the angle between the normal to the S/L interface and the welding direction, and $V$ is the welding speed. The solidification rate is lowest at the edge of the weld pool, i.e. $\alpha \to 90^0$, as indicated by point B in Fig. 2.3. The solidification rate is highest at point A on the weld centerline, i.e. $R_{CL} = V$, because the interface normal has the same direction as the welding direction. The solidification rate decreases from point A to B along the fusion boundary. Hence, the solidification rate at the fusion line is zero, i.e. $R_{FL} = 0$, and $R_{CL} >> R_{FL}$.

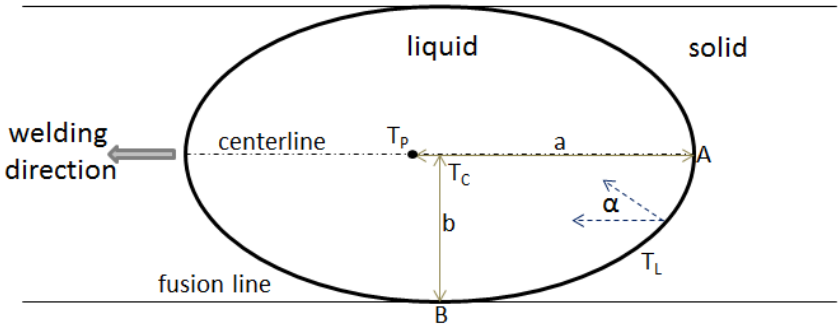


Figure 2.3: Schematic plot for calculation of temperature gradients at the weld centerline and fusion line.

Since the weld pool is elongated, the distance between the maximum pool temperature $T_P$ and the pool boundary $T_L$ is greater at the centerline than at the fusion line. Consequently, the temperature gradient normal to the pool boundary at the centerline, $G_{CL}$ is less than that at the fusion line, $G_{FL}$. Since, $G_{CL} < G_{FL}$ and $R_{CL} >> R_{FL}$, we have

$$\left(\frac{G}{R}\right)_{CL} << \left(\frac{G}{R}\right)_{FL} \tag{2.4}$$

$$(G*R)_{CL} > (G*R)_{FL} \tag{2.5}$$

As per Eq. (2.4), the value of $G/R$ decreases from the fusion line toward the centerline. This suggests that the solidification mode may change from planar to cellular, columnar dendritic, and equiaxed dendritic across the fusion zone. Figure 2.4 depicts the variation in solidification mode across the fusion zone. According to Eq. (2.5), the cooling rate $G*R$ at the weld centerline is higher than that at the fusion line. This suggests that the dendritic arm spacing decreases from the fusion line to the centerline because the dendritic arm spacing decreases with increasing cooling rate [1].

The heat input and welding speed can affect the solidification mode of the weld metal significantly. With increase in welding speed, the value of $G*R$ is increased while the value of $G/R$ is reduced at the weld pool centerline. It is known that the solidification mode changes from planar to cellular and dendritic as the ratio $G/R$ decreases. Under the same welding speed, as the heat input increases, the temperature gradient $G$ decreases and hence $G/R$ decreases. Hence, at higher heat inputs $G/R$ is lower and the dendritic solidification prevails, while at lower heat inputs $G/R$ is higher and cellular solidification prevails [1].

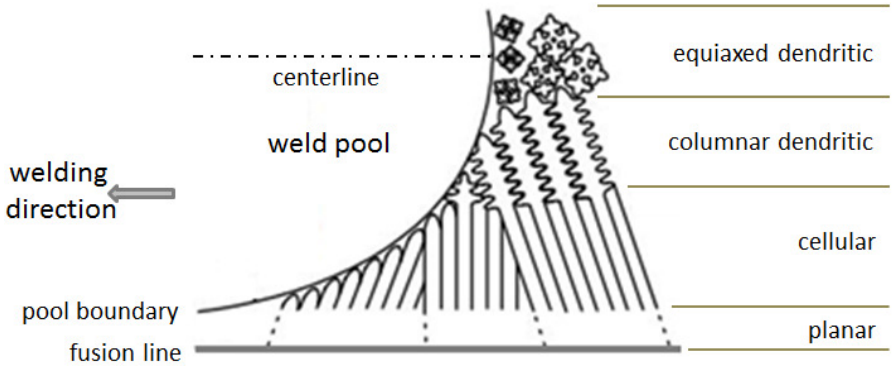


Figure 2.4: Variation in solidification mode across the fusion zone.

### 2.3 Post-Solidification Phase Transformation

When post-solidification phase transformations occur they change the solidification microstructure and properties of the weld metal. The 300 series grade of austenitic steel is the most widely used in the industries. The welds of austenitic stainless steels normally have an

austenite (fcc) matrix with varying amounts of $\delta-$ferrite (bcc). The development of the weld metal microstructure in austenitic stainless steels is described in Fig. 2.5. Figure 2.5 is obtained from the ternary phase diagram of the Fe-Cr-Ni system by taking a vertical (isoplethal) section at approximately 70% Fe and above 1475K. Alloys with a composition on the Cr-rich side have $\delta-$ferrite as the primary solidification phase, i.e., the first solid phase to form from the liquid. In contrary, alloys with a composition on the Ni-rich side have austenite as the primary solidification phase [1].

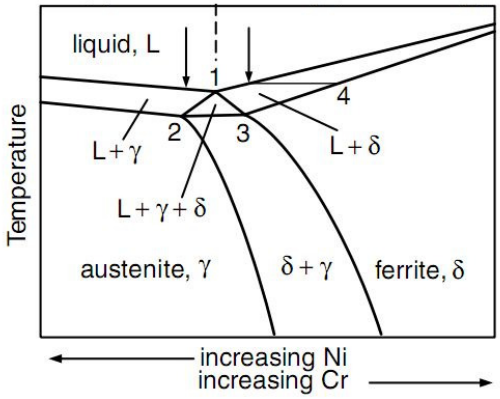


Figure 2.5: Schematic of the vertical section of the ternary-phase diagram at approx. 70% Fe.

# Chapter 3

---

## Background and Literature Review

It has been more than 60 years since Rosenthal [2, 3] presented his solution for the heat flow due to a point source of heat traversing the surface of a semi-infinite block of material. The techniques involved ignored any convective motions in the molten metal. Woods and Milner [4] studied fluid flow in weld pools by examining the mixing of dissimilar metal droplets in the pools. Their experiments showed that the weld pool produced by a TIG arc was vigorously stirred and was primarily due to electromagnetic forces. They found that buoyancy-driven convection was comparatively very small. Early 1980s saw growing interest in understanding the fluid motion in weld pools and its role in affecting both the heat transfer phenomena and thereby the mechanical properties of the welds. Heiple and Roper [5, 6] conducted a series of experiments to study the fluid flow and weld penetration during the GTA welding of stainless steels. Their studies showed that when a surface active agent was present in the liquid metal, at a small but significant amount, the temperature coefficient of surface tension $\partial\gamma/\partial T$ changed from a negative to a positive value, thus reversing the surface-tension gradient driven flow direction and making the weld pool much deeper. In addition to the qualitative [4-6] studies, quantitative studies were also carried out. Atthey [7] considered a steady-state fluid flow in an assumed hemispherical weld pool by a distributed current source. Until that time, this was the closest mathematical model to the weld pool problem. Oreper et al. [8] studied fluid flow in stationary GTA weld pools. They did not calculate the pool shape, and considered it known in their fluid flow model. One of the first papers addressing the transient development of fluid flow and temperature fields in the molten pool in GTA welding was by Oreper and Szekely [9]. They identified key phenomena affecting the weld pool dynamics as arc pressure, arc heat flux, buoyancy, electromagnetic force, force due to surface-tension, plasma jet impingement, surface deformation, conductive and convective heat transfer processes in the pool. Their mathematical model was based on the assumptions of non-deformable top surface and negligible plasma drag force. They calculated that in the absence of surface tension effects both buoyancy and electromagnetic forces play a significant role in determining the flow field. However, under such

a situation the flow field has a negligible effect on the heat transfer process. But when the surface-tension driven flow was incorporated, it was found to have a profound effect on the weld pool shape. This was due to the high surface velocities produced by the surface-tension gradients. Kou and Sun [10] carried out a computer simulation of the weld pool fluid flow and its effect on the weld penetration. They used a two-dimensional, steady-state model with stationary arc. Three driving forces for fluid flow were included in their model, namely the buoyancy force, the electromagnetic force and the surface tension gradient. They found that surface tension gradient at the surface had the maximum, and buoyancy the minimum influence on fluid flow in the weld pool. Their results confirmed the strong influence of fluid flow on the weld penetration. Simulation results by Kou and Wang [11] showed that compared to the buoyancy force, the surface tension gradient and Lorentz force dominated the convection mode in the weld pool. Since the 1980s, Debroy and co-workers [80-84] have studied in detail the fluid flow in weld pool under GTA welding by comparing the computational model with experimental results for both stationary and moving GTA welding. Till the mid-1980s, experiments and computer simulations that were carried out primarily focused on understanding the weld pool phenomena at a very crude level. However, since the early 1990s, detailed research works have been carried on to understand all the physics that influences the weld pool shape, depth-to-width ratio, and residual stresses etc.

### 3.1 Surface Tension Gradient Induced Flow

Surface tension driven flow, known as thermocapillary flow or marangoni convection, has been shown to be the principle driving force for fluid flow, heat transfer and resulting weld shape and size. Heiple and co-workers [5, 6, and 12] showed that when a surface active agent is present in the liquid metal, at a small but significant amount, the temperature coefficient of surface tension $\partial\gamma/\partial T$ can be changed from a negative to a positive value, thus reversing Marangoni convection and making the weld pool much deeper. This reversal in the direction of circulation in the weld pool has significant implications in several practical systems. Examples of surface active elements in stainless steel are sulphur (S), oxygen (O), selenium (Se) and tellurium (Te). This reversal of Marangoni convection pattern has been attributed to be the main mechanism behind changing the weld pool depth and was first proposed by Bennett and Mills[13], Heiple

and Roper[5,14], and Heiple and Burgardt [15] in the 1980s. In 1988, Sahoo et al. [16] gave the relation for surface tension of metal-solute (*i*) alloys as a function of surface temperature, T, and surface active agent content, $a_i$

$$\gamma = \gamma_m^0 - A_g(T - T_m) - RT\Gamma_s \ln\left\{1 + k_l a_i \exp\left(-\frac{\Delta H^0}{RT}\right)\right\} \tag{3.1}$$

where, $\gamma_m^0$ is the surface tension of pure metal at the melting point, $A_g$ is the negative of $\partial\gamma/\partial T$ for pure metals, $T_m$ is the melting point of the material, R is the gas constant, $\Gamma_s$ is the surface excess solute concentration at saturation, $k_l$ is the constant related to entropy of segregation, $a_i$ is the activity of species '*i*' in %wt., $\Delta H^0$ is the standard heat of adsorption. The temperature coefficient of surface tension is then given by differentiating Eq. (3.1) with respect to T, as

$$\partial\gamma/\partial T = -A_g - R\Gamma_s \ln(1 + Ka_i) - \frac{Ka_i}{1+Ka_i}\frac{\Gamma_s \Delta H^0}{T} \tag{3.2}$$

where, K is the adsorption coefficient and is defined as

$$K = k_l \exp(-\Delta H^0/RT) \tag{3.3}$$

This surface tension model for binary metal-surface active solute systems was modeled based on the Gibbs and Langmuir adsorption isotherms and consideration of the surface segregation of the

solutes. It is to be noted that $\partial\gamma/\partial T$ is negative for pure metals and is a function of both temperature and composition. Sahoo et al. discussed in their paper that below a certain %wt. of surface active agent content, $\partial\gamma/\partial T$ will remain negative across the weld pool surface, irrespective of the surface temperature profile, thus resulting in a radially outward flow on the pool surface. However, above certain higher %wt. of surface active agent content $\partial\gamma/\partial T$ can change from a positive value at relatively low temperatures to a negative value at higher temperatures. Hence, for higher %wt., $\partial\gamma/\partial T$ might go through an inflection point at certain locations on the weld pool surface. However, no results were highlighted in the paper. It is to be noted that this model proposed by Sahoo et al. was developed under assumptions of equilibrium thermodynamics. Figure 3.1 shows the variation of surface tension gradient of FeS system as a function of composition and surface temperature, and as represented by Eq. (3.2).

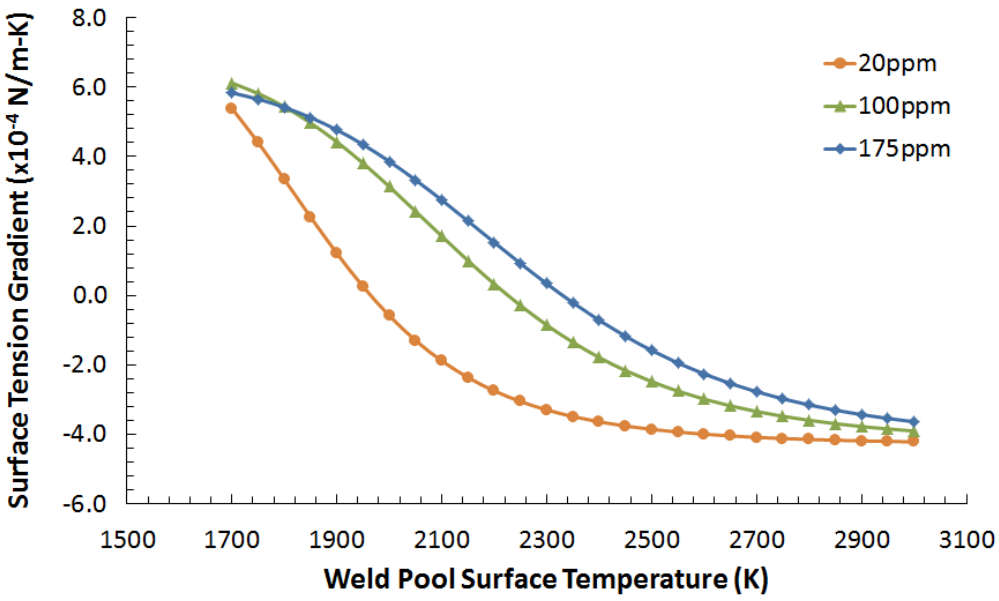


Figure 3.1: Variation of temperature coefficient of surface tension of FeS system as a function of composition and surface temperature.

It was shown by Zacharia et al. [17, 18] that a simple arbitrary assumption of a single valued positive leads to an unrealistic weld pool aspect ratio, whereas the use of Eq. (3.2) results in

reliable predictions. McNallan and Debroy [19] also built on this model and extended it to predict the temperature and composition dependence of surface tension in alloys containing nickel, chromium and small amounts of other elements, when sulphur is the primary surface-active impurity in the alloy. They identified temperature coefficient of surface tension $\partial\gamma/\partial T$ of the alloy to be the most important parameter in welding applications. The effects of sulphur content on thermocapillary convection in weld pools under GTA welding of type 304 SS were studied by Lei et al. [20]. Computations were conducted for sulphur contents in the range from 0.003 to 0.03%wt. and 100A welding current. The nature and strength of vortices developed were discussed. Due to the low welding current used, they made a reasonable assumption of a flat weld pool surface in their model [48, 52]. They however used constant thermophysical properties. Pierce et al. [21] investigated the influence of the arc phenomena on the weld shape and thermocapillary flow. They found the thermocapillary flow to be limited by two arc factors, namely, the arc length and the arc current. They studied the thermocapillary flow reversal for current less than 200A and they also neglected the arc plasma shear force in their studies. They reported that the input energy density increased with higher arc power, slower travel speed and shorter arc length. Experimental study for visualization of Marangoni convection with surface active agent was performed by Limmaneevichitr and Kou [22]. They identified that interference of electromagnetic force in the weld pool and plasma drag force due to arc inhibits the study of thermocapillary convection in arc welding. Also, flow visualization in a weld pool is only limited to the pool surface due to opacity. To circumnavigate these problems, they used a defocused laser beam instead of an arc. The Marangoni convection thus induced should be similar to that induced by the arc. Also, to visualize the flow reversal pattern inside the weld pool, they used a transparent pool of sodium nitrate with potassium acetate as the surface-active agent (Fig. 3.2). The Marangoni number for the simulated weld pool of sodium nitrate was found to be close to that of steel weld pools. They studied the flow reversal and its effects on the weld shape. The Marangoni number was given as

$$Ma = \frac{-\frac{\partial\gamma}{\partial T}(\Delta T)_L}{\mu\alpha} \tag{3.4}$$

where, $(\Delta T)_L$ is the temperature differences between the center and edge of the pool, $\mu$ is the dynamic viscosity and $\alpha$ is the thermal diffusivity. Limmaneevichitr and Kou [23] continued their experiments and found that in the absence of surface-active agents and electromagnetic force, the pool bottom convexity increases with increasing Peclet number. Such change in pool bottom shape from concave to flat to convex with increasing Peclet number reflected the increased dominance of heat transport by convection. They related the weld pool shape to the Peclet and Prandtl numbers. The Peclet number (Pe) and Prandtl number (Pr) were defined as follows

$$\text{Pe} = \frac{\text{heat transport by convection}}{\text{heat transport by conduction}} = \frac{\text{LV}}{\alpha} \tag{3.5}$$

$$\text{Pr} = \frac{\text{momentum diffusivity}}{\text{thermal diffusivity}} = \frac{\upsilon}{\alpha} \tag{3.6}$$

where, L is the pool surface radius, V is the maximum surface velocity and $\upsilon$ is the kinematic viscosity. The purpose of using the Peclet number was to depict the effect of Marangoni convection on the weld pool shape in the absence of surface-active agent. These experiments showed how the weld shape could reveal details about the weld pool convection.

Chakraborty and Chakraborty [24] developed a three-dimensional mathematical model to study the effects of the sign of surface tension coefficient, i.e. Marangoni flow reversal, in both laminar and turbulent weld pool convection under GTA welding. They report that due to enhanced mixing in a turbulent pool, the mean convective effect becomes weaker and tends to reduce the pool penetration in case of positive surface tension coefficient. However, an effective enhancement in diffusion tends to increase the pool depth. These two counteracting mechanisms compete in deciding the final pool depth. Significant amount of research work has been done to

improve the penetration of TIG welding utilizing the flow reversal characteristics of the Marangoni convection. Research works have showed that by smearing oxide fluxes [25, 26] or adding small amounts of active-gas, $O_2$ or $CO_2$ [27-29], to the argon shielding gas can dramatically increase the TIG depth again by utilizing the Marangoni flow reversal characteristics. Recently, Wei et al. [30] numerically predicted the effects of Prandtl number on two-dimensional Marangoni convection and weld pool shape induced by a negative surface tension coefficient. Their model did not account for electromagnetic forces as the heat source was chosen as a laser or electron beam. Similar study was done by Sen and Davis [31] flat pool surface assumption. They report that the Prandtl number, Marangoni number and weld pool shape are intricately related. For Pr>1, (i) the pool shape is hemispherical for Ma<100, (ii) pool bottom is convex for $10^2$<Ma<$10^5$ and (iii) pool bottom is slightly convex for Ma>$10^5$. The pool width increases with Ma and is almost independent of Prandtl number, when Pr>1. Pool depth decreases and then increases when Ma is increased beyond $10^3$. However, when Pr is very small, the pool depth decreases with increasing Ma and is almost insensitive to Pr variations. Irrespective of Pr, small increase in Ma exhibits rapid increase in width-to-depth ratio. Moreover, it was found that the surface temperature of the hottest part of the pool decreased with increasing Pr and Ma. Independent of the Pr, the peak surface temperature increased with decreasing Peclet number and decreasing travel speed of the incident heat flux.

Recent years have seen increased attention being paid to activating flux TIG (A-TIG) welding. Reason being the disadvantages of the TIG process, namely, relatively shallow penetration capability and low productivity. A-TIG is a variant of TIG, using a thin layer of an active flux being applied on the surface of the base metal. A-TIG process significantly increases penetration and aids in thick plate welding. A-TIG process can weld plates of thickness 6-10mm in a single pass [32]. Modenesi et al. [33] studied A-TIG process and reported around 300% increase in weld penetration compared to the conventional TIG process. Lu et al. [34] used five different oxide fluxes to systematically study the effects of single flux on penetration. They reported that when the oxygen content in the weld pool was within the range of 70-300ppm, it played a critical role in increasing weld penetration through Marangoni flow reversal. They report that increasing the thickness of the flux layer at first increases the weld depth, but further increase leads to a decrease in weld depth. Hence, too-low or too-high oxygen content in the

weld pool has negligible or no effect on the penetration. In spite of significant research work undertaken to understand this A-TIG process, there is still doubt on the actual mechanism of A-TIG welding. Four different mechanisms have already been proposed. The first mechanism [35] is based on the concept of lowering of the surface tension of weld pool by the flux results in an increased depression of the surface, thus providing an increased radius of curvature of pool surface to support the arc pressure, resulting in arc concentration at the descended portion of the pool. The second mechanism [5, 12 and 14] is based on the concept of Marangoni flow reversal due to dissolved flux. The third mechanism [36, 37] is based on the effects of vapor from the flux. It is suggested that vaporized flux molecules contract the welding arc. Hence, for a given current, there would be increased current density at the center of the arc, which would produce an increase in weld depth. The fourth mechanism is called the insulation mode and was suggested by Lowke et al. [38]. They identified that the metallic oxide fluxes that are generally used are good electrical insulators. Hence, the effect of the flux is to add a layer of high electrical resistance on the outer regions of the molten weld pool. Hence, towards the center of the weld pool there will be higher current density, and thereby increased penetration. Their suggested mechanism is based on the fact that the surface of weld pool is not depressed by the arc. This is a reasonable assumption for welding currents less than 200A [48, 52, and 54]. Significant work on A-TIG has also been done by Zhang and Fan [39] and Xu et al. [40]. They studied the effects of arc constriction and found that it can cause the width of the weld to be narrower, but had little effect on penetration. They studied the characteristic appearances of the arc in helium shielded GTA welding, with and without flux, at an 180A welding current. They found that in case of GTA welding without flux, a large and wide region of the blue luminous plasma exists in the lower part of the arc. However, in case of GTA welding with flux, the region of the blue luminous plasma is constricted at the center in the lower part of the arc.

Lu et al. [27-29, 41, and 42] performed extensive experimental studies of the effects of adding $O_2$ and $CO_2$ to argon and helium shielding gases on the Marangoni convection in the weld pool and weld penetration. They found that the decomposition of $O_2$ and $CO_2$ in the shielding gas provided a significant source of oxygen absorption for the molten metal pool in GTAW. Small addition of $CO_2$ could significantly increase the weld depth. They reported that under the specifications of the experiment, the Marangoni flow reversal took place when the oxygen content in the weld pool exceeded a critical value from 68 to 82ppm. Recently, Lu et al. [42]

performed numerical study of the use of $N_2$ versus Ar as a shielding gas. They found that due to higher specific heat and thermal conductivity $N_2$ arc is more constrict under the same arc length and welding current, and hence could enlarge the pool volume and increase the weld productivity.

### 3.2 Buoyancy- and Electromagnetic- Force Driven Flow

Secondary to the surface tension gradient force, the other two driving forces are buoyancy force and electromagnetic force. With increase in temperature the density of the molten metal decreases. The weld pool surface right below the center of the heat source is warmer than the region near the pool boundary. Gravity causes the heavier liquid near the edge of the pool to sink. Thus, buoyancy causes radially outward flow in the weld pool surface and downward flow near the pool edges, thereby setting up two counter-rotating convective loops [43]. Tendency of buoyancy is to increase the width of the weld pool, but decrease its depth. Effect of both buoyancy and surface tension is to flatten out the weld pool surface. In general, in all the published literature, authors have used the Boussinesq approximation to model buoyancy due to density variations of molten metal with temperature. The buoyancy force appears as a body-force term in the Navier-Stokes (N-S) equation and is given by [10, 51]

$$\vec{F}_b = \rho g \beta \, \Delta T \tag{3.7}$$

When dealing with the effects of buoyancy-driven flow, the Grashof number and the Bond number can be calculated as

$$Gr = \frac{\text{buoyancy forces}}{\text{viscous forces}} = \frac{\beta g (T_s - T_0) L^3}{\upsilon^2} \tag{3.8}$$

$$Bo = \frac{\text{gravitational force}}{\text{surface tension force}} = \frac{\rho g L^2}{\sigma} \tag{3.9}$$

where, $\beta$ is the compressibility factor, $T_s$ is the surface temperature, $T_0$ is the reference temperature, L is the length scale, $\upsilon$ is the kinematic viscosity of fluid, $\rho$ is the density of the material and $\sigma$ is the surface tension. It has been reported by Woods and Milner [4] and many others [10, 11, 45] that weld pool fluid flow due to buoyancy force is small compared to that due to electromagnetic force, and almost negligible when compared with surface tension driven flows. However, the buoyancy effects become significant when the depth of the weld pool is greater than 10mm.

Considering GTA welding with direct-current electrode negative (DCEN), the electric current in the workpiece converges towards the tungsten electrode and hence near the center of the pool surface. This converging current field interacts with the magnetic field it induces to produce the electromagnetic force or Lorentz force, which appears as a body force term in the N-S equations. The Lorentz force pushes the liquid metal downward along the pool axis and rises along the pool boundary [44, 45]. It tends to make the weld pool much deeper. The Lorentz force is represented as

$$\vec{F}_L = \vec{j} \times \vec{B} \tag{3.10}$$

where, $\vec{j}$ is the current density vector and $\vec{B}$ is the magnetic flux vector. Calculation for electromagnetic force for GTA welding was given by Kou and Sun [10]. When dealing with the effects of the electromagnetic force, the magnetic Reynolds number can be calculated as

$$R_m = \frac{\text{electromagnetic force}}{\text{viscous force}} = \frac{\rho \mu_m I^2}{4\pi^2 \mu^2} \tag{3.11}$$

where, $\mu_m$ is the magnetic permeability, $I$ is the current and $\mu$ is the dynamic viscosity of the material. Zhang et al. [50] reported that when the welding current is around 120A, the electromagnetic force becomes relatively small and has negligible effect [45]. Debroy et al. [83] studied the transient temperature and velocity field evolution under GTA spot welding, especially the shape and size of the heat affected zone (HAZ) for the thermal cycles. They performed dimensional analysis to delineate the effects of various driving forces on the convection in the weld pool and understand the heat transfer mechanism. For their investigation, they assumed a flat top weld surface [44, 48, 52, and 54] and a constant surface temperature gradient. They observed that the Peclet number increased progressively during heating, but decreased abruptly during cooling/solidification. They also determined the temperature gradient $G$ and solidification rate $R$ of the mushy zone to estimate the solidification morphology.

### 3.3 Arc Pressure

In GTA welding, the depression of the molten pool surface has long been an area of intense research. Friedman [46] and Choo et al. [47] have reported that the depressed weld pool surface influences the arc plasma/pool interaction, the weld pool convection and the weld penetration. Szekely and Thompson [85] studied the transient nature of weld pools when the pool surface is deformed. Lin and Eagar [48] found out that when the welding current is less than 240A, the pool surface depression is less than 1mm in case of full-penetration TIG weld pool. Wu and Dorn [49] used a three-dimensional model to find out the relation between weld pool depressions and weld penetration for TIG welding under full-penetration condition, and confirmed the results given by Lin and Eagar [48]. They highlight that when the workpiece is fully penetrated, the pool depression is less than 1mm under current levels less than 200A. Fan et al. [53] showed that in a fully-penetrated weld, the top surface depression is large and is caused by the sagged free bottom surface. Wu et al. [55, 56] established a correlation through three-dimensional numerical simulation between the transient behavior of weld pool surface deformation and workpiece penetration. Such quantitative analysis of fully-penetrated weld pool would help in the development of topside vision based penetration control in GTA welding. However, it has been

shown [48, 52, and 54] that when considering partial penetration of the workpiece, surface depression can be regarded as negligible if the welding current is less than 200A. Ko et al. [54] verified that the depression of the molten pool free surface is mainly due to arc pressure and to some extent by the inward circulation due to current, validating the work done by Lin and Eagar [70]. However, Marangoni flow decreases this surface depression and smoothens out its fluctuations. Hence, it has been shown that when operating below 200A, which is usually the case for GTA welding, arc pressure has negligible effect on fluid flow in weld pool [44, 68-70] and therefore, deformable weld pool surface need not be considered. It can be concluded that the dynamic balance between arc pressure, buoyancy force and surface tension force determines the ultimate shape of the weld pool surface [49, 52].

### 3.4 Plasma (Arc) Induced Shear Stress

The welding arc can be described as an ionic gas, or plasma, with an electric current passing through it [44]. The driving force behind the fluid flow in the arc is the electromagnetic force. Hsu et al. [57] described the arc in a single mathematical model for the first time. They solved the electric potential equation with the continuity, momentum and energy conservation equation. They also presented thermal profiles obtained from spectrometric measurements. McKelliget and Szekely [58] proposed a better representation of the heat and current flux density at the anode surface. Both these models [57, 58] assumed a known current density at the cathode surface. Similar models were highlighted by Choo et al. [59], Lee and Na [60], Goodarzi et al. [61], Fan and Shi [62], and Kim et al. [63] that helped to improve and better understand arc modeling. Ramirez et al. [64] compared the predictions of both formulations of electromagnetic field, i.e. electric potential equation and magnetic diffusion equation against each other and also against the available experimental and numerical solutions. They report the potential formulation to provide better solutions in the representation of welding arcs. Lee et al. [65] used the Gaussian current density distribution along the electrode surface and calculated the arc plasma temperature contours and validated the results with experimental data. Previous research works had assumed a uniform temperature distribution along the electrode. Fan et al. [66] calculated the combined arc plasma-cathode system, without any assumption of the current density distribution on the cathode surface. They report that the maximum current density increases with decreasing arc

length and that the current density distribution radius increase with increasing arc length. Cantin and Francis [67] conducted experiments to study the effects of arc polarity, arc length, welding current and shielding gas on the arc power and arc efficiency. They found that the arc polarity had the most profound effect on the arc power and arc efficiency. Shielding gas had the next most significant influence. Recently, Lu et al. [42] performed numerical study of the use of $N_2$ versus Ar as a shielding gas. $N_2$ demonstrated to have more constriction properties, thereby aiding in enlarging pool volume. Arc pressure in GTA welding is caused by the momentum transfer of the impinging plasma jet on the weld pool. It has been shown [44, 68-70] that in the case of GTA welding where the operating current is usually below 200A, the effect of arc pressure force on the fluid flow in the weld pool is negligible and thus can be neglected. Dong et al. [71] showed that for GTA welding of SUS304 stainless steel, the plasma drag force can be neglected for welding currents less than 160A. Their simulations showed that when the welding current becomes more than 200A, the plasma drag force becomes large and is one of the main factors that influence the weld shape. Hence, it can be concluded that in order to simulate the weld pool dynamics under GTA welding, operating well below 200A, the assumptions of flat weld pool surface, negligible plasma drag and arc pressure force are realistic. Figure 3.2 shows the plasma induced shear stress distribution on the molten pool surface for GTA welding of SUS304 stainless steel, under 200A current and 3mm arc length.

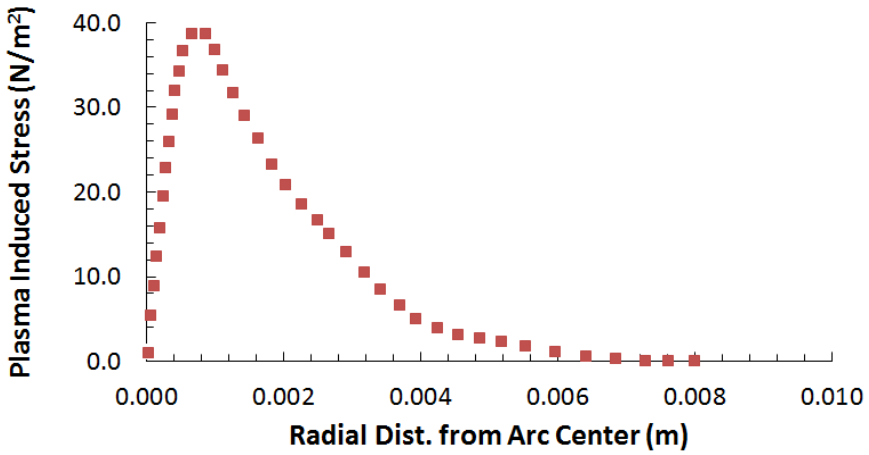


Figure 3.2: Plasma induced shear stress distribution on weld pool surface.

The plasma induced shear stress is zero at the arc center, and abruptly increases its maximum at the radial distance near the center, and then rapidly decreases to zero. The maximum outward shear stress increases with the increasing welding current.

### 3.5 Coupled Weld Arc-Pool

A significant amount of work is also done in the field of coupled welding arc and weld pool modeling and simulation. Such unified modeling is necessary in order to consider the gas shear due to impinging plasma arc force over the free weld pool surface. Choo et al. [59] developed a mathematical formulation to describe the temperature profiles in GTA welding arcs and thereby computed the net heat flux from the welding arc to the weld pool. They did so by coupling the Maxwell's equations, Navier-Stokes equations and the thermal energy balance equation. Their model was based on the assumptions of steady, axi-symmetric laminar flow. This welding arc model was combined with the weld pool model by Choo et al. [72] to represent the interaction between welding arc and the weld pool. Their model was developed for spot welding with flat top surface of weld pool. They used constant thermophysical properties, and the temperature coefficient of surface tension was treated to be a function of temperature and activity. They used the commercial package PHOENICS for their simulations. Tanaka et al. [73] developed a model encapsulating tungsten cathode, arc plasma, workpiece, and weld pool for a stationary TIG. Using assumptions of a flat weld pool surface and constant surface tension gradient, they made steady state calculations and predicted the two-dimensional distributions of temperature and velocity in the whole region of TIG welding process. They extended their work by identifying that apart from the arc current, another principle parameter for welding is the arc length, and developed a two-dimensional model to investigate [74] the effects for arc length less than 10mm. They observed that on increasing the arc length, for constant arc current, increased the total power to the anode, but decreased the heat flux density to the anode due to decreased current density. Yamamoto et al. [75] used a unified numerical model incorporating the tungsten cathode, the arc plasma and the weld pool to take into account the contamination of the plasma by the metal vapor from the weld pool surface. They observed differences in the peak current distribution for the anode.

Recently, Dong et al. [76, 77] used the ANSYS FLUENT commercial CFD software to model the welding arc and weld pool together. Using their unified model, they systematically investigated the effect of active element oxygen on the Marangoni convection and weld shape. The weld shape and depth-to-width ratio from the numerical model were compared with the experimental one. They reported that under high oxygen content, the depth/width ratio substantially depended on the welding parameters. High welding speed and larger arc length decreased the depth/width ratio. Under the low oxygen content, the weld D/W ratio slightly decreases with the increasing welding current. Using their unified welding arc-pool model, they also calculated the radial distribution of heat flux, current density and plasma induced shear stress on the anode surface.

### 3.6 Turbulent Weld Pool

From previous literature it has been found that almost all researchers characterized the weld pool fluid flow as Newtonian, laminar and incompressible. The reason being that in case of GTA welding the current is practically below or around 200A, and hence the laminar assumption seemed reasonable. Since weld pool convection is dominated by Marangoni effects, a Reynolds number may be defined based on the maximum surface velocity (as the characteristic velocity scale) and the pool width (as the characteristic length scale in the transverse direction of fluid flow). Accordingly, the Reynolds number can be defined as $\mathrm{Re} = \rho w_{\max} b / \mu$, where $w_{\max}$ is the maximum velocity in the direction perpendicular to the weld axis and $b$ is the width of the weld pool. Chakraborty et al. [78] mathematically modeled turbulent weld pool convection in GTA welding process with high power, where the effects of turbulent transport can actually be realized. They follow that for high power TIG welding the onset criterion for turbulence is when the surface tension Reynolds number is greater than 100. This criterion was used by Aboutalebi et al. [109]. Chakraborty et al. [79] also modeled turbulent weld pool convection in three-dimensions using a high Reynolds number k-ε model. Since it is difficult to establish the exact value of a critical Reynolds number theoretically, they chose a sufficiently high range of Reynolds numbers (of the order of 3000) in order to carry out their studies of turbulence in welding. In their study, they found the turbulent weld pool to be shallower than the laminar one. Chakraborty [24] studied the effects of the sign of surface tension coefficient on both laminar

and turbulent weld pool convection in a GTA welding process. They report that due to enhanced mixing in a turbulent pool, the mean convective effect becomes weaker and tends to reduce the pool penetration in case of positive surface tension coefficient. However, an effective enhancement in diffusion tends to increase the pool depth. These two counteracting mechanisms compete in deciding the final pool depth. They studied the Marangoni flow reversal in detail for both laminar and turbulent flows.

### 3.7 Heat Input Influence on Microstructure and Mechanical Properties of Welded Joints

Chen et al. [110] found that when Cu-Si enriched type 304 SS and a conventional type 304 SS was welded using GMAW, the process ductility decreased and ferrite levels increased in both weldments, as the heat input was increased. Yan et al. [111] performed a comparative study on the microstructure and mechanical properties of 304 SS joints by TIG welding, laser welding, and laser-TIG hybrid welding. Their work showed that laser welding could give highest tensile strength and smallest dendrite size in all joints whereas TIG welding gave lowest tensile strength and biggest dendrite size. Muthupandi et al. [112] conducted research on the effect of weld chemistry and heat input on the structure and properties of duplex stainless steel welds using autogenous-TIG and electron beam welding. They showed that chemical composition exerts a greater influence on the ferrite-austenite ratio than the cooling rate. Jana [113] reported the effect of varying heat input on the properties of the HAZ of two different duplex steels and found that as the arc energy increased the hardness of both weld metal and the HAZ decreased. They also reported that the width of the HAZ increased with increased arc energies. Nowacki et al. [114] studied the influence of welding heat input on submerged arc welding welded duplex steel joints imperfections. They used heat input from 2.5 to 4.0 kJ/mm for plate thickness of 10-23mm. They concluded that usage of larger welding heat input provided the best quality joints.

Zumelzu et al. [115] studied the mechanical behavior of AISI 316L welded stainless steel joints using shielded metal arc welding (SMAW) and GMAW process with different electrode types. They concluded the existence of a direct correlation between the thermal contribution and tensile strength of the material studied. Durgutlu [116] carried experimental investigations on the effect of hydrogen in argon as a shielding gas in the TIG welding of austenite stainless steel. It

was demonstrated that the mean grain size in the weld metal increased with increasing hydrogen content besides the increase in the weld metal penetration depth and width. Lee et al. [117] reported in their studies the effects of strain rate and failure behavior of 304L SS SMAW weldments. They found that as the strain rate increased, the flow stress increased and the fracture strain decreased. Korinko et al. [118] reviewed the considerations for weldability of 304L SS and recommended $Cr_{eq}/Ni_{eq}$ ratio of 1.52-1.9 for better control of the primary mode of solidification. Lee et al. [119] investigated the pitting corrosion behavior of welded joints of AISI 304L using fluxed core arc welding process. They found that tensile and yield strengths were increased with increasing equivalent ratio of $Cr_{eq}/Ni_{eq}$. Milad et al. [120] found that the yield and tensile strengths of 304SS increased gradually at the same rate with increasing degree of cold work. Shyu et al. [121] investigated the effect of oxide fluxes on weld morphology, arc voltage, mechanical properties, angular distortion, and hot cracking susceptibility of autogenous-TIG bead on plate welds. They showed that penetration is significantly increased which in turn increased the depth to bead width ratio and reduced angular distortion. Kumar et al. [122] studied the influence of heat input on the microstructure and mechanical properties of GTA welded 304 SS joints. They performed microstructural evaluations for low, medium, and high heat input per unit length of the weld. Their resulted showed that joints made using low heat input exhibited higher ultimate tensile strength than those welded with medium and high heat input. They observed grain coarsening in the HAZ for all the joints, with extent of grain coarsening increasing with increase in heat input. It was seen that with increased heat input the dendrite size and inter-dendrite spacing in the weld metal also increased. Based on their study, they recommended employment of low heat input when welding AISI 304SS using GTAW as it gives good tensile strength and ductility, smaller HAZ, and less grain coarsening in the weld joints.

Other studies on 304 SS and 304L SS grade has been performed by many researchers. Studies include experimental determination of grain boundary composition of 304 SS in low temperature sensitization condition [123], chromium depletion measurement after thermal heat treatments [124], modeling of low temperature sensitization of austenitic stainless steel [125], sensitization behavior study of grain boundary engineered austenitic stainless steel [126], etc.

### 3.8 Structural Analysis of Welded Joints through Simulations

The mechanical response of welds is sensitive to the close coupling between weld pool dynamics, thermal energy distribution, microstructure evolution and mechanical (deformation/stress) behavior (Fig. 3.3). The solid arrows denote strong coupling and the dotted arrows denote weak coupling. The weld pool dynamics-thermal fields are two-way coupled, whereas the thermo-mechanical, thermo-metallurgical, and metallurgical-mechanical fields are all one-way coupled.

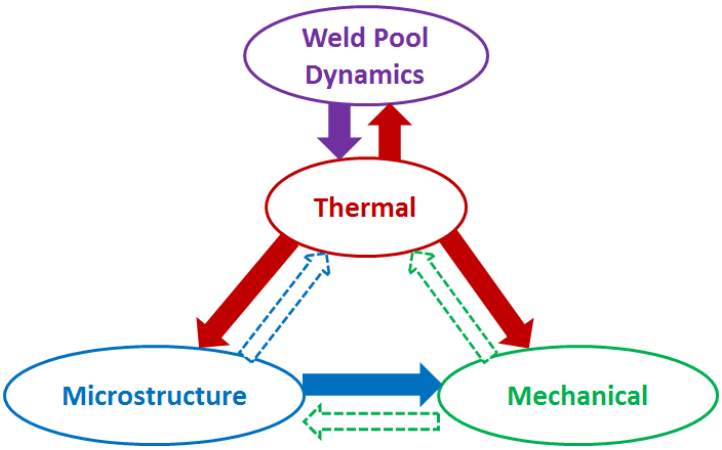


Figure 3.3: Weld pool dynamics integrated coupled fields in a welding process.

When the objective of the analysis is to determine the thermal effects of welding on mechanical response (i.e. residual stress and distortions) the simplest approach is to consider the one-way thermo-mechanical coupling only. Using this simplistic approach, numerical analysis of thermal stresses in welded joints has been studied over the years [89, 90]. The thermal and mechanical simulations of spot welding were carried out by Sheppard [91]. It was suggested that the predictions could be extended to other manufacturing processes which involve spot welding. Sluzalec [92] studied the thermal effects in friction stir welding (FSW). The finite element method (FEM) was used to simulate the temperature and stress fields. Khandkar and Jamil [93] predicted thermal stress developments under FSW. The predictions however did not deal with the severe plastic deformation in the welding region. Lin and Lee [94] studied the effect of the

welding parameters on the residual stress formation in welding. The results indicated that parallel heating did not increase the width of the heat affected zone (HAZ) and the grain coarsening. Yang and Xiao [95] performed an elasto-plastic modeling of residual stress under welding. They showed that as the depth of the yield zone increased, the location of the maximum residual stress changed. Canas et al. [96] performed a numerical analysis of residual stress using the finite element (FE) code ABAQUS. They used a plane stress model to determine the residual stress distribution. Transient three-dimensional thermal stress analyses of welds have been described in detail in several papers [9-99]. Yuan and Sun [100] investigated the transient temperature and stress fields using FEM during welding of metallic materials. The welding deformation at the heated zone was predicted from the temperature field using FEM by Murakawa et al. [101]. Using FEM, Chidiac and Mirza [102] predicted stress fields in the weldments. They found that the longitudinal stress component was as high as the yield strength of the substrate material. Sunar et al. [103] conducted two-dimensional numerical thermal and stress analysis of a sheet metal under welding. They considered a constant temperature heat source along the weld line. They found that temporal changes in the temperature gradient induce stresses in the substrate material. Also, maximum value of the von-Mises stress was less than the yield strength of the substrate material. Recently, Kong and Kovacevic [104] developed a finite element model for the thermally induced residual stress analysis of a hybrid laser/arc welded lap joint. They found that increasing the welding speed causes the penetration and width of the weld bead to decrease, and the thermal stress concentration at the welded joint also reduces accordingly. In all these studies, the strong two-way coupled weld pool dynamics-thermal fields has not been considered, i.e. heat redistribution and change in the HAZ due to convective driving forces in the molten weld pool have not been considered.

Previous research on weld pool dynamics effects has clearly shown that surface tension gradient induced flow (due to presence of surface active agent), electromagnetic force, plasma induced stress on weld pool surface, buoyancy, and heat input per unit length of the weld (determined by welding parameters like current, welding speed, etc.) influence the development of the HAZ. The nature and extent of the HAZ influences the developed thermal stresses in the weld structure. In a standalone thermo-mechanical analysis there has been only a few papers that have included the effects of fluid flow in weld pools. Sheng and Chen [129, 130] developed a mathematical model to describe the temperature distribution, flow in the molten fluid and stress

field in the solid during welding. In their analysis, the workpiece during welding is assumed to have three zones: the pure solid, the pure fluid, and the solid-fluid mixture. They used volume fractions to define the territories of each zone. They developed a fully coupled energy equation, incorporating the dilatation work, the plastic work in the solid phase, the mechanical work done by the molten fluid, and the latent heat of the phase. Their mathematical model was implemented using an in-house finite element code. Their simulations showed the location of the maximum residual stress in the neighborhood of the solidification boundary.

A number of numerical models have been developed to predict the welding residual stresses considering the metallurgical-mechanical coupled fields, i.e. microstructure change/phase transformation effects on mechanical behavior. Leblond and Devaux [131] and Leblond et al. [132, 133] presented a kinetic model for metallurgical transformations in steels and the constitutive model for the plastic behavior of steels during phase transformations, respectively. Oddy et al. [134, 135] developed a relation for transformation plasticity, not relying on empirical constants, and proposed a method to incorporate transformation plasticity in a FE program based on the relation and basic material properties. Ronda et al. [136] developed a thermo-mechano-metallurgical (TMM) model which included melting, solidification and solid phase transformations during welding. Recently, Kim et al. [137] conducted a systematic numerical implementation of the thermo-elastic-plastic constitutive equation. Deng and Murakawa [138] investigated the influence of solid-state phase transformation on the evolution of residual stress distribution in butt-welded steel pipes using a thermal elastic-plastic FE model which took into account the metallurgical phase transformation. Lee [139] presented a three-dimensional one-way coupled thermo-mechanical FE model which took into account the effects of solid-state phase transformation on residual stresses. Their results showed that the volumetric change due to the austenitic to martensitic phase transformation significantly affected the residual stresses in the transformation region. They also extended their work to high strength carbon steel butt welds [140].

### 3.9 Present Investigation: Coupled Field Analysis of GTA Welded Butt Joints

To the best of our knowledge, there are no detailed numerical studies on the coupled weld pool dynamics-thermo-metallurgical-mechanical analysis of a welded joint. In the present investigation, an attempt is made to study such a coupled field analysis of welding through numerical modeling and simulation. The most widely used welding process used in industries is GTA welding, and is chosen for the present study. The three-dimensional numerical model developed is for thin butt-joint plates, specifically less than 5mm in thickness, so that autogenous GTA welding can be employed, i.e. use of filler material is not necessary [44]. The plate material is austenitic steel, specifically type 304 SS grade. Out of the 300 series grade of austenitic steels, type 304 SS is extensively used in industries due to its superior low temperature toughness and corrosion resistance. The coupled weld pool dynamics-thermal model takes into account all the major driving forces and fluid flow in the molten pool. The model also includes the effects of electrode angle and arc length on the anodic heat flux and current density distributions. Temperature dependent thermophysical properties are used in the simulations for a more accurate estimation of weld D/W ratio and temperature field prediction of the workpiece. The coupling of the weld pool dynamics-thermal models with the microstructure evolution is achieved through material modeling, and made part of the overall solution in the determination of mechanical response of welded structures. In material modeling, the material properties are defined as a function of both temperature and microstructure change. Such an analysis would indirectly incorporate microstructural aspects in the material description through the exploitation of microstructure dependency on temperature and deformation [127, 128 and 141]. For austenitic steels and Inconel, the effect of microstructure/phase changes on mechanical behavior may be reasonably ignored [128, 141]. Hence, in the present investigation, mechanical properties like yield strength is expressed as a function of temperature only. Such an approach helps to achieve the desired coupled weld pool dynamics-thermo-metallurgical-mechanical analysis of a welded joint. It is to be noted that for performing such coupled field analysis of GTA welding of other materials, the mechanical properties need to be expressed as a function of both microstructure change and temperature. The mathematical framework developed here serves as a robust tool for better quantification of thermal stress evolution, residual stress distribution, and distortion in a welded structure.

# Chapter 4

# Modeling and Simulation of GTA Welding

## 4.1 Introduction

In GTA welding, a localized intense heat source (arc) is moved along the joint and this result in the melting and subsequent solidification of the adjacent areas of the two parts. Here, the thermal energy from the arc is transferred to the workpiece, causing it to melt, forming the molten region known as the weld pool. Subsequent solidification of the weld pool forms the weldment or actual joint. The GTA welding transport processes are: (i) heat and current flux distributions to the weld pool, (ii) interaction of the arc with the free surface and possible surface deformation, (iii) convective heat transfer due to fluid flow in the weld pool, (iv) thermal conduction into the solid workpiece, (v) convective and radiative heat losses, (vi) transient solidification and melting, (vii) electromagnetic stirring due to divergent current path, (viii) thermocapillary or Marangoni convection due to surface tension gradient, (ix) plasma induced shear stress, and (x) buoyancy in the weld pool. Figure 4.1 highlights the schematic model for the moving GTA welding process and highlights the coordinate system. The gas tungsten arc moves along the z-axis and hence the problem is symmetric about the yz-plane.

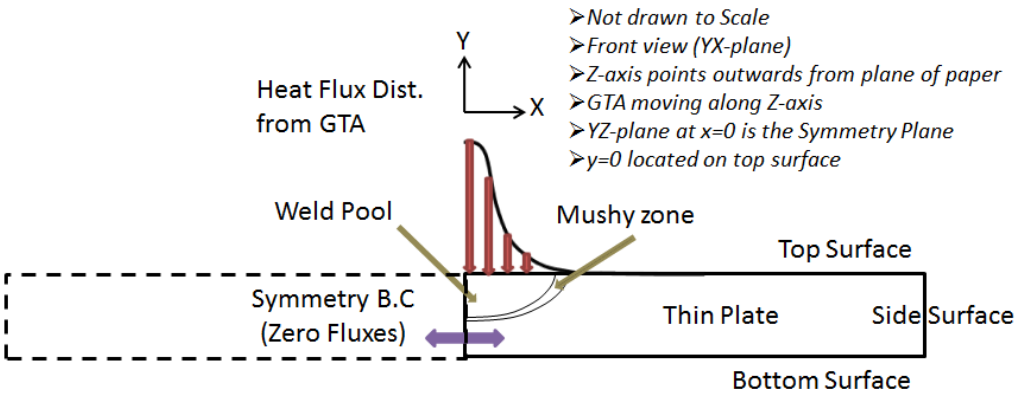


Figure 4.1: Schematic of a moving GTA welding process.

Two main concerns in GTA welding are (a) ability to predict the D/W ratio of the weld and (b) determination of the thermally-induced residual stresses in the welded structures. It has been found that conduction and convection in the weld pool determines how the weld shape develops. While conduction depends on the properties of the metal plates being joined, the convection in the weld pool is determined by the various driving forces. Hence, quantification of relative convection modes, their nature and strength, would help accurately determine the thermal profiles in the welded joint. Due to the moving arc, a very large temperature variation occurs over a small region. Consequently, significant thermally induced stresses get generated in the welded structure due to the temperature gradients, which tends to cause defects such as crack formation and fractures. The region being heated tends to be in compression and the region being cooled tends to be in tension. The thermal stress analysis of welds is difficult because of the geometry changes and due to the complex stress-strain relationship. Modeling stresses in the welds includes all distortions that can be predicted by thermal stress analysis. Residual stress and distortion of welds are strong functions of plasticity. Most thermal stress analyses of welds conducted have used thermo-elastic-plastic constitutive models with rate independent plasticity.

## 4.2 Mathematical Model

### 4.2.1 Weld Pool Dynamics Modeling

The melting/solidification problem is handled using the enthalpy-porosity formulation [106], which helps to track the liquid/solid interface in the weld pool. By treating the liquid/solid mushy zone as a porous zone, with the porosity equal to the liquid fraction, it is possible to account for the melting/solidification through the introduction of a momentum sink term in the Navier-Stokes (N-S) equations. Hence, the mushy zone is a region in which the liquid fraction lies between 0 and 1. The governing equations for continuity, momentum and energy, developed on the assumptions of incompressible, laminar flow in the weld pool, are given by

Continuity:

$$\overline{\nabla} \cdot \vec{V}=0 \tag{4.1}$$

Momentum:

$$\rho\frac{\partial\vec{V}}{\partial t} + \rho(\vec{V}\cdot\overline{\nabla})\vec{V} = -\overline{\nabla}p + \mu\nabla^2\vec{V} + A_m\vec{V} + \vec{j}\times\vec{B} + S_b \tag{4.2}$$

Energy:

$$\frac{\partial}{\partial t}(\rho H) + \nabla\cdot(\rho\vec{V}H) = \nabla\cdot(k\nabla T) + S_h \tag{4.3}$$

where $\vec{V} = u\vec{e}_x + v\vec{e}_y + w\vec{e}_z$ is the fluid velocity, $\rho$ is the density, $p$ is the pressure, $\mu$ is the dynamic viscosity, $\vec{j}$ is the current density vector, $\vec{B}$ is the magnetic flux vector, $A_m\vec{V}$ is the momentum sink term to account for the mushy zone, where

$$A_m = -C(1-f_L)^2/(f_L^3+\varepsilon') \tag{4.4}$$

where, C is the mushy zone constant, $\varepsilon' = 0.001$ (included to avoid division by zero), $H$ is the enthalpy, $S_h$ is the phase related enthalpy source term, $f_L$ is the liquid fraction, and $S_b$ is the buoyancy source term. We note that $\vec{j}\times\vec{B}$ represents the electromagnetic Lorentz force. The enthalpy $H$ can be decomposed into the sum of sensible enthalpy, $h$ and the latent heat content, $\Delta H$ where

$$h = h_{ref} + \int_{T_{ref}}^{T} c_p dT \tag{4.5}$$

where, $h_{ref}$ is the reference enthalpy, $T_{ref}$ is the reference temperature, $c_p$ is the specific heat at constant pressure, and the latent heat content $\Delta H = f_L L$, where $L$ is the latent heat of the material. Liquid fraction, $f_L$ is defined as

$$f_L = (T - T_{solidus}) / (T_{liquidus} - T_{solidus}) \tag{4.6}$$

$$f_L = 0, \text{ if } T < T_{solidus}$$

$$f_L = 1, \text{ if } T > T_{liquidus}$$

The electromagnetic (Lorentz) force, $\vec{F}_L (= \vec{j} \times \vec{B})$, appears as a body force term in the N-S equation and can be obtained by solving the current continuity equation in association with the steady state version of the Maxwell's equation in the domain of the workpiece for the current density and magnetic flux.

Current Continuity:

$$\nabla^2 (\sigma_e \phi) = 0 \tag{4.7}$$

where, $\sigma_e$ (=7.14x10$^5$ $\Omega^{-1}$m$^{-1}$) is the electrical conductivity of the workpiece and $\phi$ is the electric potential. In order to solve Eq. (4.7), the current density distribution from the arc on the top surface of the anodic workpiece is considered as a boundary condition. Upon solving Eq. (4.7) in the domain of the workpiece, the current density can be obtained as

$$\vec{j} = -\sigma_e \nabla \phi \tag{4.8}$$

Maxwell's equations:

$$\overline{\nabla} \cdot \vec{E} = \rho_e / \varepsilon_0 \tag{4.9a}$$

$$\overline{\nabla} \cdot \vec{B} = 0 \tag{4.9b}$$

$$\overline{\nabla} \times \vec{E} = -\partial \vec{B} / \partial t \tag{4.9c}$$

$$\overline{\nabla} \times \vec{B} = \mu_0 \varepsilon_0 \, \partial \vec{E} / \partial t + \mu_0 \vec{j} \cong \mu_0 \vec{j} \tag{4.9d}$$

where, $\vec{E}$ is the electric field, $\rho_e$ is the electric charge density, $\varepsilon_0$ (=8.8542x10$^{-12}$ F/m) is the permittivity of the free space and $\mu_0$ (=4πx10$^{-7}$ Wb/A-m) is the permeability of free space. The magnetic flux vector can be defined as

$$\vec{B} = \nabla \times \vec{A} \tag{4.10}$$

where, $\vec{A}$ is the magnetic vector potential, and using Eq. (4.9b) in combination with vector calculus identities, Eq. (4.9d) can be represented as

$$-\nabla^2 \vec{A} = \mu_0 \vec{j} \tag{4.11}$$

On obtaining the solution of Eq. (4.11) using Eq. (4.8), the magnetic flux vector can be obtained using Eq. (4.10), and takes the form

$$\vec{B} = \hat{i}\left(\frac{\partial A_z}{\partial y} - \frac{\partial A_y}{\partial z}\right) + \hat{j}\left(\frac{\partial A_x}{\partial z} - \frac{\partial A_z}{\partial x}\right) + \hat{k}\left(\frac{\partial A_y}{\partial x} - \frac{\partial A_x}{\partial y}\right) \tag{4.12}$$

The electromagnetic (Lorentz) force is then calculated by taking the cross product of $\vec{j}$ and $\vec{\mathrm{B}}$, and the x, y, and z-components of the Lorentz force are

$$\mathrm{F_{Lx}} = j_y \mathrm{B}_z - j_z \mathrm{B}_y \tag{4.13a}$$

$$\mathrm{F_{Ly}} = j_z \mathrm{B}_x - j_x \mathrm{B}_z \tag{4.13b}$$

$$\mathrm{F_{Lz}} = j_x \mathrm{B}_y - j_y \mathrm{B}_x \tag{4.13c}$$

Eq. (4.13a, b, c) are used in the x, y, z-components, respectively, of the momentum equation.

### 4.2.2 Structural (Stress) Analysis Modeling

The relationship used in the finite element solver for the structural analysis is given by

$$[K]\{\vartheta\} = \{F\} \tag{4.14}$$

where, $[K]$ is the stiffness matrix, $\{\vartheta\}$ is the displacement matrix, and $\{F\}$ matrix denotes the loads/constraints. For a nonlinear analysis, the stiffness becomes a function of the applied load. Hence, Eq. (4.14) is solved iteratively until convergence is reached. The Newton-Raphson method is employed for the iterative process (details are given in Section 4.3.1). Non-linearity in a structure occurs if the loading causes significant changes in stiffness. For the present problem of welding of thin plates we consider geometric and material nonlinearities. Generally, during welding process, besides elastic, plastic and thermal strains, strains due to solid-state phase transformations and creep can potentially give some contribution to the total strain. As austenitic SUS304 stainless steel has no solid-state phase transformation during cooling, the total strain at a material point can be expressed as the summation of elastic, plastic and thermal strain only. The thermal elastic-plastic constitutive equations used in the mechanical (stress) simulation (ANSYS Inc., 2012) analysis are

$$[d\sigma] = [D^{ep}][d\varepsilon] - [D^{th}]dT \tag{4.15a}$$

$$[D^{ep}] = [D^{e}] + [D^{p}] \tag{4.15b}$$

where, $d\sigma$ is the stress increment, $d\varepsilon$ is the strain increment, $dT$ is the temperature increment, $[D^e]$ is the elastic stiffness matrix, $[D^p]$ is the plastic stiffness matrix, and $[D^{th}]$ is the thermal stiffness matrix. The structural analysis model is developed based on isotropic material behavior and hence the thermal strains can be represented as

$$\varepsilon_{th}^{x} = \varepsilon_{th}^{y} = \varepsilon_{th}^{z} = \beta(\mathrm{T} - \mathrm{T}_{\mathrm{ref}}) \tag{4.16}$$

where, $\beta$ is the thermal expansion coefficient, and $\mathrm{T}_{\mathrm{ref}}$ is the temperature where thermal strain is zero, i.e. the workpiece is stress free. In the FE solver, elasticity is modeled using the isotropic Hook's rule with temperature dependent Young's modulus and Poisson's ratio, and the plasticity is defined using a rate-independent plastic model with temperature dependent yield stress. The FE code utilizes an isotropic hardening model to consider the material strain-hardening behavior.

As for the assumptions that are built into this model, we have neglected influences from the arc pressure and assumed a flat weld pool surface (i.e. negligible surface deformation). Arc pressure in GTA welding is due to the momentum transfer of the impinging plasma jet on the weld pool. Since operating current for GTA welding is below 220A, the effect of arc pressure is negligible [44, 68-70] and therefore, deformable weld pool surface need not be considered. Further, when considering partial penetration of the workpiece, surface depression can be regarded as negligible if the welding current is less than 200A [48, 52, 54]. Ko et al. [54] verified that the depression of the molten pool free surface is mainly due to arc pressure and to some extent due to the inward circulation due to current, validating the work done by Lin and Eagar [70]. It has been determined that the dynamic balance between arc pressure, buoyancy force, and the surface tension force determines the ultimate shape of the weld pool surface [52]. Also, it is to be noted that when the welding current is less than 160A, the plasma induced shear stress is negligible [71].

### 4.2.3 Boundary Conditions for Weld Pool Dynamics

The various boundary conditions applied on the different faces of the workpiece are highlighted below (refer Fig. 4.1).

*Top Surface*: The velocity boundary condition is specified in terms of the shear stresses as $\tau_{TopSurf} = \tau_{STG} + \tau_{PIS}$, where $\tau_{STG}$ represents shear stress due to surface tension gradient, and $\tau_{PIS}$ represents the plasma induced shear stress on the weld pool surface. Hence, the velocity boundary condition takes the form

$$-\mu \frac{\partial u}{\partial y} = \frac{\partial \gamma}{\partial T} \frac{\partial T}{\partial x} \tag{4.17}$$

$$-\mu \frac{\partial w}{\partial y} = \frac{\partial \gamma}{\partial T} \frac{\partial T}{\partial z} \tag{4.18}$$

where, $\partial\gamma/\partial T$ is given by Sahoo et al. [16]. It is a relation for the temperature coefficient of surface tension of the metal-solute (*i*) alloys as a function of the surface temperature, $T$ and activity $a_i$:

$$\frac{\partial \gamma}{\partial T} = -A_g - R\Gamma_s \ln(1+Ka_i) - \frac{ka_i}{1+ka_i} \frac{\Gamma_s \Delta H^0}{T} \tag{4.19}$$

where, $A_g$ is the negative of $\partial\gamma/\partial T$ for pure metals, $R$ is the gas constant, $\Gamma_S$ is the surface excess solute concentration at saturation, $a_i$ is the activity of species '*i*' in %wt., $\Delta H^0$ is the standard heat of adsorption, and $K$ is the adsorption coefficient. The adsorption coefficient, in turn, is given by:

$$K = k_1 \exp(-\Delta H^0/RT) \tag{4.20}$$

where $k_l$ is a constant related to the entropy of segregation. Examples of surface active elements in stainless steel are sulphur (S), oxygen (O), etc. The values of $\Gamma_s$, $\Delta H^0$, and $k_l$ would change with different surface active element, thereby generating different $\partial\gamma/\partial T$ variations with T and $a_i$. From Eq. (4.19) we find that $\partial\gamma/\partial T$ is negative for pure metals ($a_i$=0) and its variation is plotted in Fig. 4.2. It can be seen that the surface tension gradient changes from a positive to a negative value beyond a critical temperature for any particular surface active element content. The critical temperature at 20ppm is ~1960K and at 100ppm is ~2220K. The heat input per unit length of the weld, determined by welding parameters like welding current, welding speed, etc. will influence the temperature distribution on the weld pool surface and hence dictate the surface tension gradient sign change for any particular surface active agent content.

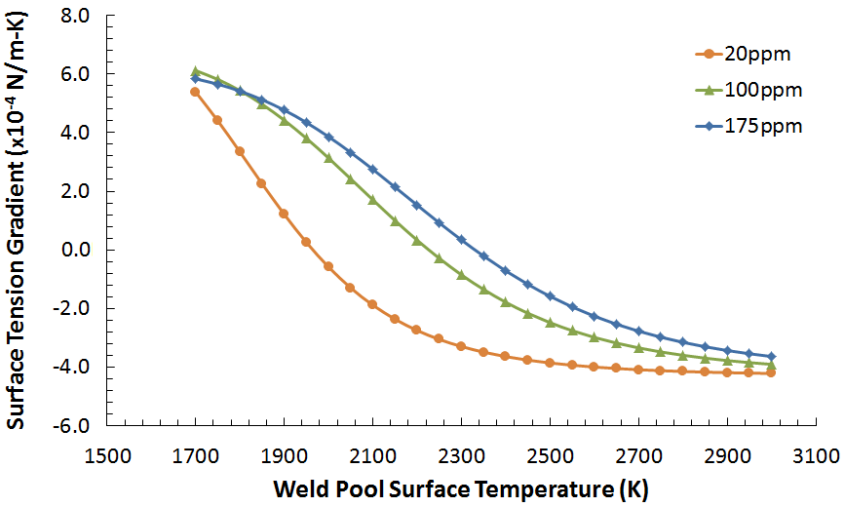


Figure 4.2: Surface tension gradient variation on weld pool surface with temperature.

Dong et al. [76] showed that the plasma induced shear stress increases linearly near the weld pool surface center and then drops off quickly. The plasma induced shear stress on the weld pool surface in the drop off region can be represented by

$$\tau_{PIS} = P_{SS,max} \exp\left\{-\frac{f_P \zeta'^2}{\pi \sigma_P^{\,2}}\right\} \tag{4.17}$$

where, $P_{SS,max}$ is the maximum value reached in the linear rise region, $\zeta'$ represents the x- and z- coordinate system, $f_p$ is the shape factor, and is the distribution parameter in the drop off region. The slope of the abrupt rise portion of the distribution increases with increase in current. Figure 4.3 show the plasma induced stress distribution on the weld pool surface.

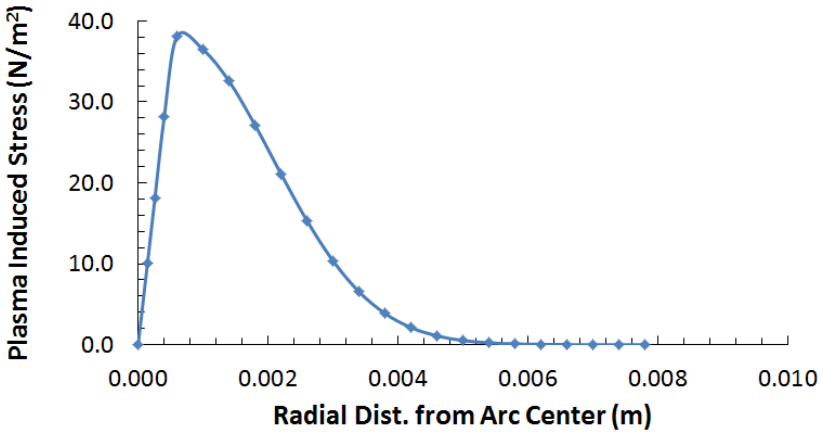


Figure 4.3: Plasma induced shear stress distribution on the weld pool surface, at 200A welding current and 3mm arc length.

The thermal boundary condition is defined in terms of the heat flux, and is described by

$$q = q_{arc} - \varepsilon_r \sigma_b (T^4 - T_{amb}^4) - h_c (T - T_{amb}) \tag{4.18}$$

where, $\varepsilon_r$ is the radiation emissivity, $\sigma_b$ is the Stefan-Boltzmann constant ($5.67 \times 10^{-8}$ W/m$^2$K$^4$), $T_{amb}$ is the ambient temperature, $h_c$ is the convective heat transfer coefficient and $q_{arc}$ is the arc heat flux distribution on the anodic workpiece, given by

$$q_{arc} = \frac{\eta_a VI}{P_{kq}\pi\sigma_q'^2}\exp\left\{\frac{-f_q\zeta^2}{\pi\sigma_q'^2}\right\} \tag{4.19}$$

where, $\eta_a$ is the arc thermal efficiency, $V$ is the welding voltage, $I$ is the welding current, $\sigma_q'$ is the modified arc heat flux distribution parameter, $f_q$ is the shape factor and $P_{kq}$ is the peak value adjustment factor. The second and third terms on the right hand side of Eq. (4.18) represent the heat loss due to radiation and convection, respectively. The current density distribution on the anodic workpiece has a similar formulation as Eq. (4.19), and is represented as

$$j = \frac{I}{P_{kj}\pi\sigma_j'^2}\exp\left\{\frac{-f_j\zeta^2}{\pi\sigma_j'^2}\right\} \tag{4.20}$$

where, $\sigma_j'$ is the modified current density distribution parameter, $f_j$ is the shape factor and $P_{kj}$ is the peak value adjustment factor. The modified distribution parameter incorporates the effects of arc length and electrode angle, and is given by $\sigma_i' = \sigma_i + (60^o - \alpha) * c_i * \sigma_i / 180$, where *'i'* represents both heat flux and current density distributions respectively, α is the electrode angle in degrees, $\sigma_i$ is the distribution parameter [107] as shown in Fig. 4.4 and Fig. 4.5, and $c_i$ is the % change in $\sigma_i$.

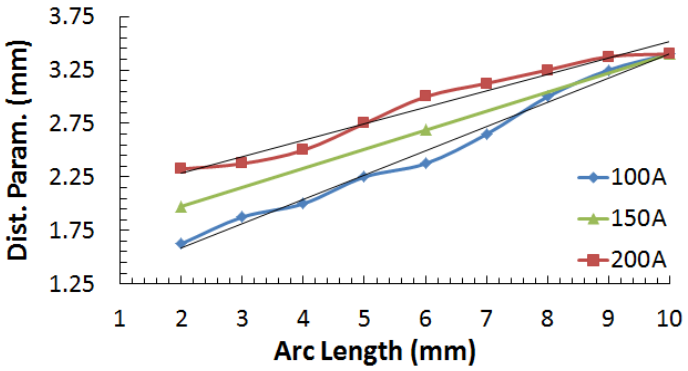


Figure 4.4: Heat flux distribution parameter vs. arc length, at different welding currents.

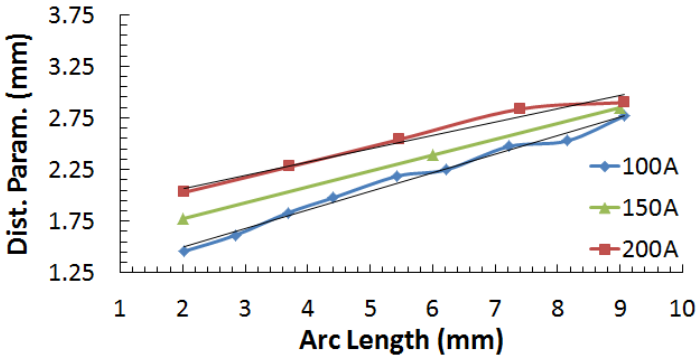


Figure 4.5: Current density distribution parameter vs. arc length, at different welding currents.

*Symmetry Surface*: A symmetry surface implies that the flow, temperature and pressure gradients are identically zero along the specified face (Fig. 4.1). Hence, physical conditions in the regions immediately adjacent to either side of the face are identical to each other. Hence, the appropriate boundary conditions are the zero flux conditions.

$$\frac{\partial T}{\partial x}=0, \frac{\partial v}{\partial x}=0, \quad \frac{\partial w}{\partial x}=0, \; u=0, \; \frac{\partial \phi}{\partial x}=0 \tag{4.21}$$

*Other Surfaces*: At all other surfaces, velocities are set to zero and for the thermal boundary condition, temperatures are set at ambient. The bottom surface of the workpiece for the electric potential is electrically isolated and hence current density is set as zero. As for the remaining three side surfaces, as the electrical conductivity of the workpiece is very high and these surfaces being far enough from the weld pool, it is assumed that the electrical potential at these surfaces is zero.

### 4.2.4 Boundary Conditions for Structural (Stress) Analysis

Since the problem is symmetric about the weld line, stress analysis is also performed for only one-half of the workpiece, utilizing the symmetry boundary condition. The boundary conditions used for the structural analysis are as follows (refer Fig. 4.6)

Surface ABCD: This surface is the symmetry face. It is prevented from moving or deforming in the normal direction, thus representing an equivalent symmetry condition. It is defined as a frictionless face in the FE solver.

Edges AA', BB', CC', and DD': These edges are fixed, i.e. they cannot move or deform. However, rotation is permitted about the edges, i.e. the plate can bend. This constraint is equivalent to clamping the edges, thus holding the two workpieces together.

Other Surfaces: They have no constraints defined and are hence free to move or deform under the thermal load.

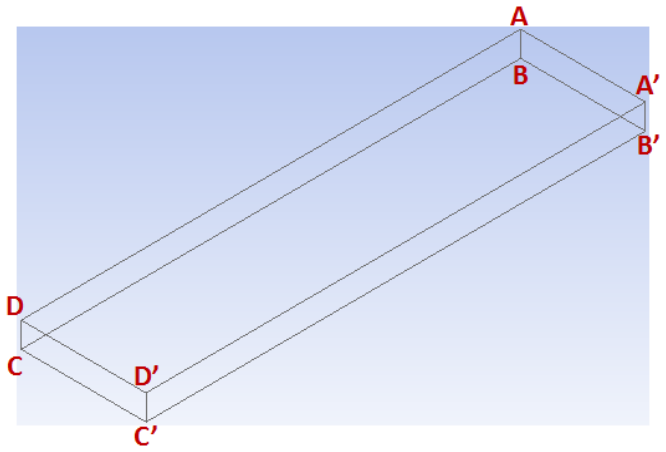


Figure 4.6: Structural analysis boundary conditions definition.

### 4.2.5 Initial Conditions

As for the weld pool dynamics modeling, it is assumed that the workpiece is initially at a uniform temperature distribution, given by $T_{init}$. For the structural (stress) analysis, it is assumed that the workpiece is initially stress-free.

## 4.3 Numerical Modeling and Simulation

### 4.3.1 Introduction

Computational Fluid Dynamics (CFD) is the technology used for the mathematical study of the dynamics of flow. CFD helps to bridge the gap between pure theory and pure experiment, and gives an alternative approach to solve fluid dynamics problems. It utilizes computational power to perform numerical calculations, aiding the interpretation of results without actually conducting experiments, thereby reducing cost and time. CFD is based on numerical techniques by which the solution domain is discretized into nodes, and using discretization schemes the conservation equations are transformed into algebraic ones. Hence, at the core of any CFD calculation there is a computational grid, dividing the solution domain into elements where the problem variables are computed.

Modeling and numerical simulation of weld pool dynamics are increasingly being used by researchers in the field. A recent trend has been to use commercially available software platforms to model and simulate the weld pool dynamics. An alternative route is for research groups to develop computer codes in-house, which is becoming more and more impractical because of code development times spanning over several years, and resources which can be often be counted in person years. While the codes developed by the researchers themselves have advantages such as familiarity with all aspects of the computer code, there are also disadvantages in terms of lack of robustness and ease of use. Many widely used commercial simulation packages allow the user to have greater flexibility in terms of choice of models. Users have the option to use their own models, when the built-in models are not satisfactory. A widely used commercial flow solver is ANSYS FLUENT®, which has been used for the present simulations of weld pool dynamics based on the following considerations: (i) availability of numerical algorithms to do time-accurate simulations of transient phenomena, (ii) availability of a suite of numerical algorithms that can be chosen depending on the users' need for robustness and order of accuracy, (iii) excellent user interface that enables the user to include alternate models via user-defined functions (UDFs) when the built-in models lack the desired degree of realism and/or accuracy, and (iv) availability of the option to use unstructured mesh which enables the user to perform accurate simulations involving complex geometries.

UDFs allow great deal of flexibility in solving a wide range of phenomena. UDFs are basically C/C++ routines programmed by the user and linked dynamically with the ANSYS FLUENT flow solver to augment standard features of the code. These UDFs are compiled and linked during problem set up. They are then invoked by the solver during the solution process. UDFs allow to access ANSYS FLUENT solver data and perform tasks like specifying source terms and special boundary conditions. UDFs have been extensively employed to incorporate various aspects of the GTA welding phenomena that are not built into the flow solver. Through these UDFs, calculations were performed for the movement of the arc on the plate surface, arc heat flux and current density distribution on the welding surface, appropriate boundary conditions on the various workpiece surfaces, solution of Maxwell's equation, Lorentz force calculations, and surface tension gradient induced flow, etc.

ANSYS Mechanical is used in the present study for the structural analysis of the welded joint. Based on the Finite Element (FE) method, ANSYS Mechanical offers a comprehensive solution for structural linear or non-linear and dynamics analysis. It provides a complete set of elements behavior, material models and equation solvers for a wide range of engineering problems. In addition, ANSYS Mechanical offers thermal analysis and coupled-physics capabilities involving acoustic, piezoelectric, thermal–structural and thermoelectric analysis. In the present study, the welded structure undergoes non-linear behavior. A structure is non-linear if the loading causes significant changes in stiffness. Typical reasons for stiffness changes are (i) material non-linearity: strains beyond the elastic limit (plasticity), (ii) geometric non-linearity: large deflections, and (iii) contact non-linearity: changing status (contact between two bodies, element birth/death). ANSYS Mechanical uses a set of linear equations, and hence the non-linear response cannot be predicted directly. However, a non-linear structure can be analyzed using an iterative series of linear approximations, with corrections. Consequently, ANSYS Mechanical uses an iterative process called the Newton-Raphson Method. A simplified explanation of the method is shown in Fig. 4.7. The actual relationship between the load and displacement (shown with a blue dotted line) is not known beforehand. Consequently, a series of linear approximations with corrections is performed (shown with solid red lines).

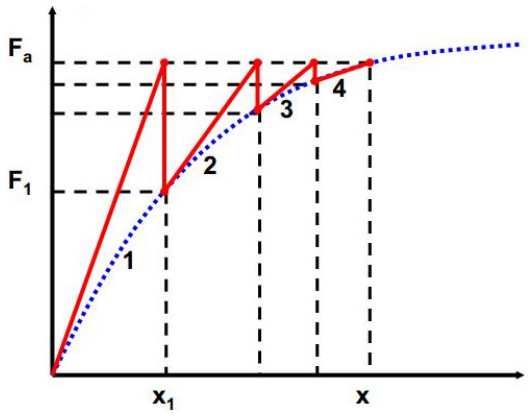


Figure 4.7: A full Newton-Raphson iterative analysis for one increment of load (4 iter. shown).

### 4.3.2 Simulation Set up

The geometrical dimensions of one of the two identical thin stainless steel plates being welded with a butt joint are 100x25x5mm. The geometry was created in the ANSYS Design Modeler and imported into ANSYS Meshing, where a structured mesh was created. The meshed three-dimensional geometry, representing the symmetric half (Fig. 4.8), comprised of 0.4 million hexahedral cells. Since the problem is symmetric about the weld centerline, the symmetry boundary condition has been employed while developing the computational domain. In order to accurately capture the weld pool dynamics, the mesh nodes were clustered in the vicinity of the welding path. Coarser mesh is chosen for the areas far from the weld bead in order to reduce computation. The FE solver, ANSYS Mechanical allows the node-to-node mapping (when the meshes in both the solvers are identical) of thermal data from the ANSYS FLUENT flow solver as thermal loads in the FE solver, and/or interpolation of thermal data when the meshes used in the two solvers are different. The ANSYS Workbench platform is used to run all the aforementioned software for seamless transfer of solution data.

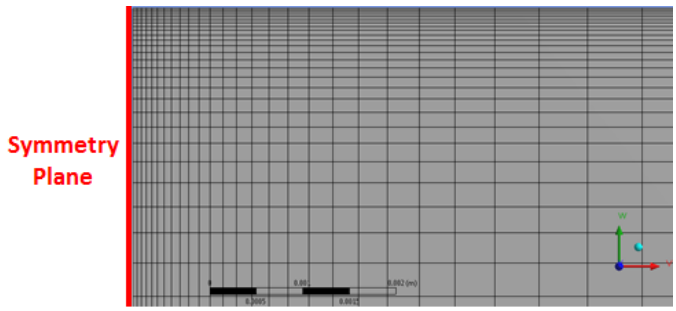


Figure 4.8: A zoomed-in segment of the mesh near the weld line.

First, the transient weld pool dynamics and thermal analysis problem is solved in a coupled manner in the ANSYS FLUENT flow solver. This generates the temperature history at all nodes. This temperature history is exported at every time step of the solution procedure to the FE structural analysis solver ANSYS Mechanical. Here, a structural (thermal stress) analysis is performed. The FE solver outputs the workpiece deformation and stress distributions. Hence, intermediary steps of the simulation give the thermal stress evolution in the plates undergoing welding. As the welding process is completed, and the welded plated cool down to their initial state, the thermally-induced residual stress distribution is obtained. A flow diagram of the major steps in the simulation is shown in Fig. 4.9.

For the present simulations, we have considered thin plates of austenitic stainless steel (SUS304). The temperature dependent thermodynamic and transport properties [142] are highlighted in Fig. 4.10(a)-(d). Material modeling is done utilizing the variation of mechanical properties with temperature [143], as shown in Fig, 4.11. The solidus and liquidus temperatures of steel are 1523K and 1723K, respectively, and the latent heat of fusion is $2.47 \times 10^5$ J/kg [72]. The welding voltage was at 12.5V. An arc efficiency of 0.7 is employed [44]. It is assumed that the plates are initially at $T_{init} = 27^{o}C$. The standard SIMPLE algorithm was used for the pressure-velocity coupling and a second-order interpolation scheme was employed in all the equations of the CFD model. An integration time step of 0.01s was used for the simulations. The bilinear isotropic hardening model was employed in the FE solver. A schematic representation of the isotropic hardening rule is shown in Fig. 4.12. The temperature variation of the strain-hardening coefficient is also included in the FE model [143].

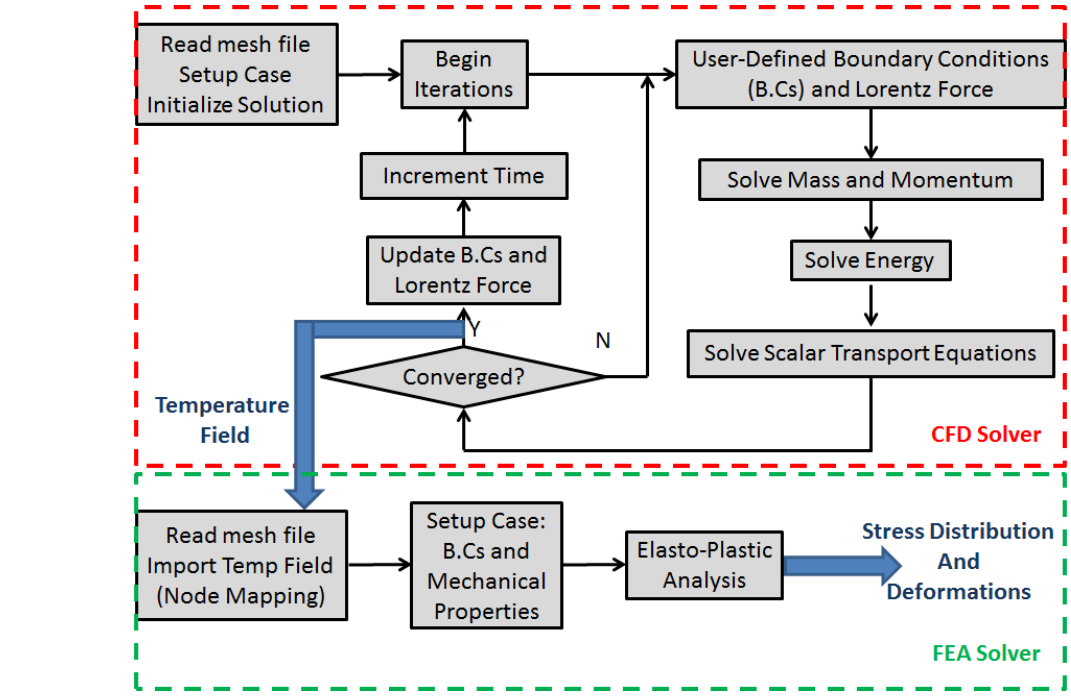


Figure 4.9: Flow diagram of the main solution steps.

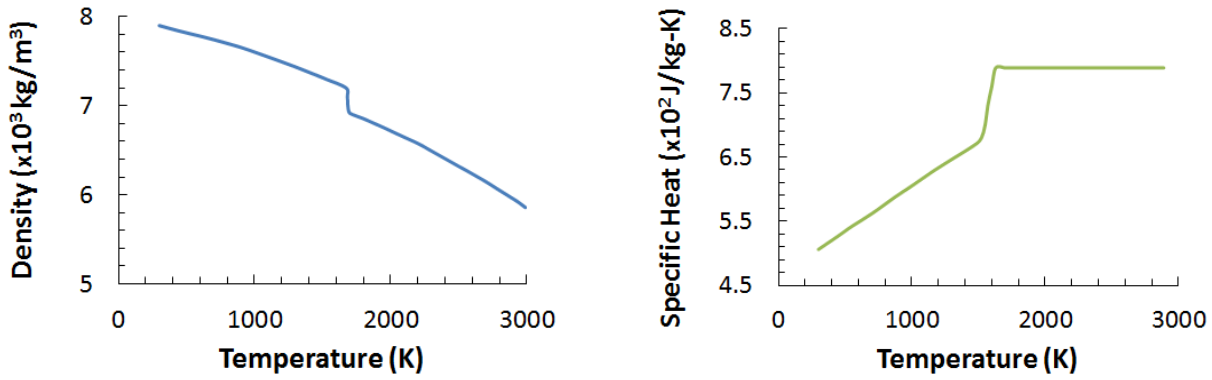


(a) (b)

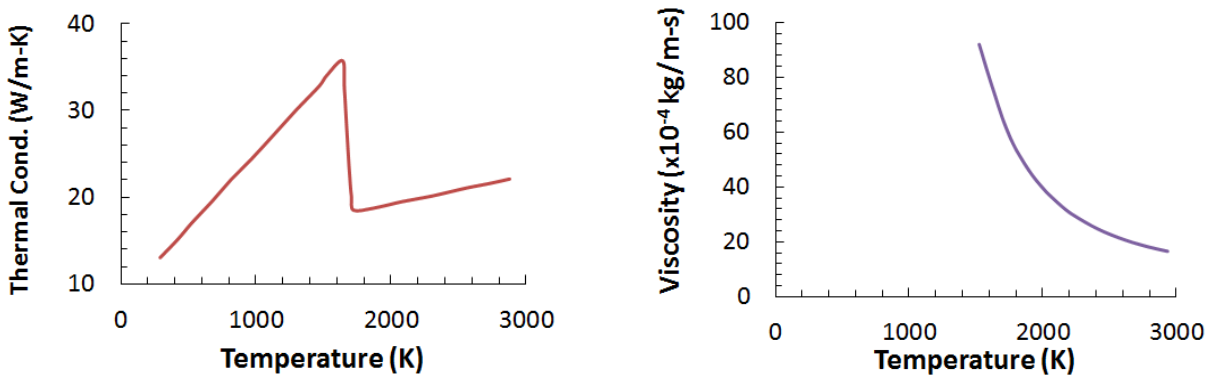


(c) (d)

Figure 4.10: Variations of thermophysical properties with temperature.

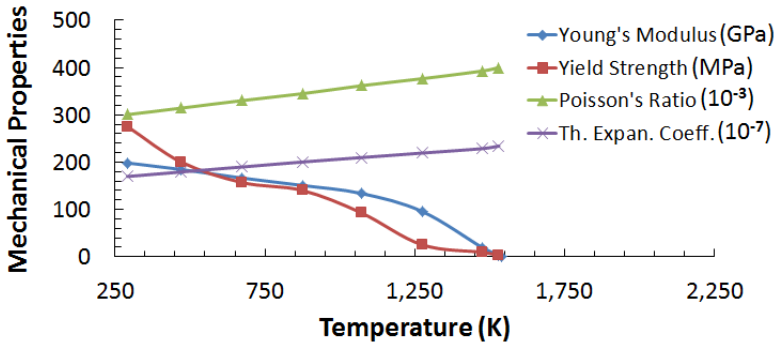


Figure 4.11: Variation of mechanical properties with temperature.

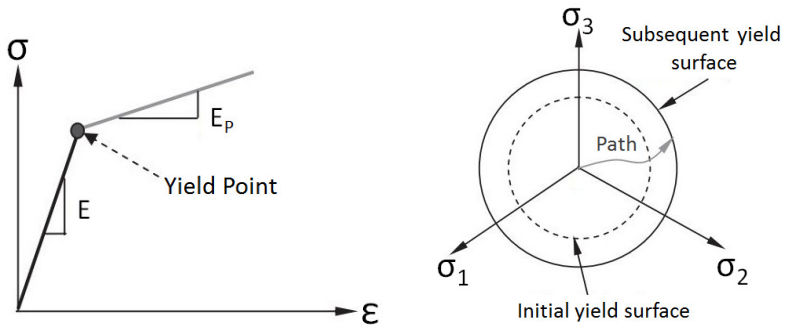


(a) (b)

Figure 4.12: Schematic representation of (a) Bilinear strain-stress relationship, and (b) Isotropic hardening rule.

# Chapter 5

# Results and Discussion

## 5.1 Model Validation

To verify the validity of the weld pool dynamics model, the results of the numerical simulations are compared with available experimental and previous simulation data. Figure 5.1 shows the anodic workpiece top surface heat flux distribution used in the present study compared with experimental results obtained by Nestor [145]. The anode heat flus distribution is also compared with numerical simulation estimates made by Dong et al. [144]. Dong et al. had obtained the anode heat flux distribution by coupling the welding arc and weld pool model in their simulations. The results highlighted are for welding parameters of 200A welding current and 6.3mm arc length. It is evident that the heat flux distribution modeled in the present investigation, using Eq. (4.19), agrees well with both previous experimental and simulation results.

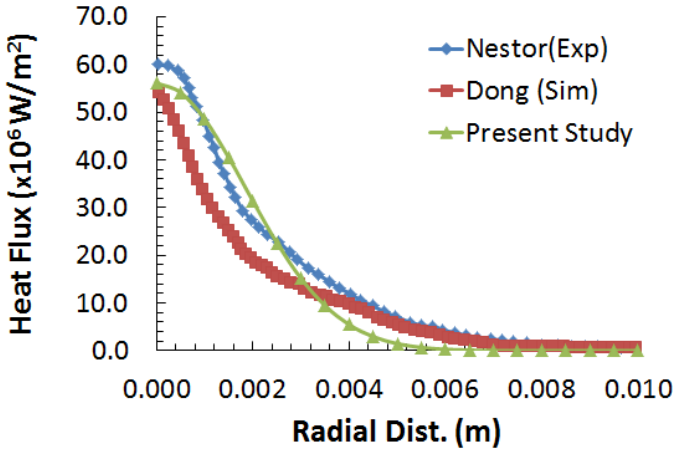


Figure 5.1: Comparison between previous experimental and simulation data of anodic workpiece top surface heat flux distribution with present study.

Figure 5.2 shows the anodic workpiece top surface current density distribution used in the present study compared with experimental results obtained by Nestor [146]. The current density distribution is also compared with numerical simulation estimates made by Dong et al. [144]. The results highlighted are for welding parameters of 200A welding current and 6.3mm arc length. It is evident that the heat flux distribution modeled in the present investigation, using Eq. (4.20), agrees well with both previous experimental and simulation results. These give us confidence in the proper incorporation of the welding arc effects on the workpiece.

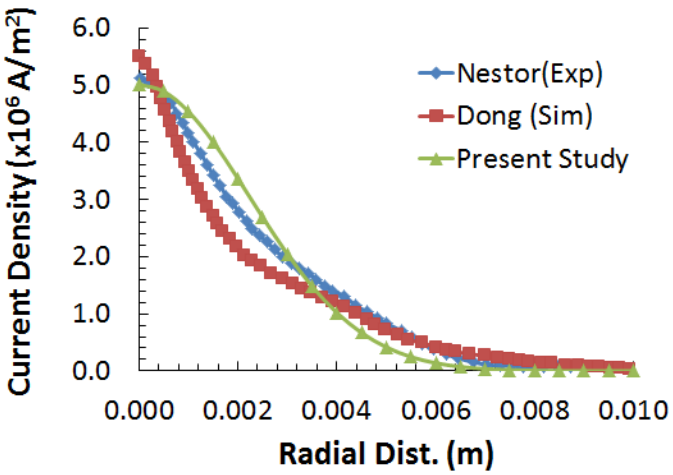


Figure 5.2: Comparison between previous experimental and simulation data of anodic workpiece top surface current density distribution with present study.

The variation of the plasma induced shear on the weld pool surface with current is shown in Fig. 5.3. Validation with previous simulation data is also highlighted in the same figure for a current of 200A. They agree well. It can be seen that the gas shear is zero at the arc center, increases abruptly in an almost linear fashion, and then rapidly decreases to zero. The maximum outward plasma induced shear increases with increase in current.

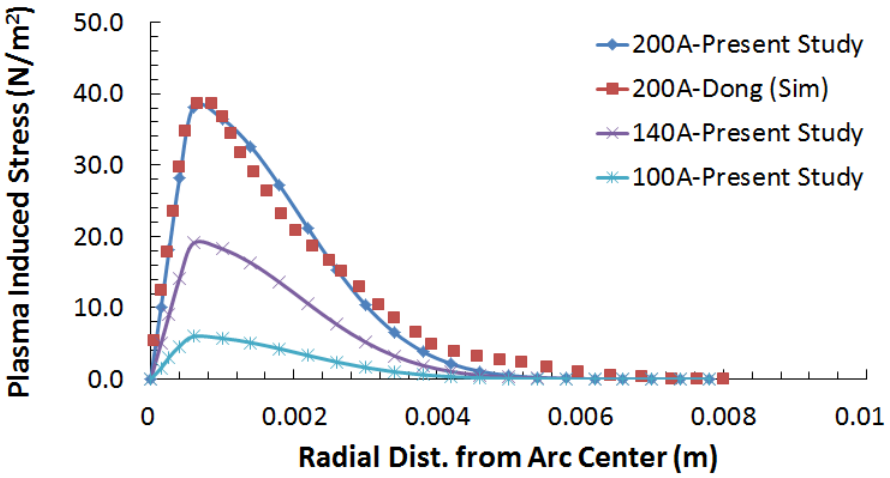


Figure 5.3: Variation of plasma induced shear stress on weld pool surface with current.

Figures 5.4-5.6 show the variation in anodic workpiece top surface heat flux distribution with welding current, arc length and electrode angle that is modeled in the present study. Figure 5.4 is at 3mm arc length and $60^0$ electrode angle. Figure 5.5 is at a welding current 200A and $60^0$ electrode angle. Figure 5.6 is at a current 200A and 3mm arc length. The trends closely follow previous experimental and simulation results [76]. It is seen that increasing the welding current would increase the magnitude of the heat flux and widen the heat distribution of the arc on the weld pool surface. However, the heat distribution width weakly increases compared to the magnitude of the heat flux. This leads to larger temperature gradient on the pool surface with increasing welding current. According to Eq. (4.17) and (4.18), the values of the surface tension gradient and temperature gradient on the pool surface determine the strength of the Marangoni convection. Hence, increasing current should strengthen the Marangoni convection on the pool surface. Also, the outward plasma drag force would increase with high welding current. Increasing current also weakly increases the electromagnetic (Lorentz) force and buoyancy. In case of arc length or electrode gap decrease, it is seen that increase in magnitude of the heat flux and width of the heat distribution is comparable. Therefore, the temperature gradient on the pool surface decreases with increase in arc length. This weakens the Marangoni convection on the pool surface. Increasing the arc length also increases the plasma drag force, but the effect is relatively weaker than when current is increased. In case of increase in electrode tip angle, the heat flux on the weld pool surface increases, i.e. the blunter the tip becomes, the arc constriction

increases, resulting in higher heat flux. However, the increase is very small. Also, it is noted that the heat distribution of the arc has no change with increase in electrode tip angle. Hence, effect on the weld pool driving forces in negligible. Figure 5.7 highlights the definition of electrode tip angle.

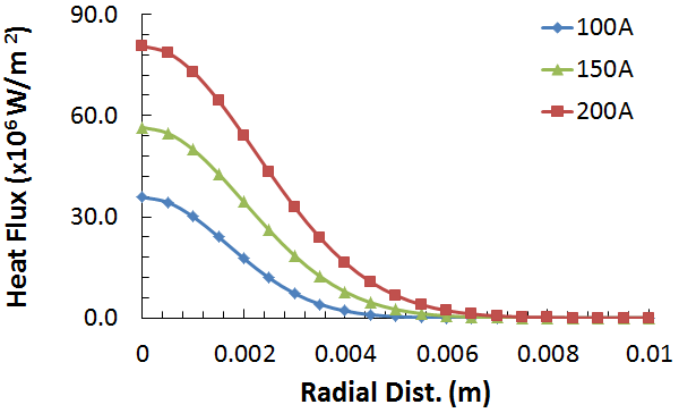


Figure 5.4: Heat flux distribution variation with current, under 3mm arc length and 60 degree electrode angle.

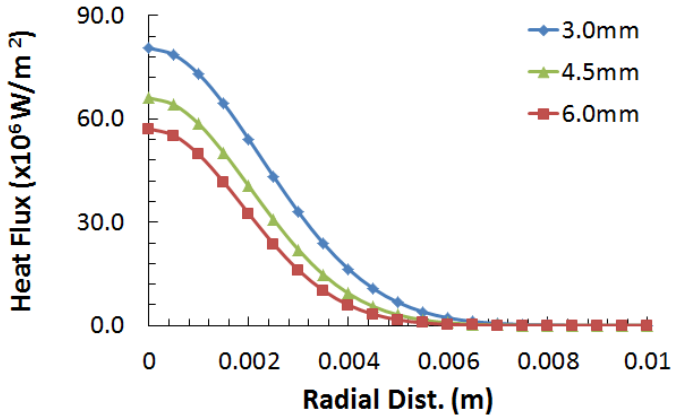


Figure 5.5: Heat flux distribution variation with arc length, under 200A welding current and 60 degree electrode angle.

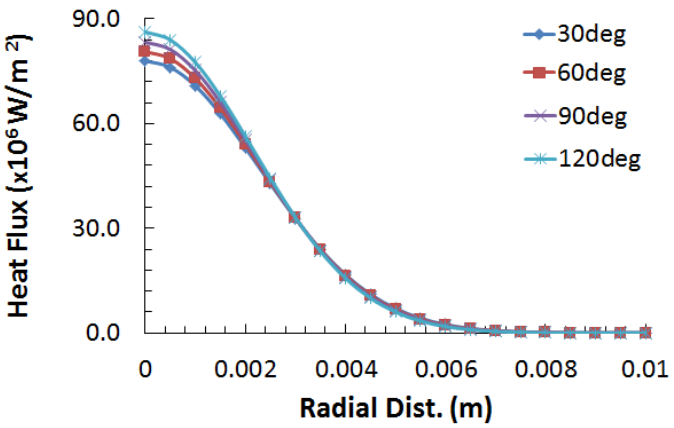


Figure 5.6: Heat flux distribution variation with electrode tip angle, under 200A welding current and 3mm arc length.

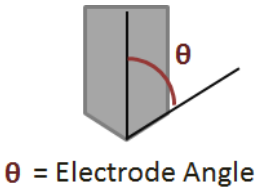


Figure 5.7: Electrode tip angle definition.

It can be noted that welding current has the most significant influence on the heat flux distribution, while electrode angle has the least influence. These results validate the proper inclusion of welding current, arc length, and electrode angle variation effects on the heat flux distribution.

The current density distributions also follow similar trends, validating previous published results [76], and are highlighted in Fig. 5.8-5.10. Increasing the current significantly increases the current density and has a significant effect on the electromagnetic (Lorentz) force. Hence, increasing the current strengthens the radially inward flow under DCEN configuration. This would result in a deeper and narrower weld, thus increasing the D/W ratio. Decreasing the arc length or electrode gap results in increased current density. This would result in higher D/W ratio due to strengthening of the Lorentz force. However, this effect is relatively weaker compared to

when the welding current is increased. Increasing the electrode tip angle effectively results in greater constriction of the arc. However, this has negligible or no effect on the current density distribution. Hence, change in the electrode tip angle has almost negligible effect on D/W ratio. These variation patterns validate the proper inclusion of the welding current, arc length, and electrode angle effects on the current density distribution.

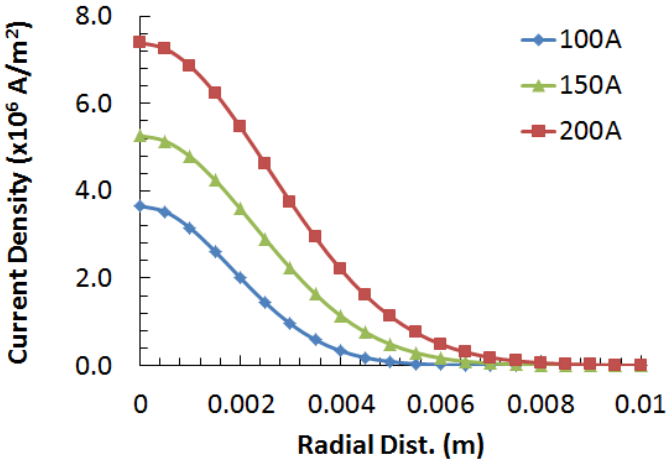


Figure 5.8: Current density distribution variation with current, under 3mm arc length and 60 degree electrode angle.

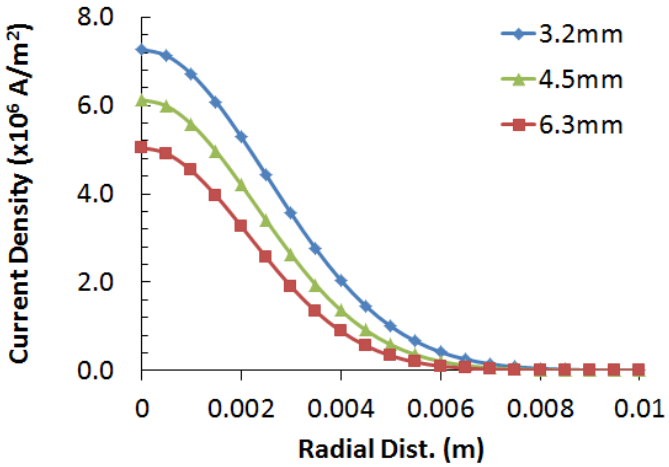


Figure 5.9: Current density distribution variation with arc length, under 200A welding current and 60 degree electrode angle.

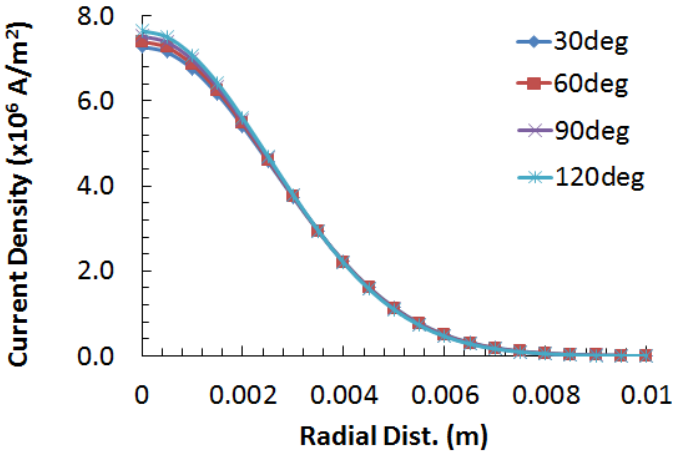


Figure 5.10: Current density distribution variation with electrode tip angle, under 200A welding current and 3mm arc length.

The present model's ability to predict the weld shape is verified with available experimental data. Figure 5.11 shows the predicted weld shape, compared with experimental [144] results. The welding was done at 2mm/s with a welding current of 160A, arc length of 3mm, and oxygen content of 175ppm. Both the weld shape and size of the weld show good agreement between the experiment and the present simulation.

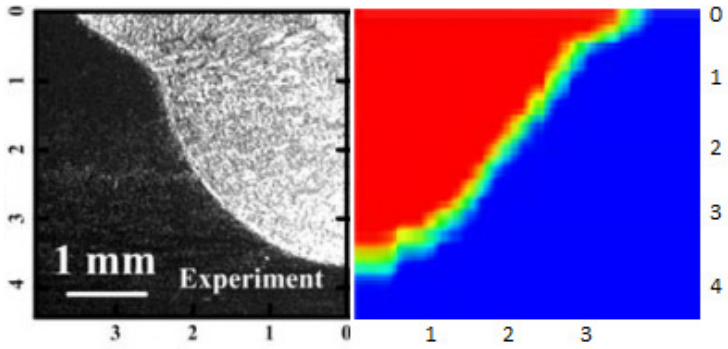


Figure 5.11: Comparison between experimental [144] and calculated weld shape prediction, using temperature-dependent thermophysical properties.

The calculated velocity vectors and temperature fields for the weld containing 175ppm of sulphur are presented in Fig. 5.12. The welding parameters are: 2.5mm/s welding speed, 150A welding current, and 3mm arc length. The plots are on the xy-plane and positioned on the z-axis where the arc is located at that instant in time. The maximum temperature reached is 2120K. This is below the critical temperature of ~2340K for 175ppm of sulphur content (refer Fig. 4.2). Hence, the surface tension gradient remains positive on the entire weld pool surface. The surface tension at the center of the weld pool is more than the surface tension towards the periphery. This results in a radially inwards surface flow that sets up a convective motion in the weld pool. This convective flow results in a deep and narrow weld, by carrying heat from the peripheral region towards the central region. It is evident that convective flow in the weld pool significantly alters the weld pool D/W ratio and the thermal energy distribution in the welded joint. The HAZ of the welded joint is thus affected by weld pool dynamics. It can thus be rightly concluded that inclusion of the weld pool dynamics into the thermally-induced stress analysis is necessary as it generates a more accurate thermal profile in the welded joint.

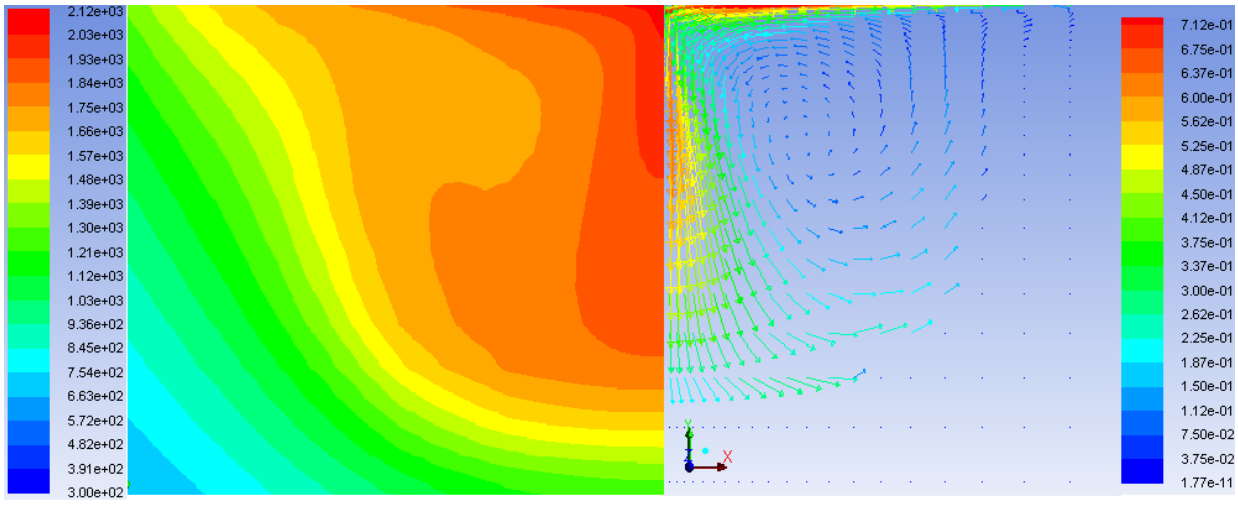


Figure 5.12: Temperature (in K) and velocity vectors (in m/s) at welding current of 150A, 3mm arc length, and 2.5mm/s welding speed. Calculation performed with temperature-dependent thermophysical properties.

## 5.2 Weld D/W Prediction

### 5.2.1 Using Temperature Dependent Thermophysical Properties

The welding current has been determined as the most important parameter influencing the weld shape and weld D/W ratio in GTA welding. The other significant parameters affecting the weld shape and weld D/W ratio are the welding speed and arc length or electrode gap. Controlled parametric simulation studies are done to delineate the influence on the weld D/W ratio. For each of these parameters, the simulations were run with low (≤40ppm) and high (≥150ppm) oxygen content. The simulations validate that under low surface active agent content the weld shapes are wide and shallow. Relatively deeper and narrower welds are obtained under high surface active agent content. The discussion here focuses mainly on the Marangoni convection and plasma induced shear stress and their significance and relative strength in determining the final weld shape and D/W ratio. In the operating regime that has been modeled here, both electromagnetic (Lorentz) force and buoyancy force undergo smaller changes in their strength when the welding parameters are varied. Hence, during the parametric study, these affect the weld shape and weld D/W ratio to a much lesser extent.

Figure 5.13 represents the D/W ratio variation with current at 30ppm of oxygen. The weld D/W ratio initially slightly increases, and then decreases gradually to a more steady value of ~0.16. The results obtained from the present study agree well with experimental data [145]. The behavior at 150ppm of oxygen is highlighted in Fig. 5.14. In this case, the weld D/W ratio initially increases steadily, and then maintains a constant value of ~0.45. Referring to Fig. 5.4, it is seen that increasing the welding current would increase the magnitude of the heat flux and widen the heat distribution of the arc on the weld pool surface. However, the heat distribution width weakly increases compared to the magnitude of the heat flux. This leads to a larger temperature gradient on the pool surface with increasing welding current. According to Eq. (4.17) and (4.18), the values of the surface tension gradient and temperature gradient on the pool surface determine the strength of the Marangoni convection. Hence, increasing current should strengthen the Marangoni convection on the pool surface. Also, the outward plasma drag force near the central weld pool region would directly increase with higher welding current. Since, at 30ppm of oxygen, an outward Marangoni convection occurs, a relatively wide and shallow weld

is obtained. A high welding current would increase the temperature gradient on the molten pool and strengthen the outward Marangoni convection. Also, the outward plasma drag force would increase with increasing welding current. Consequently, the width of the weld increases. Hence, the overall effect is that the weld D/W ratio decreases with increasing welding current. However, at 150ppm of oxygen, an inward Marangoni convection occurs, resulting in a deeper and narrower weld. Hence, there exist two counter re-circulatory flows. The outward flow due to the plasma drag force is near the center of the weld pool. The inward flow due to Marangoni convection exists in the outer region of the weld pool. When the welding current is relatively low, the outward plasma drag force is weak, and the inward Marangoni convection dominates the fluid flow pattern on the weld pool surface. Hence, the weld D/W ratio initially increases with the welding current. When the welding current is greater than 160A, the plasma drag force starts to dominate and the outward convection at the center of the weld pool is strengthened, which weakens the inward Marangoni convection at the edge of the weld pool. Consequently, the weld D/W ratio remains constant at ~0.45 when the welding current is over 160A.

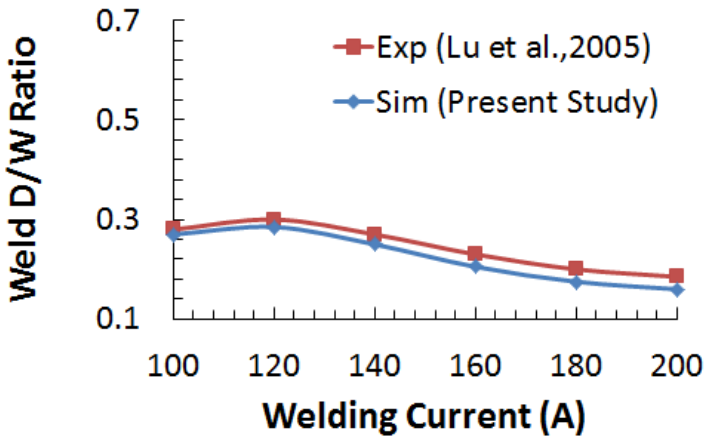


Figure 5.13: Effect of Current on Weld D/W Ratio with 30ppm of oxygen under 2mm/s welding speed, and 3mm arc length.

The percent error in the weld D/W prediction from the present model when compared with experimental data [145] is shown in Fig. 5.15. We find that the model better predicts the weld

D/W ratio under high surface active agent content. The error is ≤5%. However, under low surface active agent content, the error stays ≤10% till 160A welding current. Beyond which the error in weld D/W ratio prediction is ≤15%. One possible explanation is that the present model approximates the heat flux distribution on the weld pool surface from the arc. Hence, under high welding current, the error in this approximation becomes pronounced and it influences the weld D/W prediction.

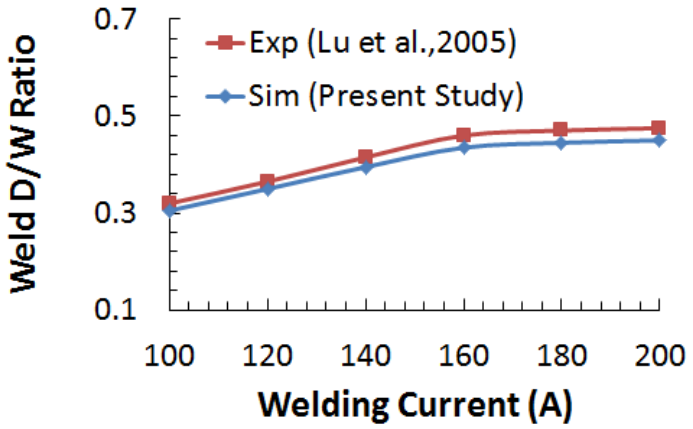


Figure 5.14: Effect of Current on Weld D/W Ratio with 150ppm of oxygen under 2mm/s welding speed, and 3mm arc length.

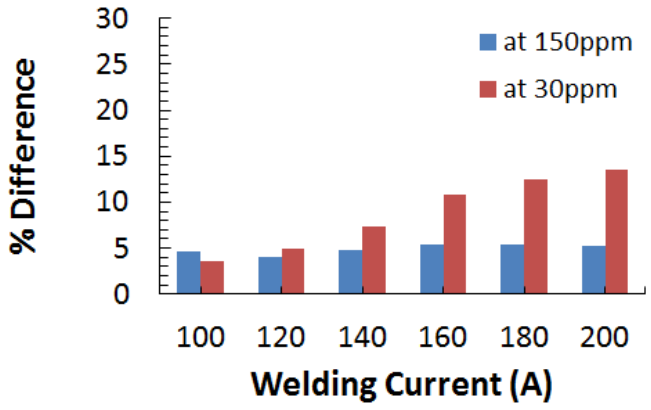


Figure 5.15: Percent error when compared with experimental results.

The effect of welding speed on the weld D/W ratio is much simpler to analyze than the welding current and arc length influence because the welding speed does not affect the shape of the heat distribution to the weld. Welding speed affects the net heat input per unit length of the weld and influences the peak temperature and the temperature gradient on the pool surface. With increasing welding speed, the peak temperature in the weld pool surface decreases. Also, at lower welding speed, the average temperature gradient on the pool surface is larger than that at high welding speed. A lower temperature gradient weakens the strength of the Marangoni convection on the pool surface. It is noted that the outward plasma drag in not influenced by the change in welding speed and its influence remains the same. Also, the electromagnetic (Lorentz) force is not affected by the changing welding speed. The weaker buoyancy force is affected to a small extent by changing the welding speed, but its influence is negligible in the determination of the final weld D/W ratio. Figure 5.16 shows that the weld D/W ratio almost remains the same with increasing welding speed, and can be considered insensitive to welding speed at low ppm (≤40ppm).

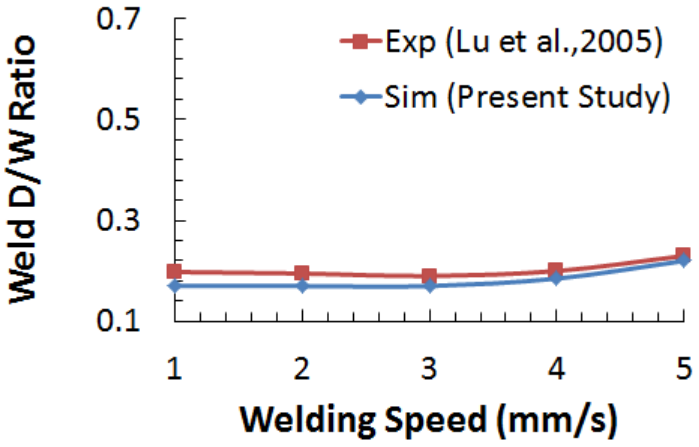


Figure 5.16: Effect of Welding Speed on Weld D/W Ratio with 30ppm of oxygen under 160A current, and 3mm arc length.

However, under high oxygen content (150ppm), the weld D/W ratio decreases with increasing welding speed, as shown in Fig. 5.17. In this case where the inward Marangoni convection occurs under high oxygen content, with increase in welding speed the average temperature gradient on the weld pool surface decreases, thereby weakening the inward Marangoni convection. The inward Marangoni convection is responsible for higher D/W ratio. Hence, with increasing welding speed the weld D/W ratio decreases. On the contrary, under low oxygen content, the weak outward Marangoni convection produces a decreasing weld width with increasing welding speed. This impedes the decrease in the surface temperature gradient and therefore the weld D/W ratio very weakly changes and hovers around ~0.18 to ~0.2. The results obtained from the present study agree well with experimental data [145].

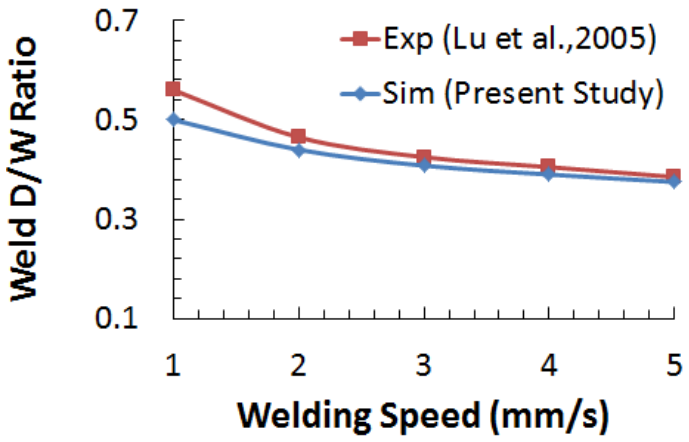


Figure 5.17: Effect of Welding Speed on Weld D/W Ratio with 150ppm of oxygen under 160A current, and 3mm arc length.

The percent error in the weld D/W prediction from the present model when compared with experimental data [145] is shown in Fig. 5.18. We find that the model better predicts the weld D/W ratio under high surface active agent content. The error is ~10% at very low welding speeds and the error reduces <5% at higher welding speeds. However, under low surface active agent content, the error stays ≤15% at lower welding speeds. At higher welding speeds, the error in weld D/W ratio prediction is ≤10%. One possible explanation is that the present model

approximates the heat flux distribution on the weld pool surface from the arc. Hence, under low welding speeds, the amount of heat input per unit length of the weld is more, and hence the error in this approximation becomes pronounced and it influences the weld D/W prediction. It can be seen that at welding speeds ≥3mm/s, the experimental and simulations results agree very well.

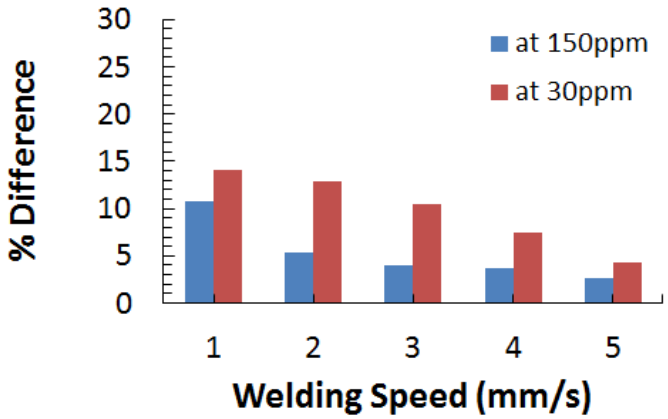


Figure 5.18: Percent error when compared with experimental results.

Referring to Fig. 5.5 and 5.9, it can be seen that decreasing the arc length or electrode gap increases the peak heat and current density fluxes. Figure 5.19 shows the weld D/W ratio variation with arc length under low oxygen content. It can be inferred that the weld D/W ratio is weakly sensitive to the arc length changes. However, the weld D/W ratio slightly decreases with increasing arc length or electrode gap under high oxygen content, as shown in Fig. 5.20. From Fig. 5.5 it is seen that a larger electrode gap broadens the heat distribution of the arc and lowers the heat flux on the weld pool surface. Hence, the temperature gradient on the weld pool surface would decrease when the electrode gap is increased. This would in turn weaken the Marangoni convection on the weld pool surface. Under low oxygen content, with increasing arc length or electrode gap, the weakened outward Marangoni convection produces a decreasing weld width. This impedes the decrease in the surface temperature gradient and therefore the weld D/W ratio very weakly changes and hovers around ~0.24 to ~0.28. However, under high oxygen content, the inward Marangoni convection is weakened with increasing electrode gap and the weld D/W

ratio decreases. The results obtained from the present study agree well with experimental data [145].

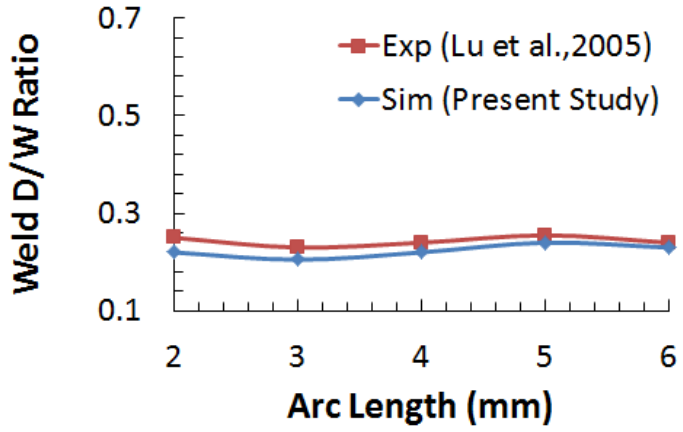


Figure 5.19: Effect of Arc Length on Weld D/W Ratio with 30ppm of oxygen under 160A current, and 2mm/s welding speed.

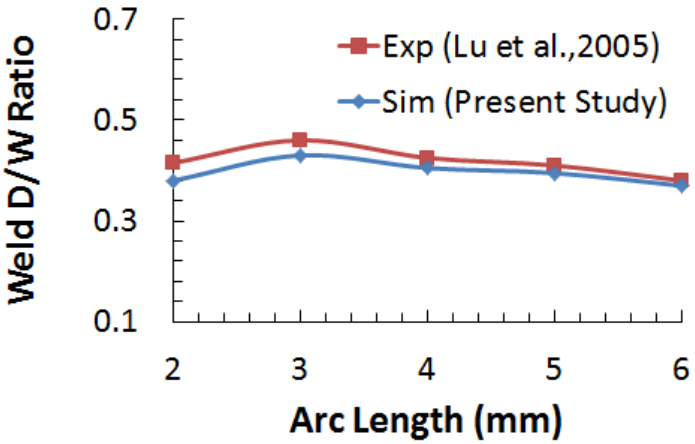


Figure 5.20: Effect of Arc Length on Weld D/W Ratio with 150ppm of oxygen under 160A current, and 2mm/s welding speed.

The percent error in the weld D/W prediction from the present model when compared with experimental data [145] is shown in Fig. 5.21. We find that the model better predicts the weld D/W ratio under high surface active agent content. The error is ≤10% at smaller electrode gaps and the error reduces <5% at larger electrode gaps. However, under low surface active agent content, the error stays ≤12% at smaller electrode gaps. At larger electrode gaps, the error in weld D/W ratio prediction is ≤8%. One possible explanation is that the present model approximates the heat flux distribution on the weld pool surface from the arc. Hence, under smaller electrode gaps, the amount of heat input per unit length of the weld is more, and hence the error in this approximation becomes pronounced and it influences the weld D/W prediction. At electrode gaps ≥4mm, the experimental and simulations results agree very well.

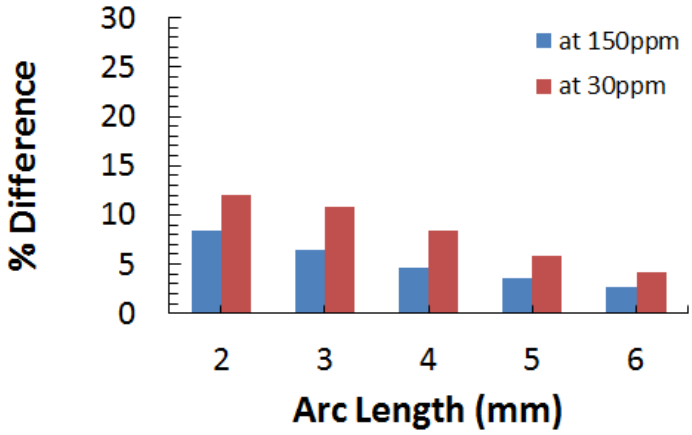


Figure 5.21: Percent error when compared with experimental results.

Figure 5.22 show the variation in the weld D/W ratio with electrode tip angle. The weld D/W ratio very weakly increases with increase in electrode tip angle. As the electrode tip angle increases, the electrode becomes blunter and greater arc constriction is achieved. With increase in arc constriction the peak value in the heat flux distribution increases. However, the distribution width remains the same, as shown in Fig. 5.6. Changing the electrode tip angle has negligible effect on the current density distribution, as shown in Fig. 5.10. Hence, when the

electrode gap is altered, the peak heat flux value increases. Increasing the electrode tip angle from 30$^{o}$ to 120$^{o}$ increases the weld D/W ratio from 0.42 to 0.5. This is a small increase in D/W ratio for a 90$^{o}$ electrode tip angle increase. The weld D/W variation trend obtained from the present study is validated qualitatively with the results highlighted by Kou [44]. They agree well.

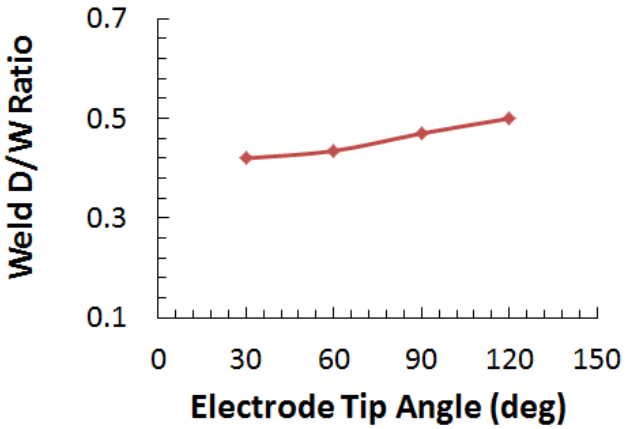


Figure 5.22: Effect of Electrode Angle on Weld D/W Ratio with 150ppm of oxygen under 160A current, 3mm arc length, and 2mm/s welding speed.

Figure 5.23 shows the weld D/W ratio variation with surface active agent content. The oxygen content is increased from 15ppm to 175ppm. It can be seen that decreasing the oxygen content below 40ppm has no effect on the weld D/W ratio. Similarly, increasing the oxygen content beyond 150ppm has no effect on the weld D/W ratio. Below 40ppm of oxygen, the surface tension gradient in the entire weld pool surface remains negative, and a radially outward flow on the weld pool surface prevails. This results in a wide and shallow weld, i.e. a low weld D/W ratio (~0.2). Beyond 150ppm, the central and remaining major portion of the weld pool surface has positive surface tension gradient. This results in a radially inward flow on the weld pool surface. This results in a deep and narrow weld, i.e. a high weld D/W ratio (~0.45). Hence, in order to characterize the weld D/W ratio behavior with various parameters under low and high surface active agent content, choosing any value ≤40ppm and ≥150ppm for low and high content, respectively, would serve the purpose. It can be noted from Fig. 5.23 that between

40ppm and 150ppm the weld D/W ratio increases rapidly with increasing surface active agent content. As the surface active agent content increases, the radially outward flow weakens. The radially inward flow existence starts from the central region weld pool surface. As the surface active agent content is increased, this radially inward flow gains strength and pushes the weakened radially outward flow towards the periphery. Finally, beyond 150ppm of oxygen, only the radially inward flow dominates the weld pool.

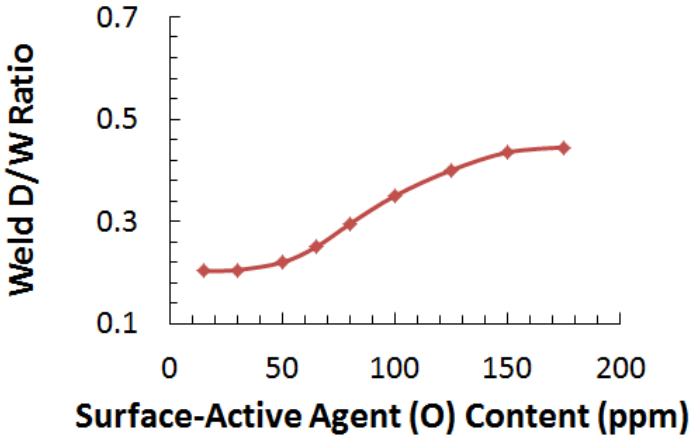


Figure 5.23 Effect of Surface Active Agent (O) Content on Weld D/W Ratio under 160A current, 3mm arc length, and 2mm/s welding speed.

### 5.2.2 Weld Solidification Mode Prediction using CFD Results

The solidification mode can change from planar to cellular and from cellular to dendritic at the pool boundary (refer to Fig. 2.4).While the solidification mode can vary from one weld to another, it can also vary within a single weld from the fusion line to the centerline. Figure 5.24 shows the average temperature gradients at the weld centerline and the fusion line.

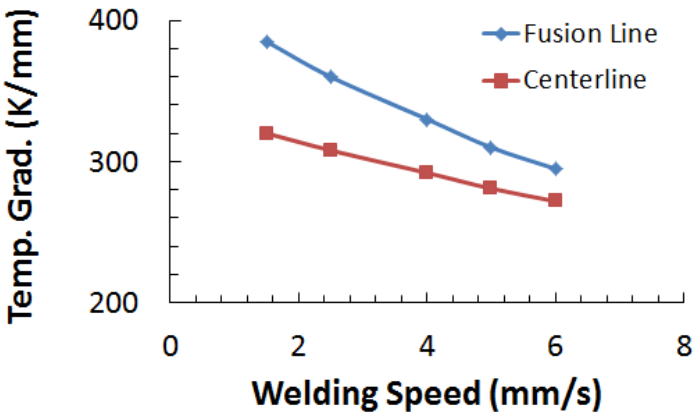


Figure 5.24: Variation of Temperature Gradient at Weld Centerline and Fusion Line against Welding Speed with 100ppm of sulphur under 160A current, and 1mm arc length.

Both $G_{CL}$ and $G_{FL}$ decrease as the welding speed increases. It is to be noted that $G_{FL}$ is higher than $G_{CL}$. It is noted that $G_{FL}$ gets closer to $G_{CL}$ as the welding speed increases. Also, referring to Fig. 2.3 and Eq. (2.3), we know that $R_{CL} >> R_{FL}$. Also, as discussed in Chapter 2, the value of $G/R$ decreases from the fusion line to the weld center. This suggests that the solidification mode may change from planar to cellular, columnar dendritic, and equiaxed dendritic across the fusion zone. Moreover, the value of $G*R$ increases from the fusion line to the centerline. This suggests that the dendritic arm spacing decreases from the fusion line to the centerline because the dendritic arm spacing decreases with increasing cooling rate. Figures 5.25 and 5.26 show the value of $G/R$ and $G*R$ at the weld centerline for different welding speeds. With increase in welding speed, the value of $G*R$ is increased while the value of $G/R$ is reduced at the weld pool centerline. Hence, with increase in welding speed finer substructures would be obtained. Referring to Fig. 2.2, it is known that the solidification mode changes from planar to cellular and dendritic as the ratio $G/R$ decreases. Hence, with increase in welding speed dendritic microstructures may be obtained.

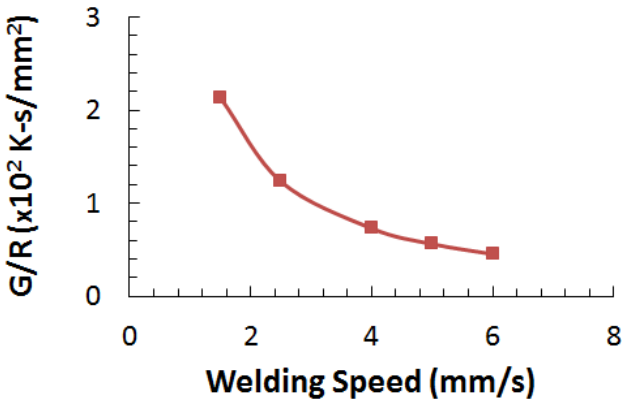


Figure 5.25: Variation of $G/R$ at the weld pool centerline with different welding speeds. $G/R$ represents the solidification mode.

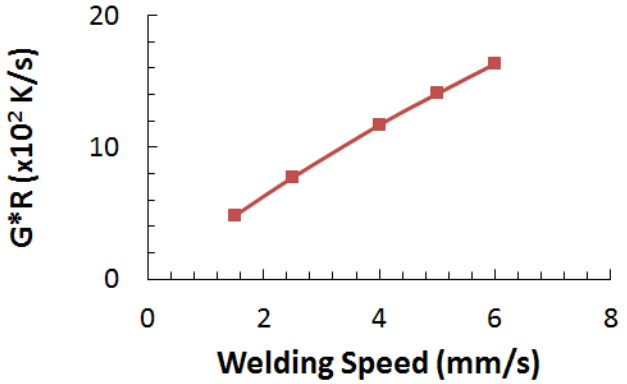


Figure 5.26: Variation of $G*R$ at the weld pool centerline with different welding speeds. $G*R$ represents the solidification rate.

### 5.2.3 Weld D/W Variation with Heat Input per Unit Weld Length

Heat input is a relative measure of the energy transferred per unit length of the weld. It is an important characteristic because, like preheat and inter-pass temperature, it influences the cooling rate, which may affect the mechanical properties and metallurgical structure of the weld and the HAZ. The heat input per unit length of the weld is represented as follows

$$H=\frac{\eta VI}{v} \tag{5.1}$$

where, $\eta$ is the arc efficiency, $H$ is the heat input per unit length of weld (in J/mm), $V$ is the voltage (in V), $I$ is the welding current (in A), and $v$ is the welding speed (in mm/s). Equation (5.1) is useful for comparing different welding procedures for a given welding process. Heat input per unit length of the weld cannot be measured directly. It is calculated from measured values of voltage, welding current and welding speed. Moreover, the weld size is related to heat input. Specifically, the cross-sectional area of the weld is generally proportional to the amount of heat input. Also, the cooling rate is a function of heat input. As the heat input increases, the rate of cooling decreases for a given base material thickness. The relation between preheat temperature, heat input, and cooling rate is given by the following proportionality function

$$R \propto \frac{1}{T_0 H} \tag{5.2}$$

where, $R$ is the cooling rate (in K/s) and $T_0$ is the preheat temperature (K). The cooling rate is a primary factor determining the final metallurgical structure of the weld and the HAZ. Figure 5.27 represents the weld D/W variation with heat input per unit weld length. It should be noted that the heat input is varied changing the welding current; the welding speed is kept constant. The weld D/W ratio variation for both low and high oxygen content is highlighted. In case of high oxygen content, it is seen that with increasing heat input the weld D/W ratio increases steadily and then levels off. Beyond 750J/mm the weld D/W ratio remains constant at ~0.45. Hence, increasing the heat input beyond this value would only increase the HAZ with no desired increase in weld D/W ratio. In case of low oxygen content, it can be seen that with increasing the heat input the weld D/W ratio decreases. The rate of decrease of weld D/W ratio lowers from 750J/mm onwards. The maximum weld D/W ratio is obtained around 500-550J/mm.

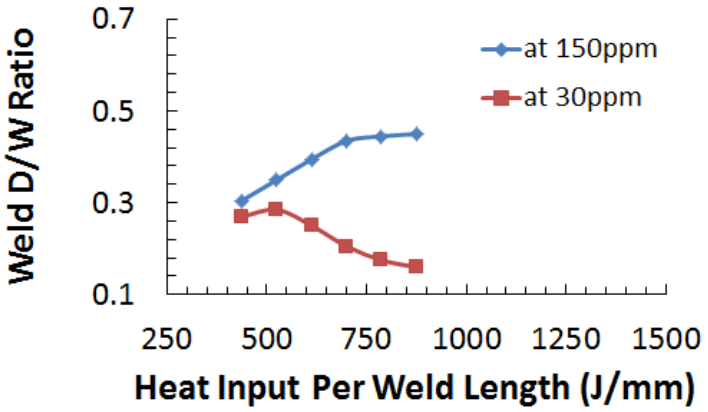


Figure 5.27: Effect of Heat Input per Unit Weld Length on Weld D/W Ratio under 3mm arc length and 2mm/s welding speed. Heat Input per Unit Weld Length varied by changing the Welding Current.

Figure 5.28 represents the weld D/W variation with heat input per unit weld length. It should be noted that the heat input is varied by changing the welding speed; the welding current is kept constant. The weld D/W ratio variation for both low and high oxygen content is highlighted. In case of high oxygen content, it is seen that with increasing heat input the weld D/W ratio increases steadily. The rate of increase of weld D/W ratio lowers from 750J/mm onwards. Beyond 750J/mm the percent increase in weld D/W ratio is ~14% for ~87% increase in heat input per unit length of weld. Since increasing the heat input results in slower cooling rate and enlarges the HAZ, the benefits of increasing the heat input per unit length beyond 750J/mm is not justified. In case of low oxygen content, it can be seen that with increasing the heat input the weld D/W ratio decreases quickly and then maintains a constant value of ~0.18. The maximum weld D/W ratio is obtained around 250J/mm.

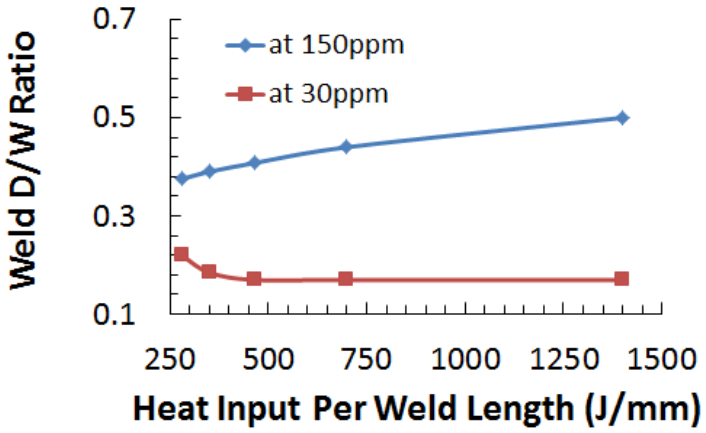


Figure 5.28: Effect of Heat Input per Unit Weld Length on Weld D/W Ratio under 3mm arc length and 160A Welding Current. Heat Input per Unit Weld Length varied by changing the Welding Speed.

An important observation that can be made from Fig. 5.27 and 5.28 is that weld D/W ratio values do not correspond to each other for the same heat input per unit length value. Hence, changing the heat input value by either changing the welding current or welding speed has an influence on how the weld D/W changes. This behavior can be explained considering the various weld pool driving forces and the welding parameters of current and speed. Changing the welding current directly influences the plasma drag force and electromagnetic forces. It has been shown previously that changing the current significantly influences the plasma-induced radially outward flow. Welding current however also determines the heat flux distribution on the weld pool. Hence, it indirectly affects the weld pool surface temperature gradient, i.e. it indirectly affects the Marangoni convection. Welding current also indirectly affects the buoyancy force. On the other hand, changing the welding speed does not influence the plasma drag force and electromagnetic force. Welding speed change affects the temperature gradient on the weld pool surface, and hence influences the Marangoni convection. Changing the welding speed also affects the temperature distribution in the weld pool and hence indirectly influences the buoyancy force. Hence, changing the heat input per unit length of the weld by varying either the current or speed will influence the important weld pool driving forces differently in a non-linear manner. The complex interplay of the driving forces determines the final weld D/W ratio. Hence, when

analyzing weld D/W ratio plots versus heat input, it is important that attention be paid as to how the changes in heat input were achieved.

### 5.2.4 Using Constant Thermophysical Properties

Previous results from other research groups have used constant thermophysical properties in the weld pool dynamics simulations. The present study also did the same to compare the differences in weld D/W ratio predictions from temperature-dependent properties employment. This would help justify the necessity of using temperature-dependent thermophysical properties or whether constant thermophysical properties would suffice. Keeping all other welding parameters and conditions same, the density, specific heat, thermal conductivity, and dynamic viscosity used are shown in Table 1. The present model's ability to predict the weld shape, using constant thermophysical properties, is verified with available experimental data. Figure 5.29 shows the predicted weld shape, compared with experimental [144] results. The welding was done at 2mm/s with a welding current of 160A, arc length of 3mm, and oxygen content of 175ppm. This prediction when referred in conjunction with Fig. 5.11 (where temperature-dependent properties were used), highlights that better agreement in weld shape is obtained using temperature-dependent properties.

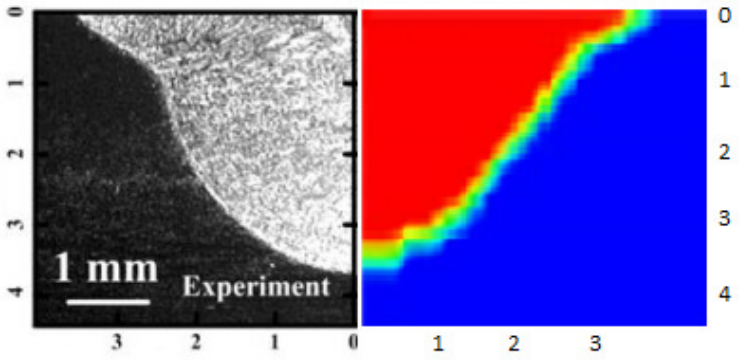


Figure 5.29: Comparison between experimental [144] and calculated weld shape prediction, using constant thermophysical properties.

**Table 1. Thermophysical Properties of Austenitic Stainless Steel SUS304**

| Thermophysical Properties | Unit | Value |
|---|---|---|
| Coefficient of Thermal Expansion | $K^{-1}$ | $10^{-4}$ |
| Density | $Kg/m^3$ | 7200 |
| Viscosity | Kg/m-s | 0.006 |
| Specific Heat | J/kg | 753 |
| Thermal Conductivity | W/m-K | 20 |

Controlled parametric simulation studies are done to delineate the influence on the weld D/W ratio. For each of these parameters, the simulations were run with low (≤40ppm) and high (≥150ppm) oxygen content. Figure 5.30 represents the D/W ratio variation with current at 30ppm of oxygen. The weld D/W ratio initially slightly increases, and then decreases gradually to a more steady value of ~0.14. The results obtained from the present simulation runs follow the experimental trend, but do not agree as well as the predictions made using temperature-dependent thermophysical properties. The behavior at 150ppm of oxygen is highlighted in Fig. 5.31.

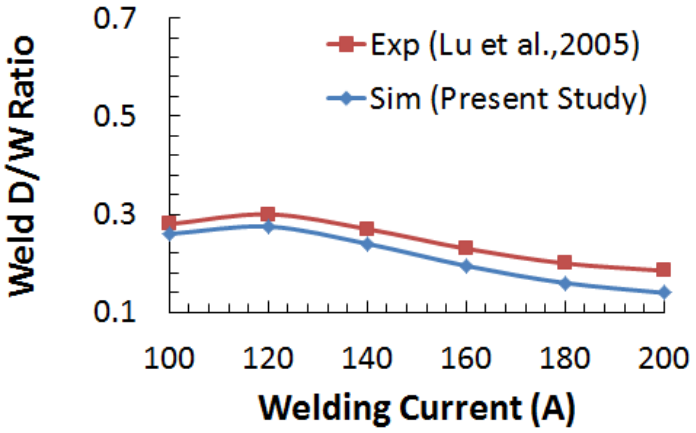


Figure 5.30: Effect of Current on Weld D/W Ratio with 30ppm of oxygen under 2mm/s welding speed, and 3mm arc length.

In this case, the weld D/W ratio initially increases steadily, and then maintains a constant value of ~0.42. As in the case for low oxygen content, the present simulation runs follow the

experimental trend, but do not agree as well as the predictions made using temperature-dependent thermophysical properties. Discussions on the nature of these trends based on various driving force influences are not highlighted here again. The percent error in the weld D/W prediction from the present model when compared with experimental data [145] is shown in Fig. 5.32. We find that the model better predicts the weld D/W ratio under high surface active agent content. The error is ≤10%, compared to ≤5% when using temperature-dependent thermophysical properties. However, under low surface active agent content, the error stays ≤10% till 120A welding current. Beyond which the error in weld D/W ratio prediction is ≤25%.

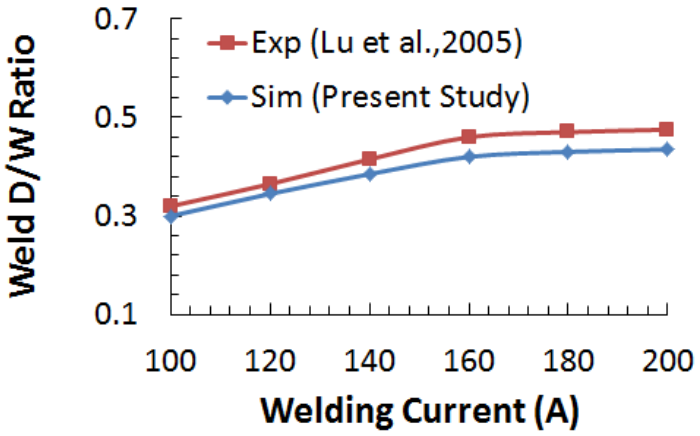


Figure 5.31: Effect of Current on Weld D/W Ratio with 150ppm of oxygen under 2mm/s welding speed, and 3mm arc length.

The effect of welding speed on the weld D/W ratio using constant thermophysical properties is highlighted here. Figure 5.33 shows that the weld D/W ratio follows the trend as obtained from experimental data. However, it does not agree well at lower welding speeds. At higher welding speeds, the agreement is much better.

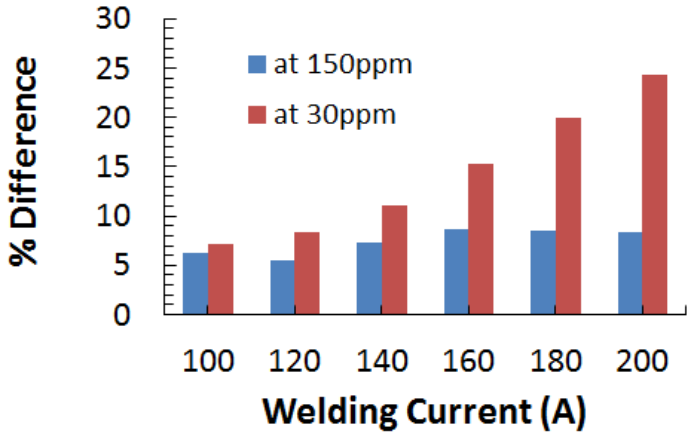


Figure 5.32: Percent error when compared with experimental results.

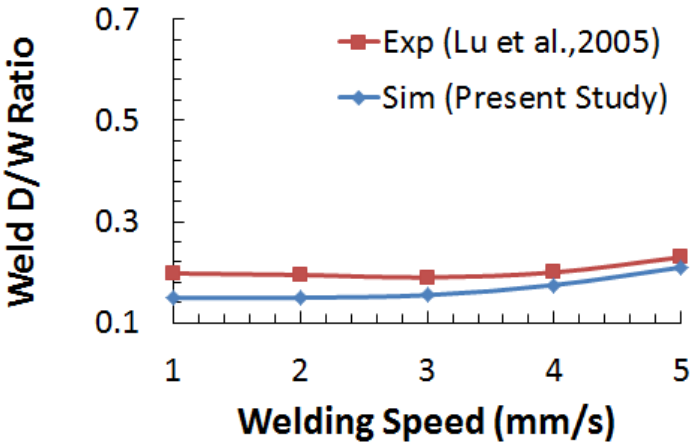


Figure 5.33: Effect of Welding Speed on Weld D/W Ratio with 30ppm of oxygen under 160A current, and 3mm arc length.

Under high oxygen content (150ppm), the weld D/W ratio decreases with increasing welding speed, as shown in Fig. 5.34. The agreement with the experimental data is poor at low speeds. However, the agreement becomes much better beyond 4mm/s.

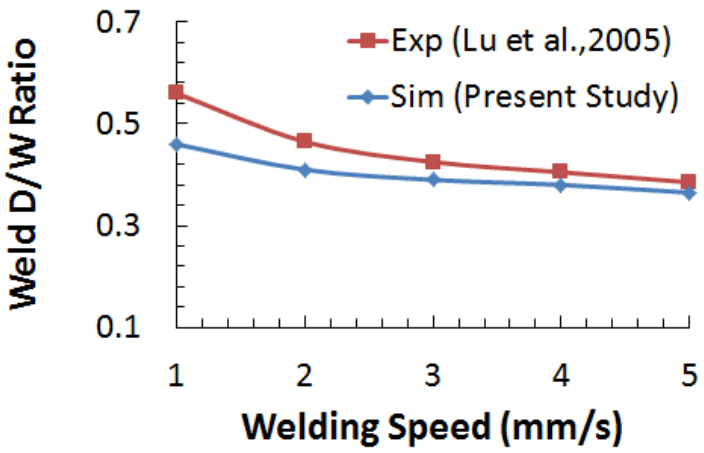


Figure 5.34: Effect of Welding Speed on Weld D/W Ratio with 150ppm of oxygen under 160A current, and 3mm arc length.

The percent error in the weld D/W prediction from the present model when compared with experimental data [145] is shown in Fig. 5.35. Under low oxygen content, the error is close to 25% at very low welding speeds and the error reduces <10% at higher welding speeds. However, under high surface active agent content, the error stays ≤18% at lower welding speeds. At higher welding speeds (≥3mm), the error in weld D/W ratio prediction is ≤10%.

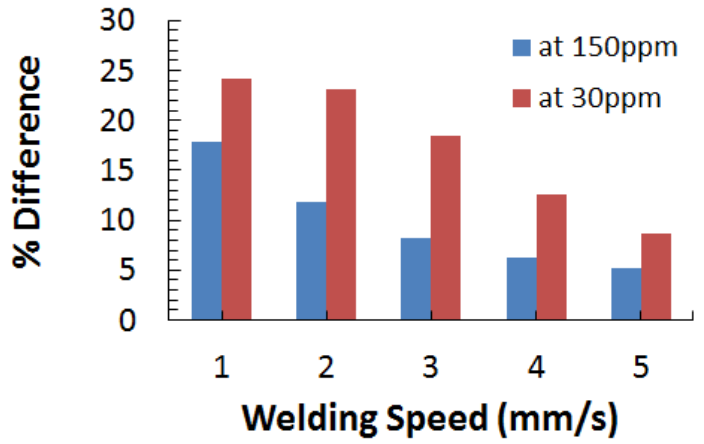


Figure 5.35: Percent error when compared with experimental results.

Referring to Fig. 5.5 and 5.9, it can be seen that decreasing the arc length or electrode gap increases the peak heat and current density fluxes. Figure 5.36 shows the weld D/W ratio variation with arc length under low oxygen content. It can be inferred that the weld D/W ratio is weakly sensitive to the arc length changes. However, the weld D/W ratio decreases with increasing arc length or electrode gap, as shown in Fig. 5.37. The agreement becomes better as the arc length or electrode gap increased. The weld D/W ratio obtained from the present runs does not agree with the experimental results as well as those when temperature-dependent properties were employed.

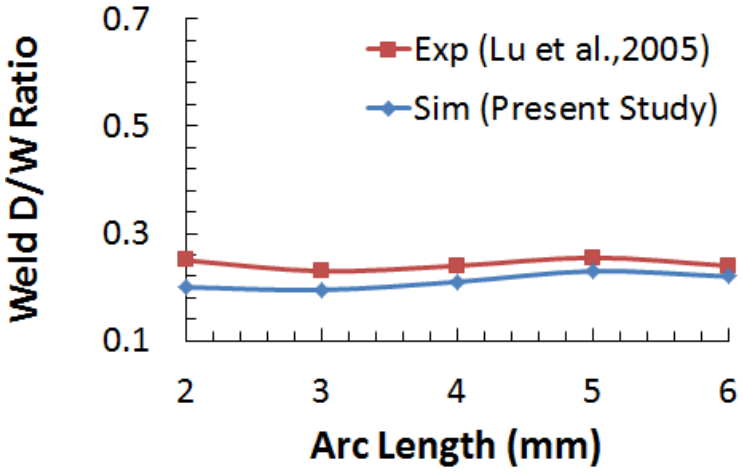


Figure 5.36: Effect of Arc Length on Weld D/W Ratio with 30ppm of oxygen under 160A current, and 2mm/s welding speed.

The percent error in the weld D/W prediction from the present model when compared with experimental data [145] is shown in Fig. 5.38. Under low oxygen content, the error is close to 20% at low arc length and the error reduces <10% at arc lengths ≥5mm. However, under high surface active agent content, the error stays ≤13% at lower arc lengths. At arc lengths ≥3mm, the error in weld D/W ratio prediction is ≤10%.

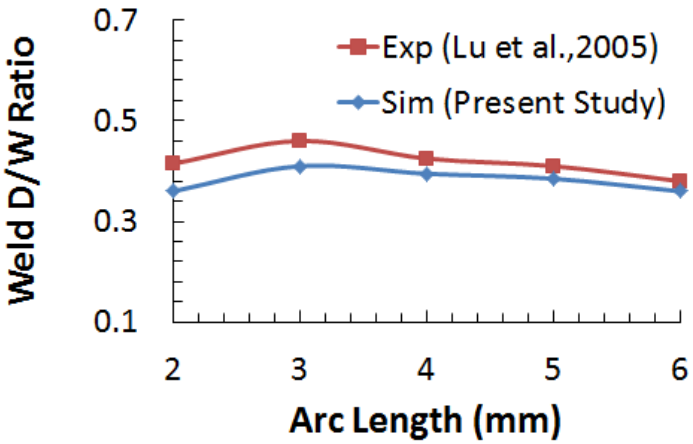


Figure 5.37: Effect of Arc Length on Weld D/W Ratio with 150ppm of oxygen under 160A current, and 2mm/s welding speed.

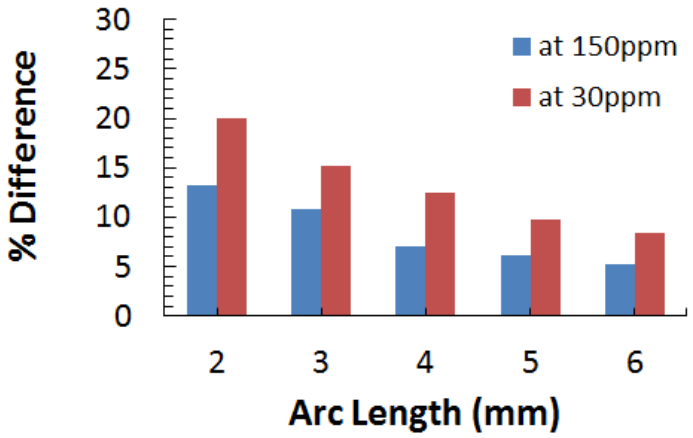


Figure 5.38: Percent error when compared with experimental results.

## 5.3 Mechanical Response of Welded Joint

### 5.3.1 Workpiece Deformation

Three fundamental dimensional changes of a flat welded plate are: (i) transverse shrinkage (shrinkage perpendicular to the weld centerline), (ii) longitudinal shrinkage (shrinkage in the direction of the weld line) and (iii) angular distortion (distortion caused by non-uniform temperature distribution in the through-thickness direction. A welded plate undergoes these

changes to some extent depending on the workpiece clamping (i.e., the constraints employed in the FE solver).

Referring to Fig. 4.6, the effect of various constraint combinations on the workpiece deformation is studied. For all the cases studied, it is to be noted that face ABCD is defined as symmetric, i.e. there is not deformation normal to this face. For the coordinate system, refer to Fig. 4.1. For the first constraint configuration, faces ABB'A' and DCC'D' are fixed, i.e. $\vartheta_x = \vartheta_y = \vartheta_z = 0$. These faces cannot move or deform. Other faces are free to deform. Figures 5.39 to 5.41 highlight the x-, y-, and z-directional deformation of the workpiece. Welding parameters are: welding current 150A, arc length 3mm, welding speed 2.5mm/s, and 100ppm of oxygen. The total deformation of the workpiece is shown in Fig. 5.42. For the second constraint configuration, edges AA', BB', CC', and DD' are fixed, i.e. they cannot move or deform. However, rotation is permitted about the edges, i.e. the plate can bend. Other faces are free to deform. Figures 5.43 to 5.45 highlight the x-, y-, and z-directional deformation of the workpiece. Welding parameters are: welding current 150A, arc length 3mm, welding speed 2.5mm/s, and 100ppm of oxygen. The total deformation of the workpiece is shown in Fig. 5.46. For the third constraint configuration, edges AA' and BB' are fixed. The other end of the workpiece is free to deflect. Other faces are free to deform. This configuration corresponds to welding away from the fixed edge. Figures 5.47 to 5.49 highlight the x-, y-, and z-directional deformation of the workpiece. Welding parameters are: welding current 150A, arc length 3mm, welding speed 2.5mm/s, and 100ppm of oxygen. The total deformation of the workpiece is shown in Fig. 5.50. For the fourth constraint configuration, face AA'B'B is fixed. The other end of the workpiece is free to deflect. Other faces are free to deform. This configuration corresponds to welding away from the fixed face. Figures 5.51 to 5.53 highlight the x-, y-, and z-directional deformation of the workpiece. Welding parameters are: welding current 150A, arc length 3mm, welding speed 2.5mm/s, and 100ppm of oxygen. The total deformation of the workpiece is shown in Fig. 5.54. For the fifth constraint configuration, edges CC' and DD' are fixed. The other end of the workpiece is free to deflect. Other faces are free to deform. This configuration corresponds to welding toward the fixed edges. Figures 5.55 to 5.57 highlight the x-, y-, and z-directional deformation of the workpiece. Welding parameters are: welding current 150A, arc length 3mm, welding speed 2.5mm/s, and 100ppm of oxygen. The total deformation

of the workpiece is shown in Fig. 5.58. For the sixth constraint configuration, face CC'D'D is fixed. The other end of the workpiece is free to deflect. Other faces are free to deform. This configuration corresponds to welding toward the fixed face. Figures 5.59 to 5.61 highlight the x-, y-, and z-directional deformation of the workpiece. Welding parameters are: welding current 150A, arc length 3mm, welding speed 2.5mm/s, and 100ppm of oxygen. The total deformation of the workpiece is shown in Fig. 5.62.

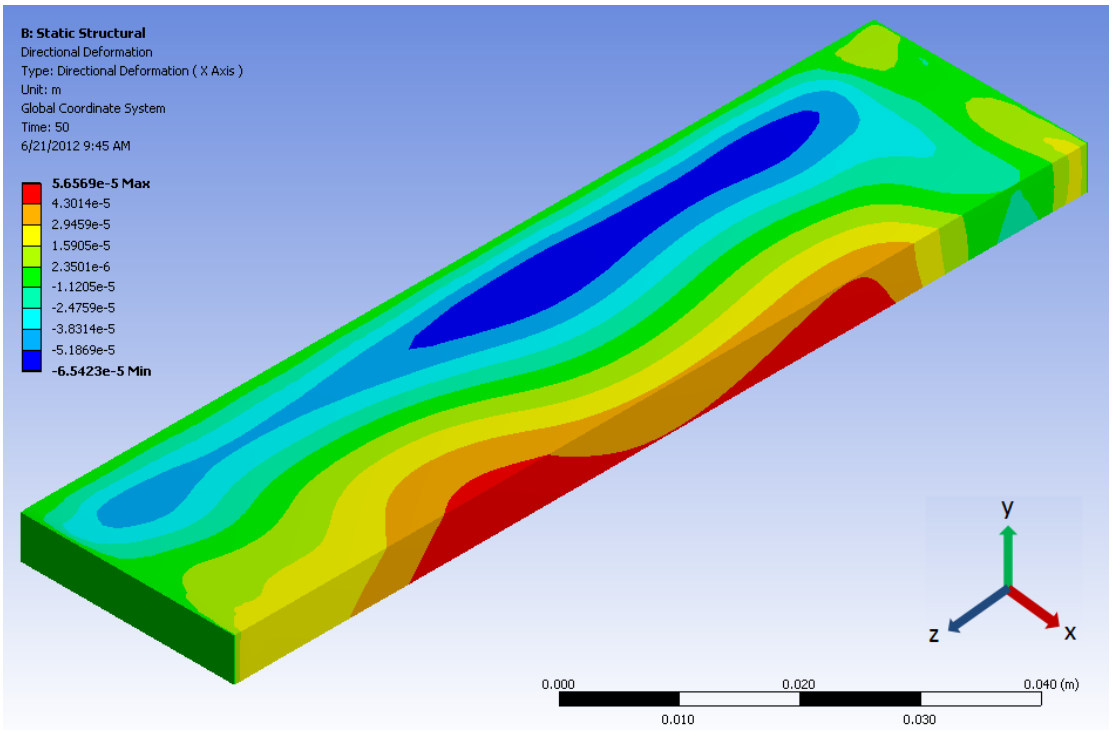


Figure 5.39: X-direction deformation (in m) of the workpiece. Faces ABB'A' & DCC'D' fixed.

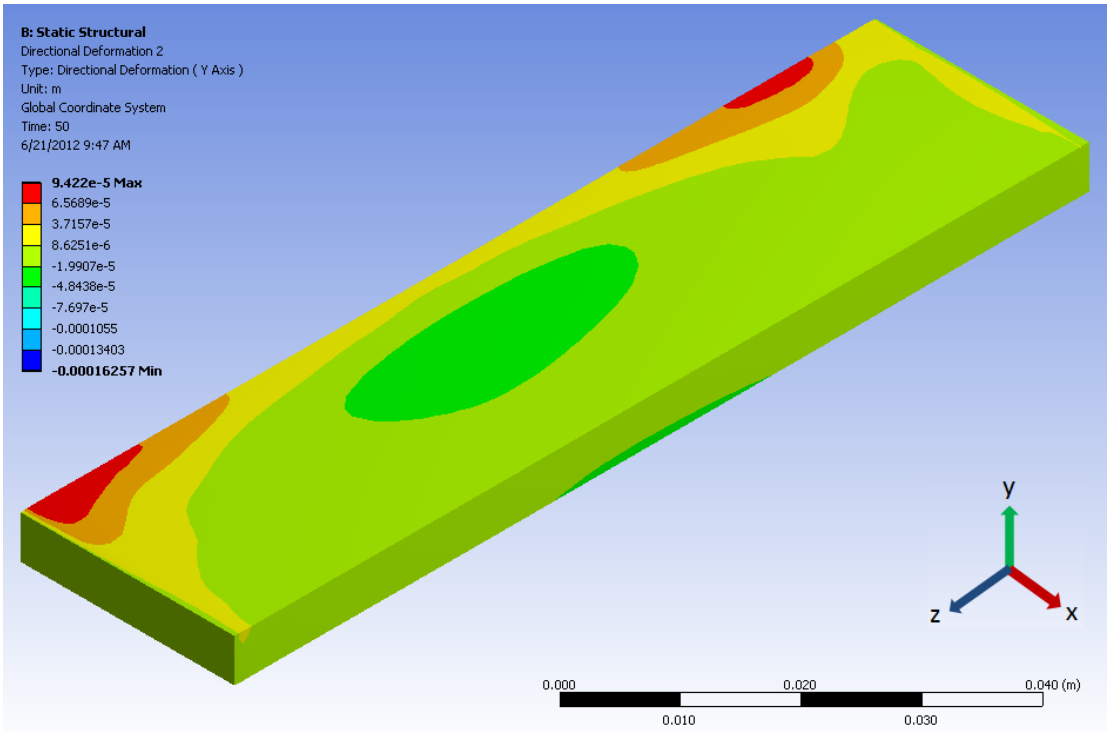


Figure 5.40: Y-direction deformation (in m) of the workpiece. Faces ABB'A' & DCC'D' fixed.

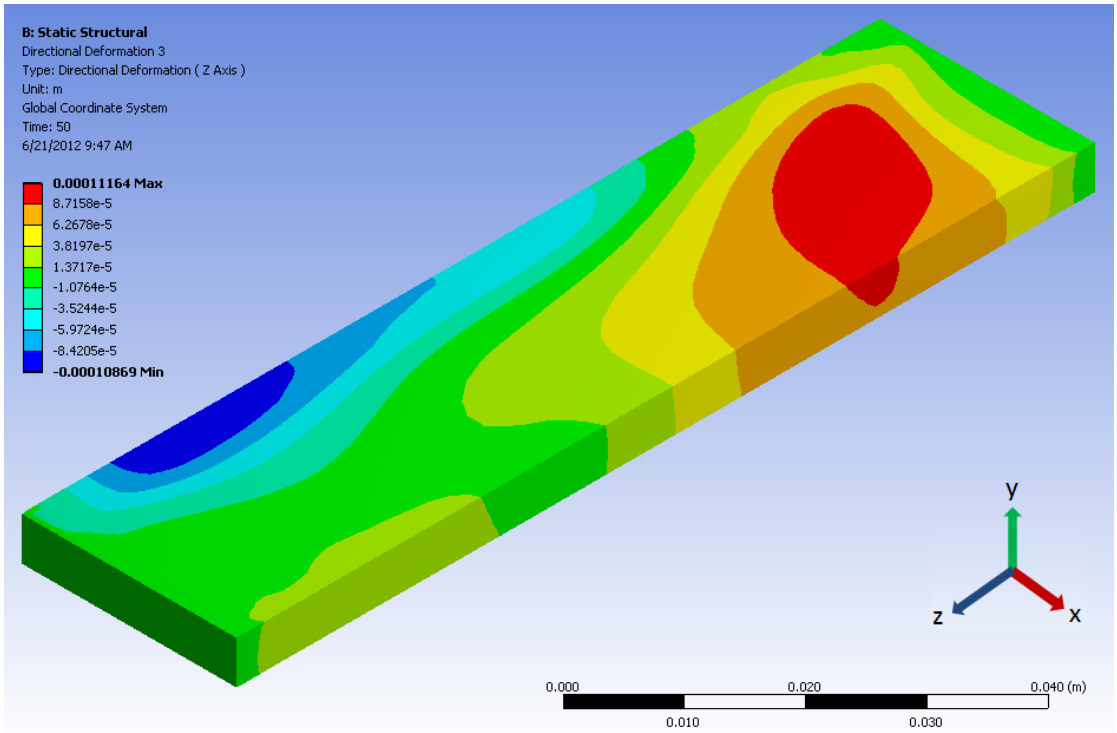


Figure 5.41: Z-direction deformation (in m) of the workpiece. Faces ABB'A' & DCC'D' fixed.

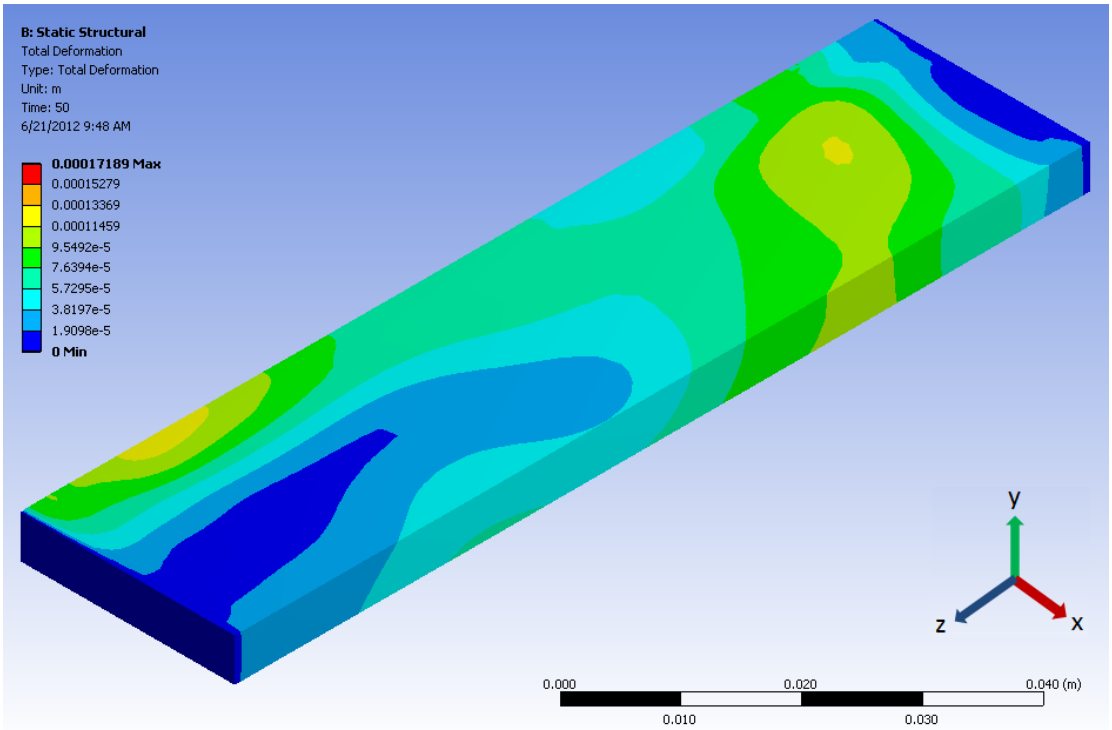


Figure 5.42: Total deformation (in m) of the workpiece. Faces ABB'A' & DCC'D' fixed.

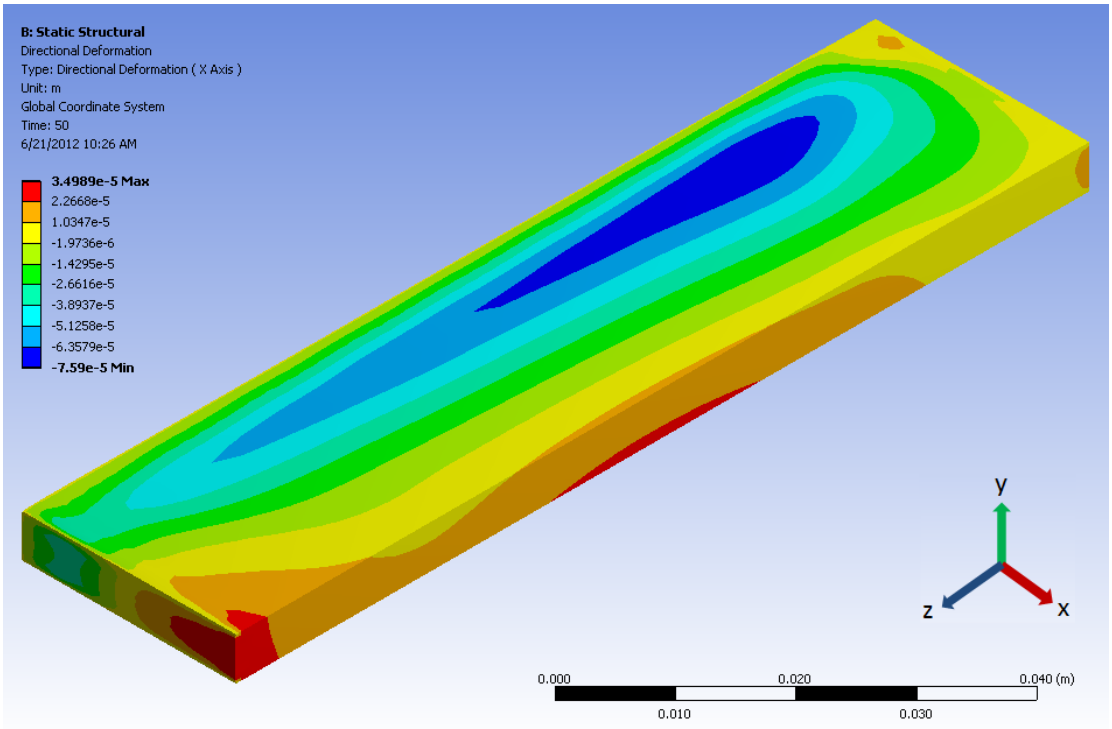


Figure 5.43: X-direction deformation (in m) of the workpiece. Edges AA', BB', CC', DD' fixed.

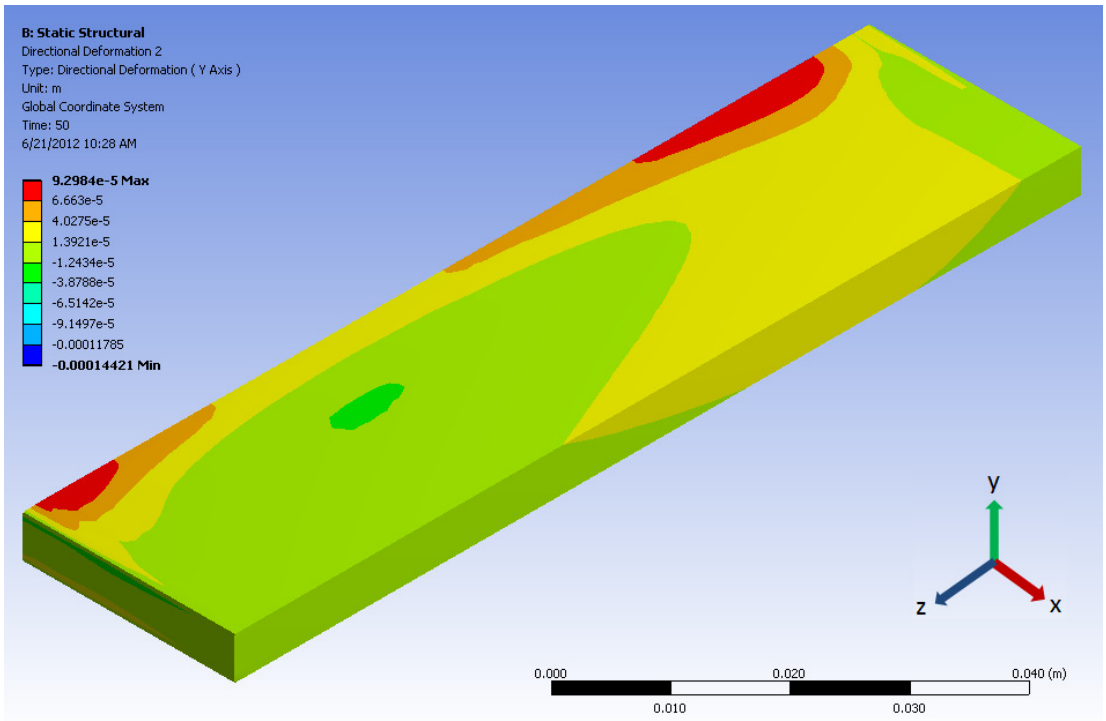


Figure 5.44: Y-direction deformation (in m) of the workpiece. Edges AA', BB', CC', DD' fixed.

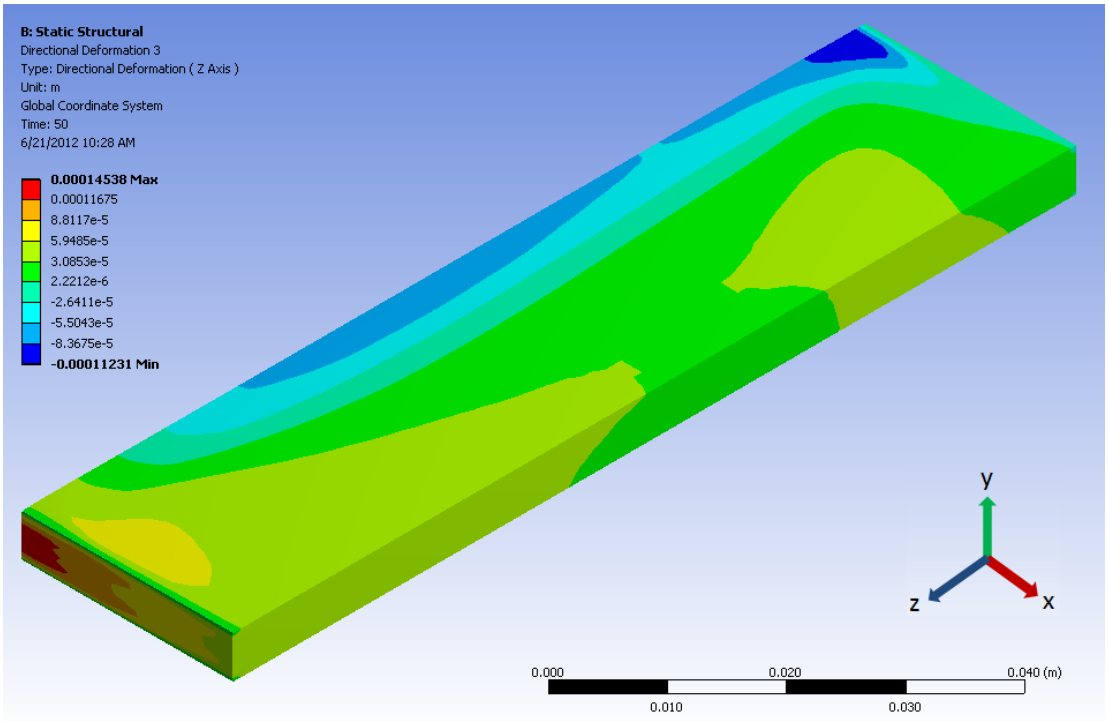


Figure 5.45: Z-direction deformation (in m) of the workpiece. Edges AA', BB', CC', DD' fixed.

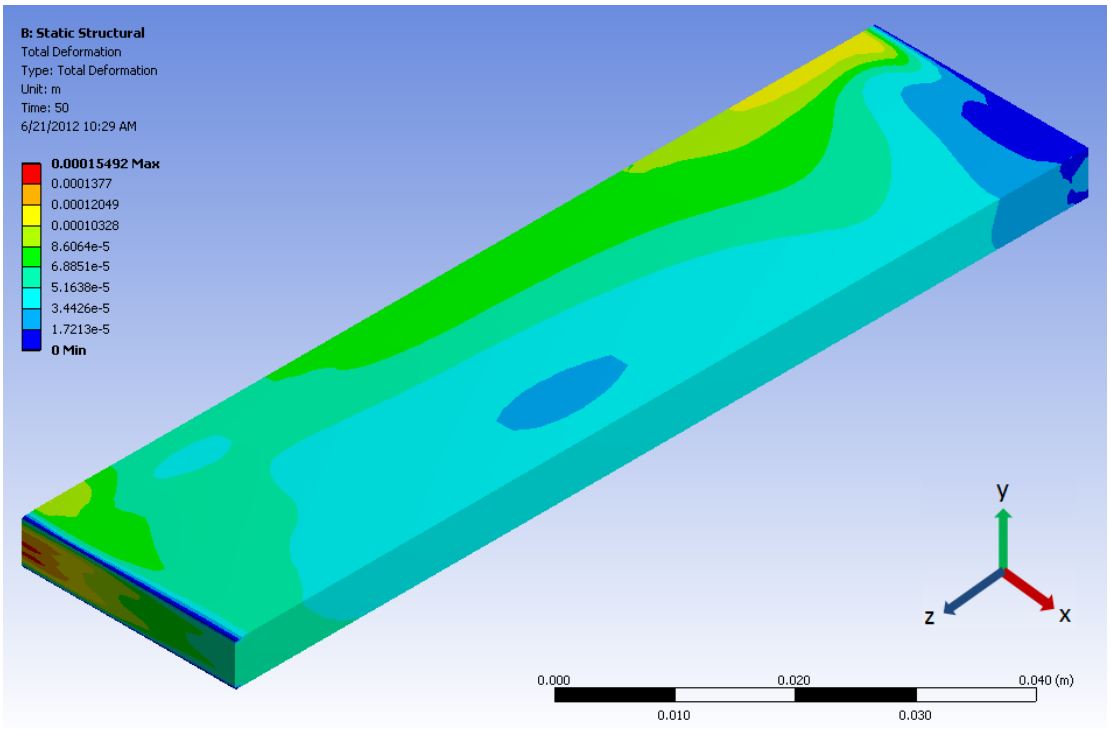


Figure 5.46: Total deformation (in m) of the workpiece. Edges AA', BB', CC', DD' fixed.

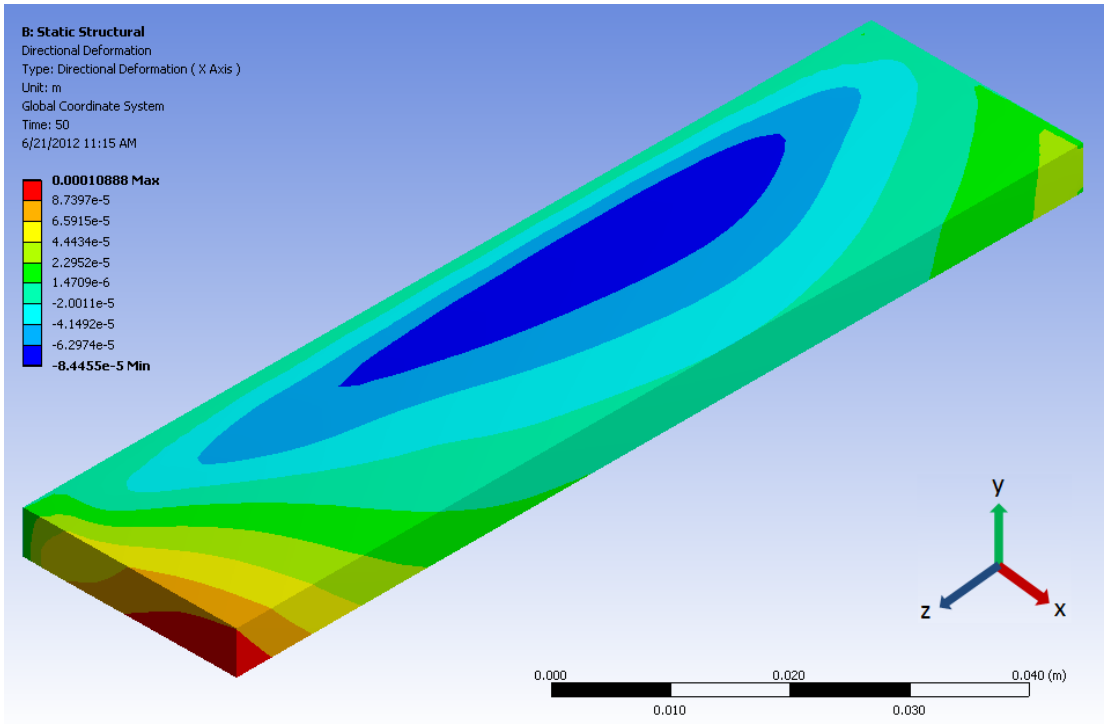


Figure 5.47: X-direction deformation (in m) of the workpiece. Edges AA', BB' fixed.

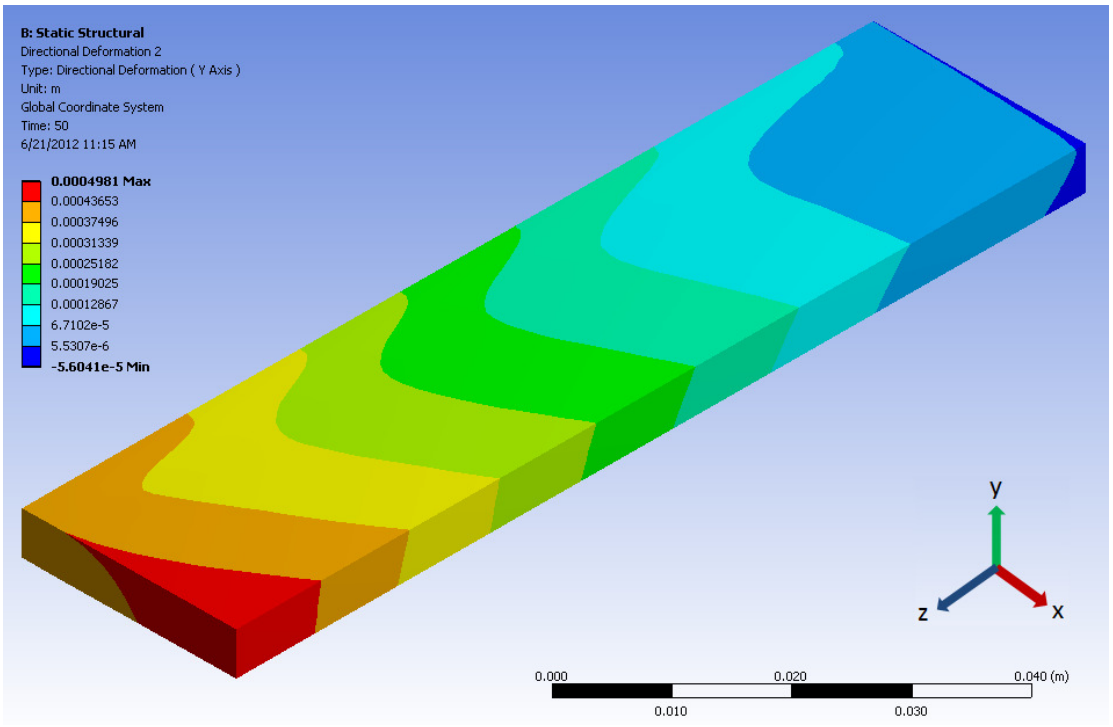


Figure 5.48: Y-direction deformation (in m) of the workpiece. Edges AA', BB' fixed.

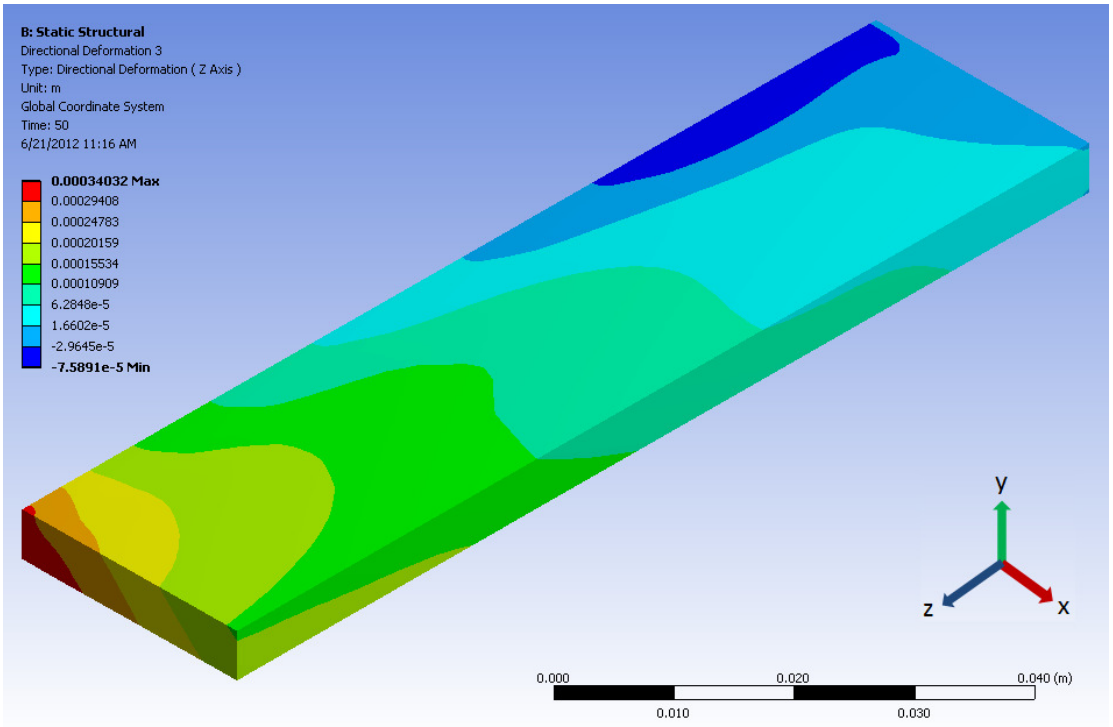


Figure 5.49: Z-direction deformation (in m) of the workpiece. Edges AA', BB' fixed.

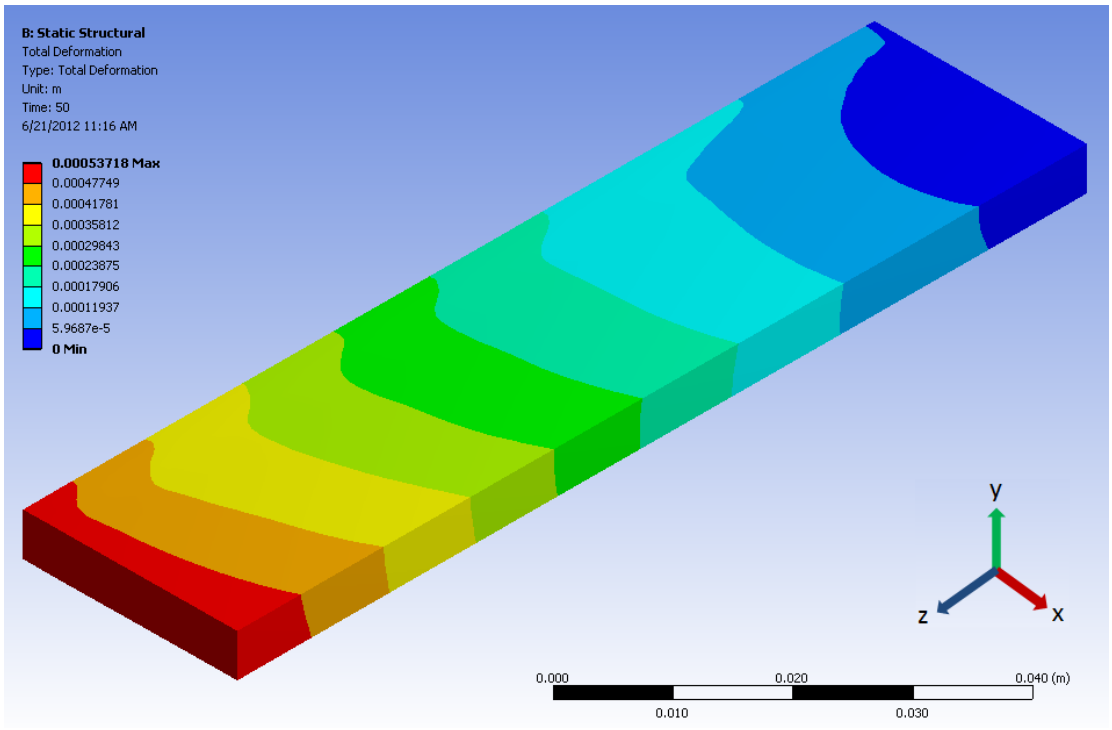


Figure 5.50: Total deformation (in m) of the workpiece. Edges AA', BB' fixed.

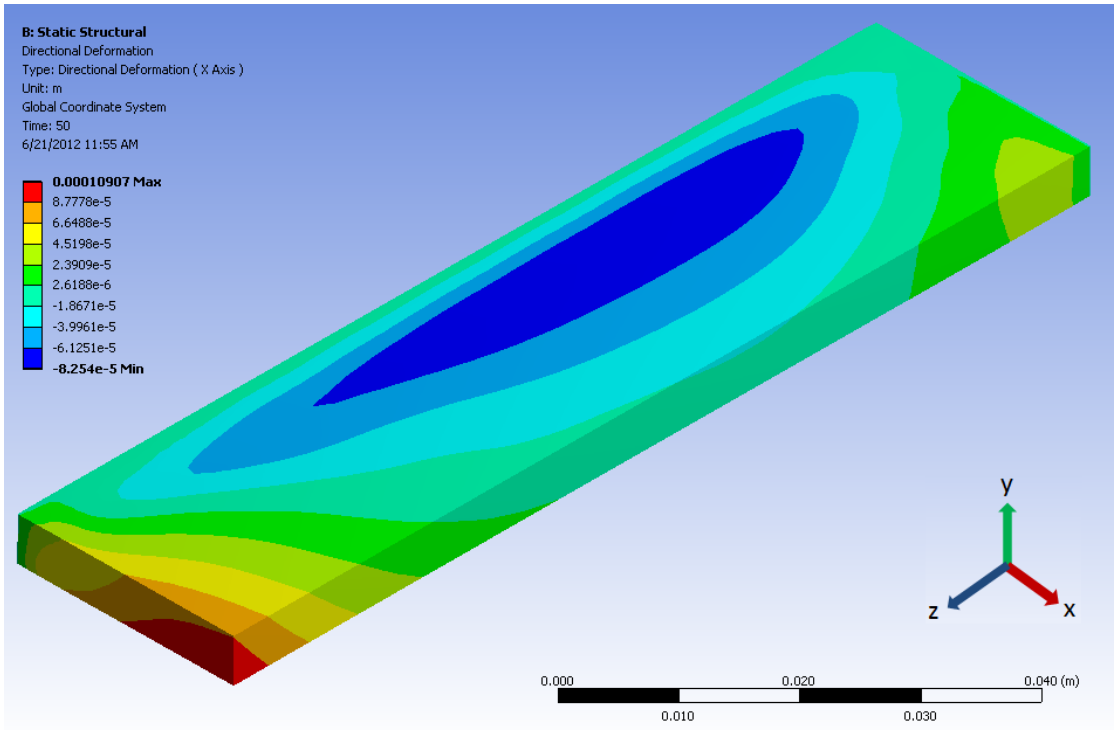


Figure 5.51: X-direction deformation (in m) of the workpiece. Face AA'B'B is fixed.

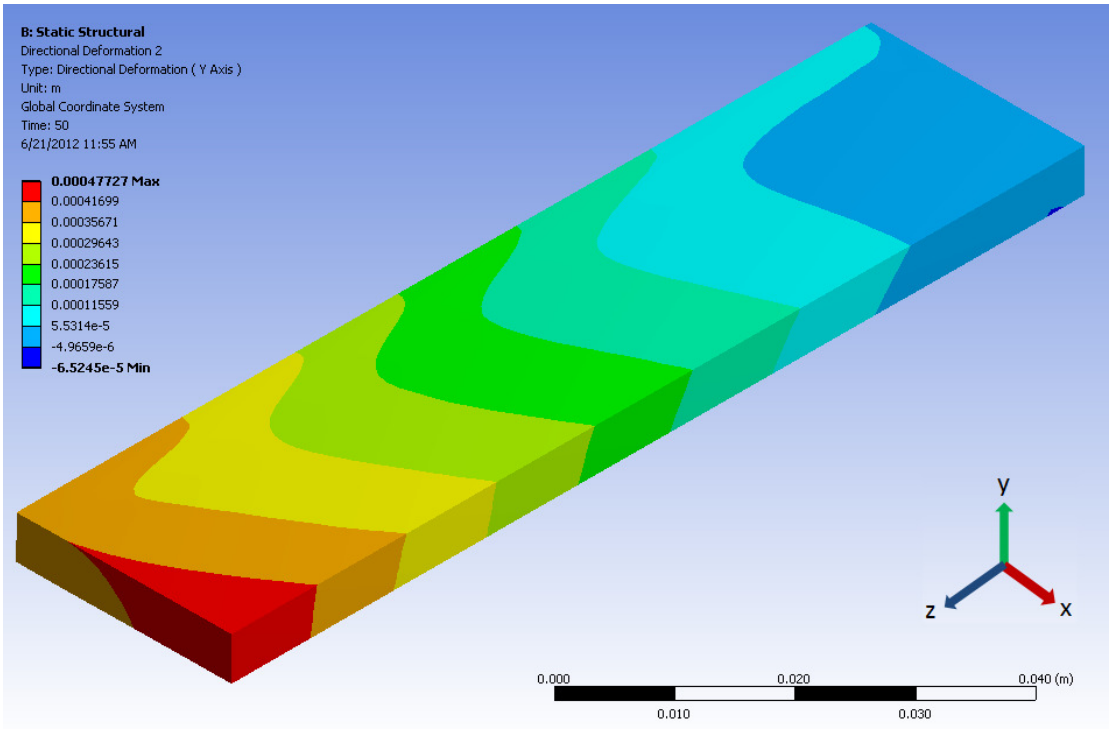


Figure 5.52: Y-direction deformation (in m) of the workpiece. Face AA'B'B is fixed.

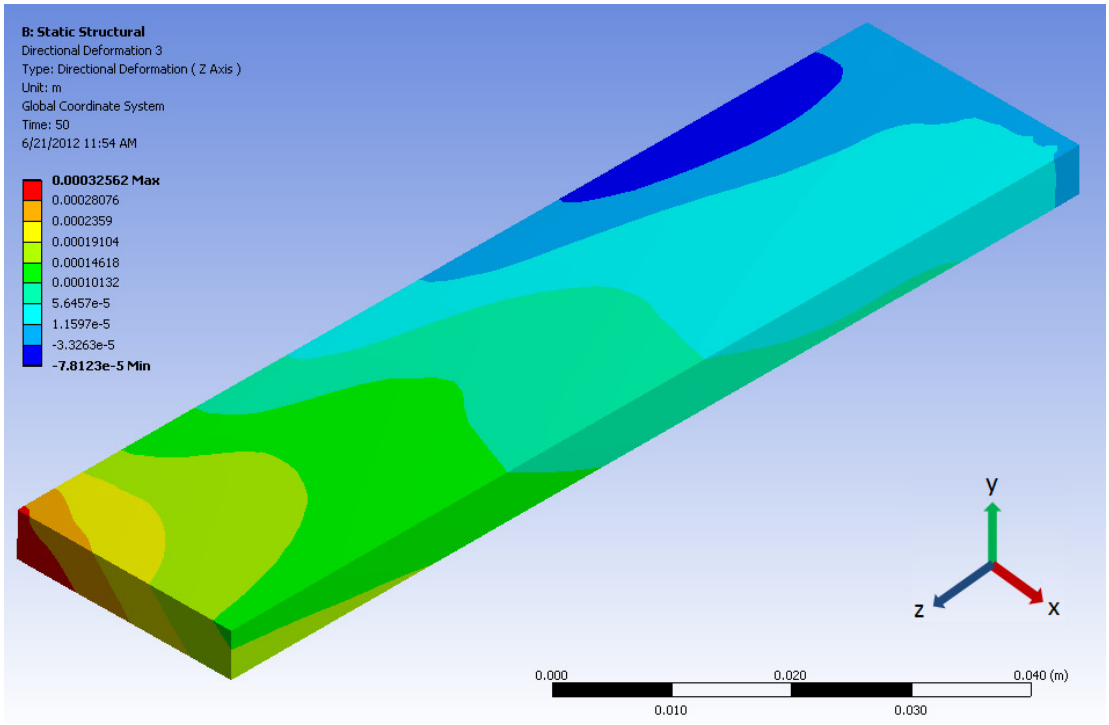


Figure 5.53: Z-direction deformation (in m) of the workpiece. Face AA'B'B is fixed.

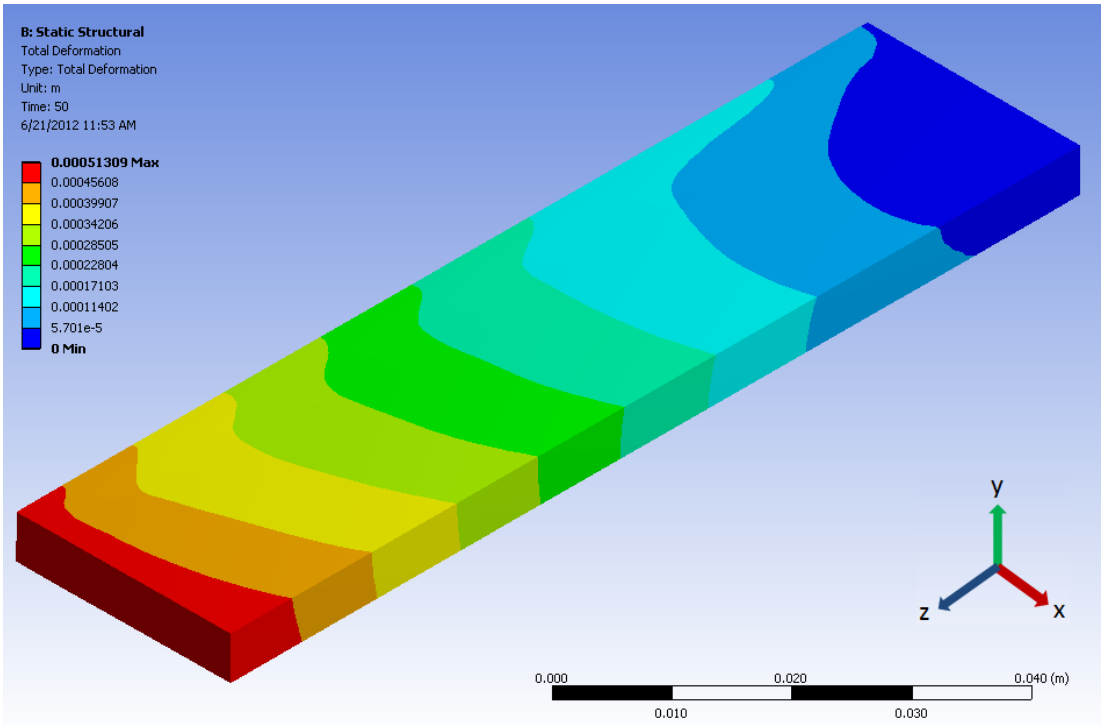


Figure 5.54: Total deformation (in m) of the workpiece. Face AA'B'B is fixed.

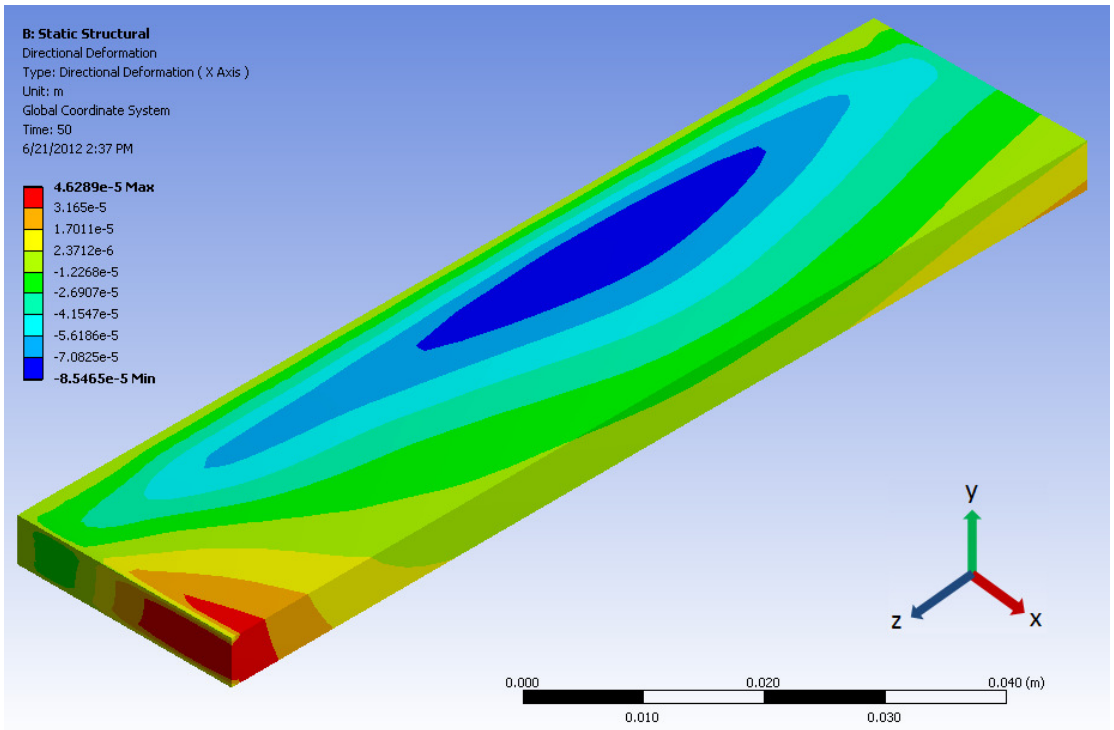


Figure 5.55: X-direction deformation (in m) of the workpiece. Edges CC', DD' fixed.

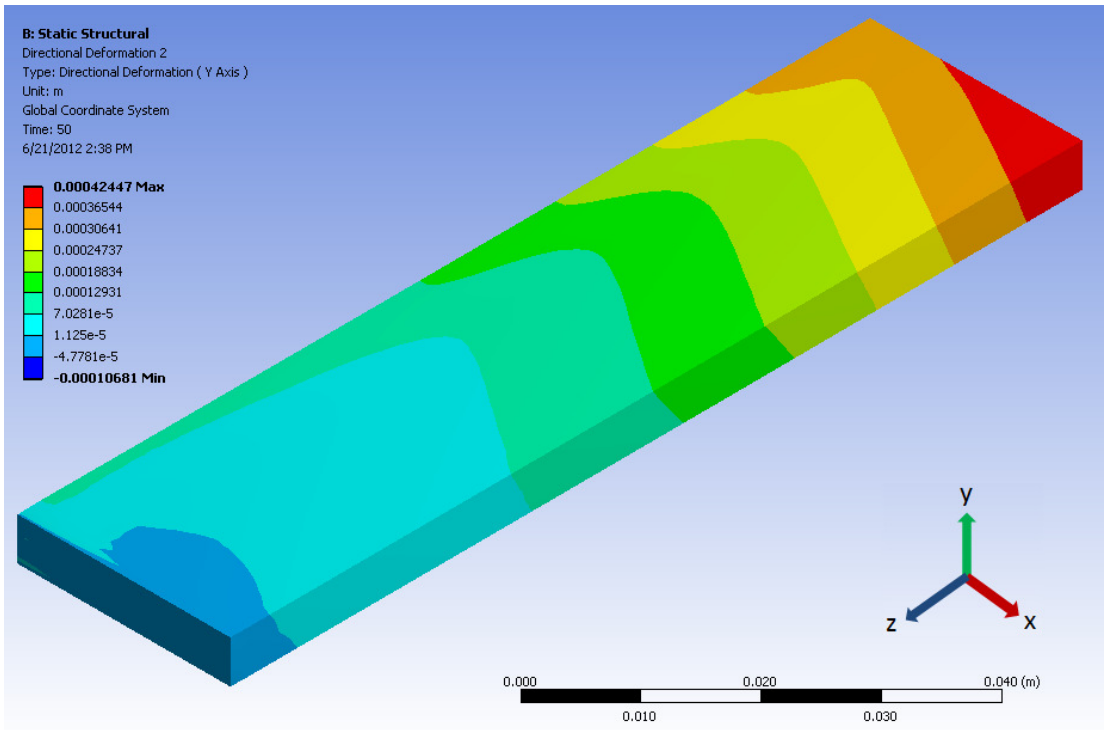


Figure 5.56: Y-direction deformation (in m) of the workpiece. Edges CC', DD' fixed.

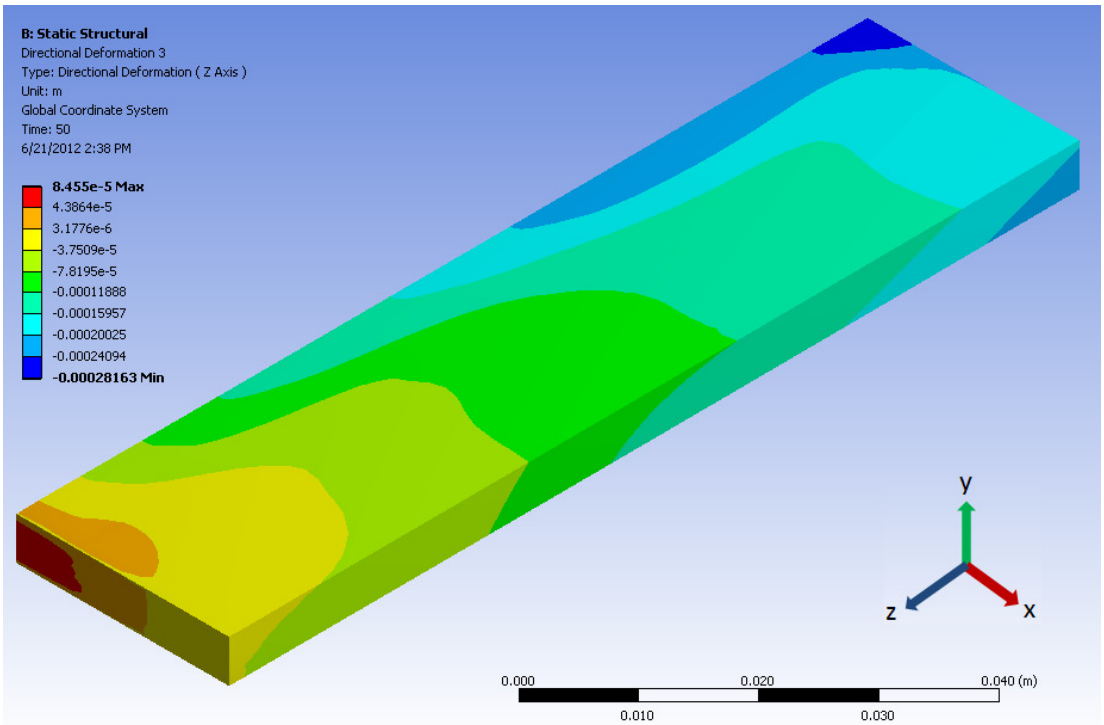


Figure 5.57: Z-direction deformation (in m) of the workpiece. Edges CC', DD' fixed.

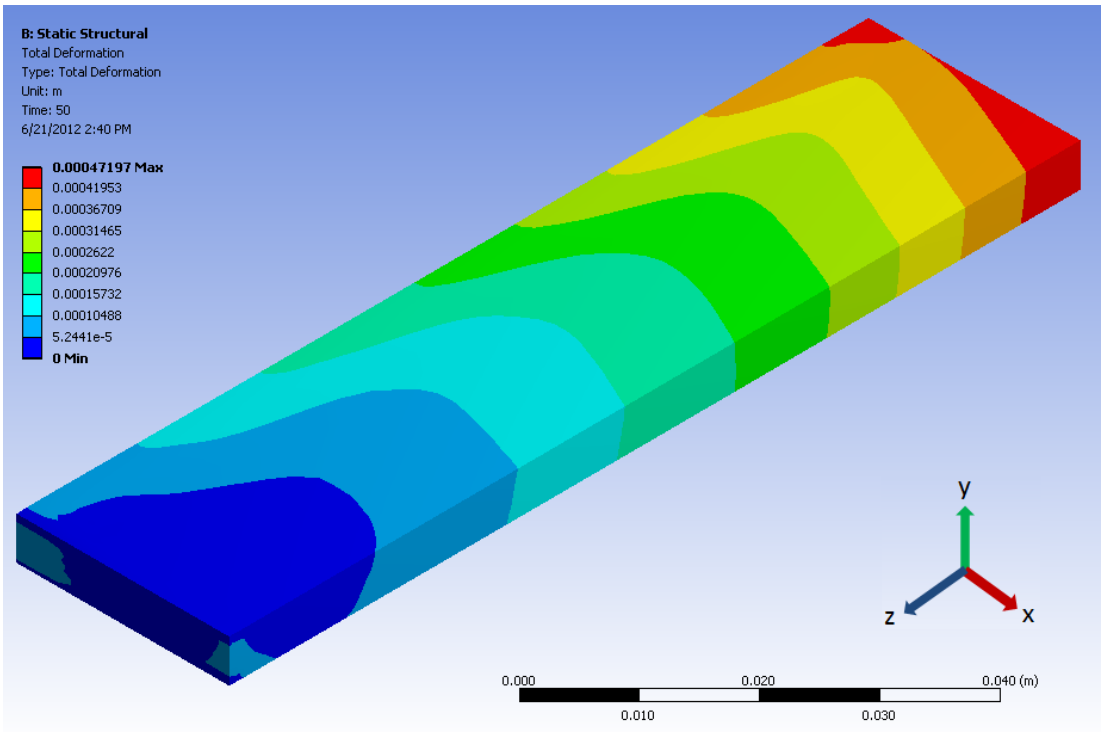


Figure 5.58: Total deformation (in m) of the workpiece. Edges CC', DD' fixed.

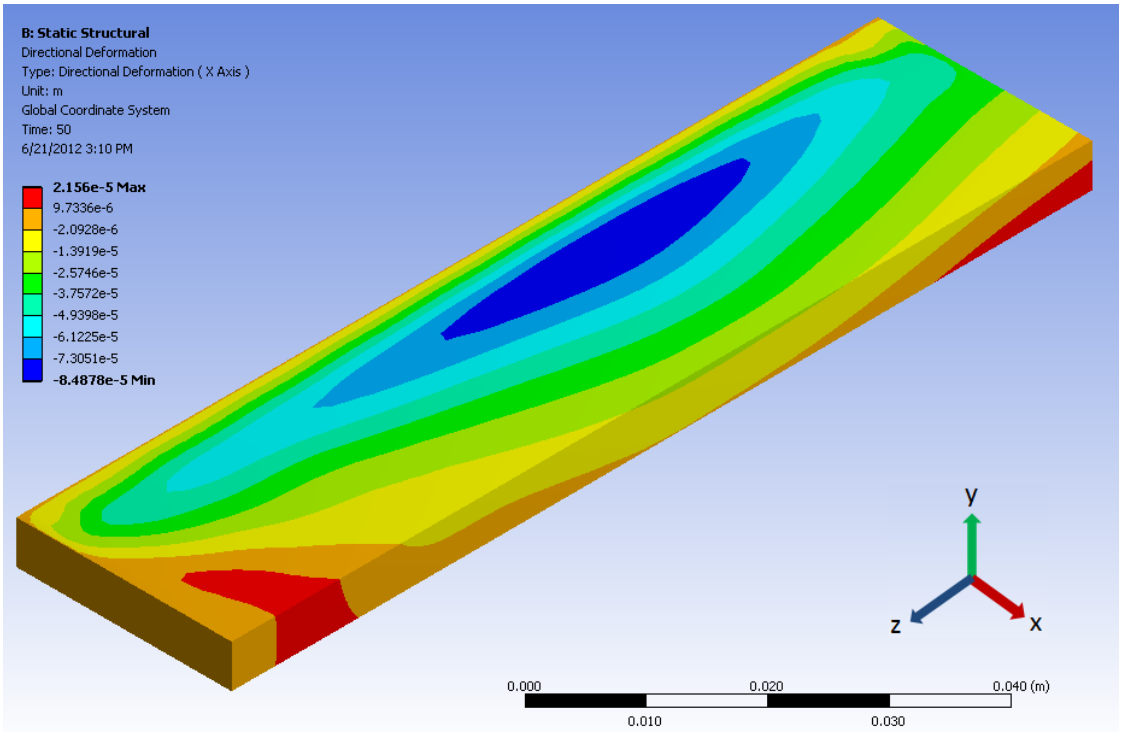


Figure 5.59: X-direction deformation (in m) of the workpiece. Face CC'DD' is fixed.

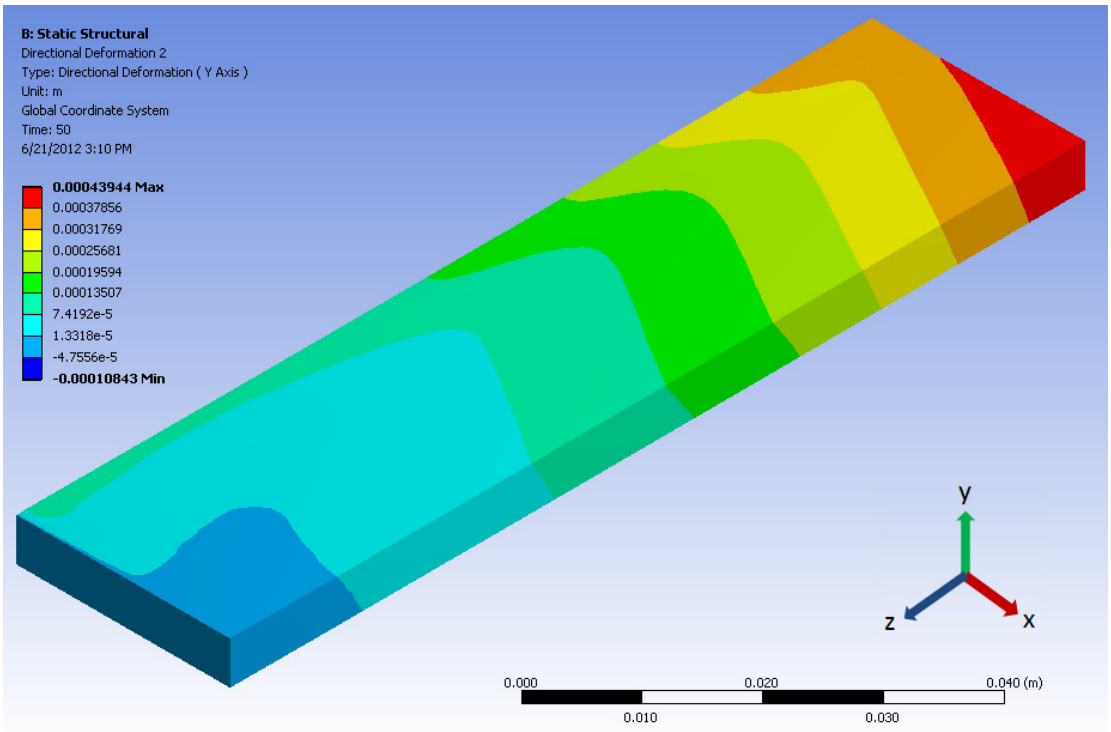


Figure 5.60: Y-direction deformation (in m) of the workpiece. Face CC'DD' is fixed.

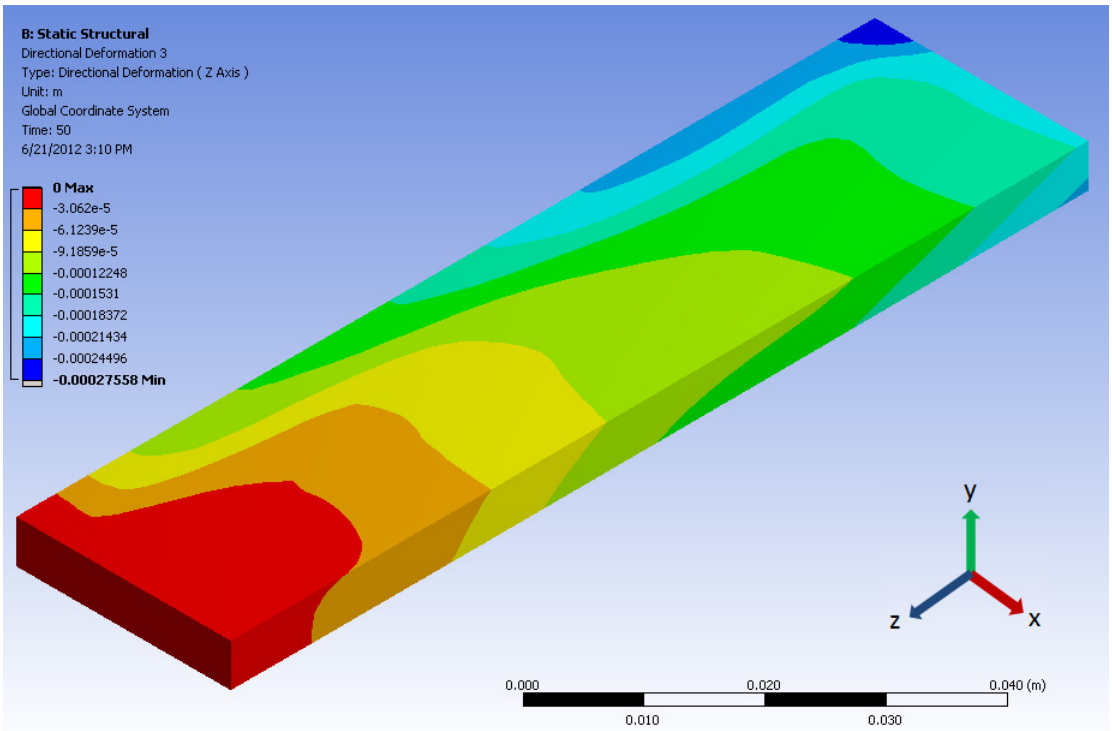


Figure 5.61: Z-direction deformation (in m) of the workpiece. Face CC'DD' is fixed.

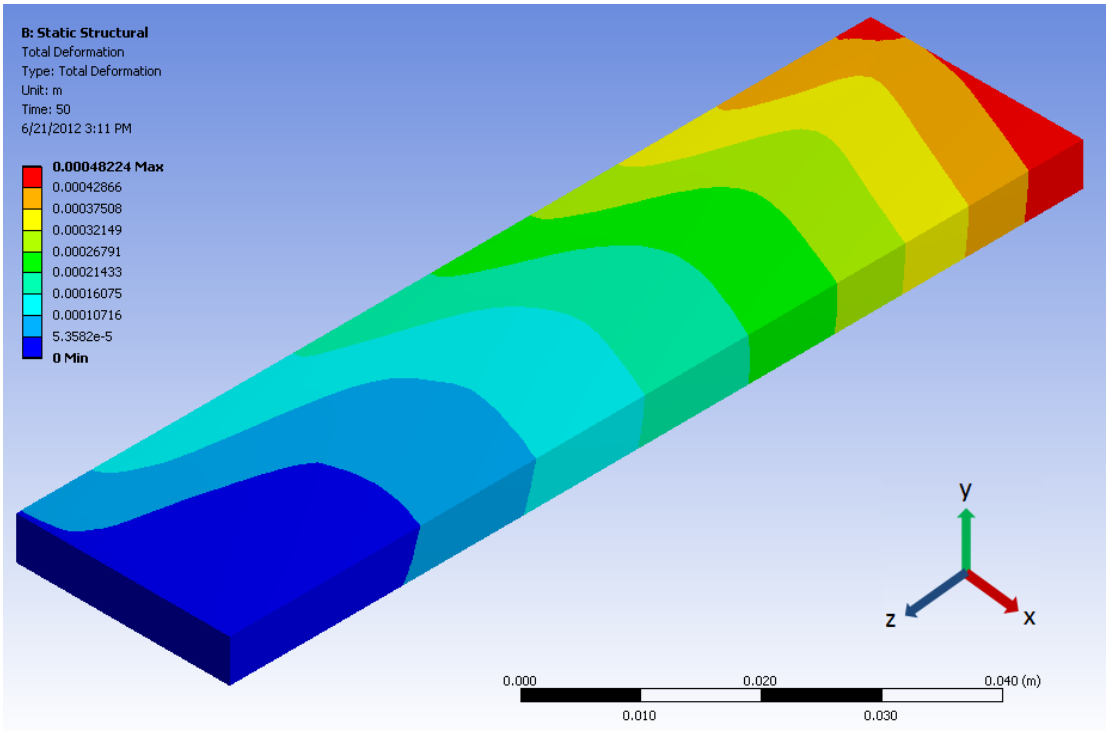


Figure 5.62: Total deformation (in m) of the workpiece. Face CC'DD' is fixed.

### 5.3.2 Stress Distributions

It is to be noted that the developed stresses obtained from the FE solver are influenced by the nature of the constraints applied. Additionally, we note that the welding bead is symmetrical about the welding axis, and normal stress components prevail in the weld. The results highlighted here are for the parameters: welding current 150A, welding speed 2.5mm/s, arc length 3mm, and a sulphur content of 100ppm. The results are highlighted on a xy-plane in the middle of the workpiece.

A stress parallel to the direction of the weld bead is called the longitudinal residual stress. Figure 5.63 represents the distribution of longitudinal stress SZ on the top of the weld. The longitudinal residual stress develops due to unequal longitudinal expansion/contraction during welding. Along the weld line, a high tensile stress is developed near the weld centerline, decreases to zero and then becomes compressive in nature on moving away from the weld bead.

Similarly, a stress perpendicular to the direction of the weld bead is called the transverse residual stress. Figure 5.64 depicts the distribution of the transverse stress SX on the top of the weld. This stress arises due to unequal transverse expansion/contraction during welding. The stress is tensile in nature near the weld edge, and decreases close to zero as the distance from the weld bead increases. The longitudinal and transverse stress distributions highlighted here represent the same distribution trends as have been shown from previous experiments and FEM simulations. Figures 5.65-5.70 highlight the von-Mises stress distributions in the workpiece for first to sixth constraint configuration, respectively.

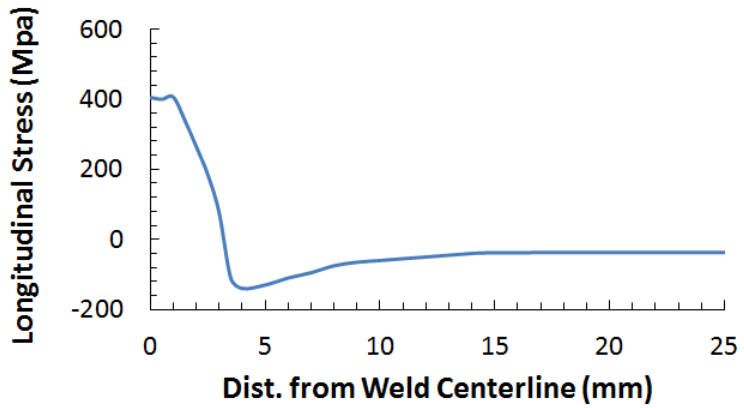


Figure 5.63: Longitudinal stress distribution across the weld on the top surface.

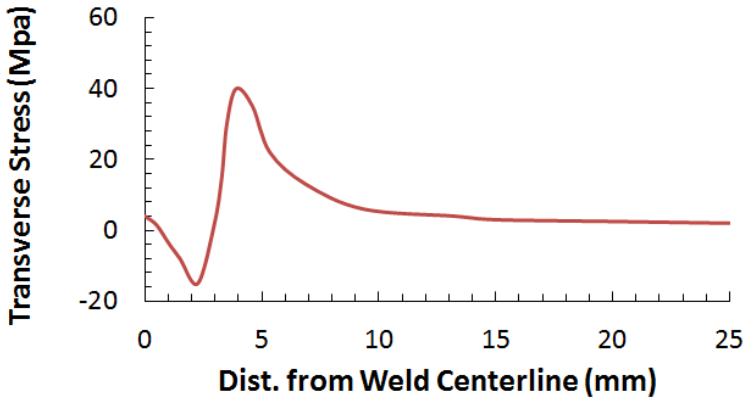


Figure 5.64: Transverse stress distribution across the weld on the top surface.

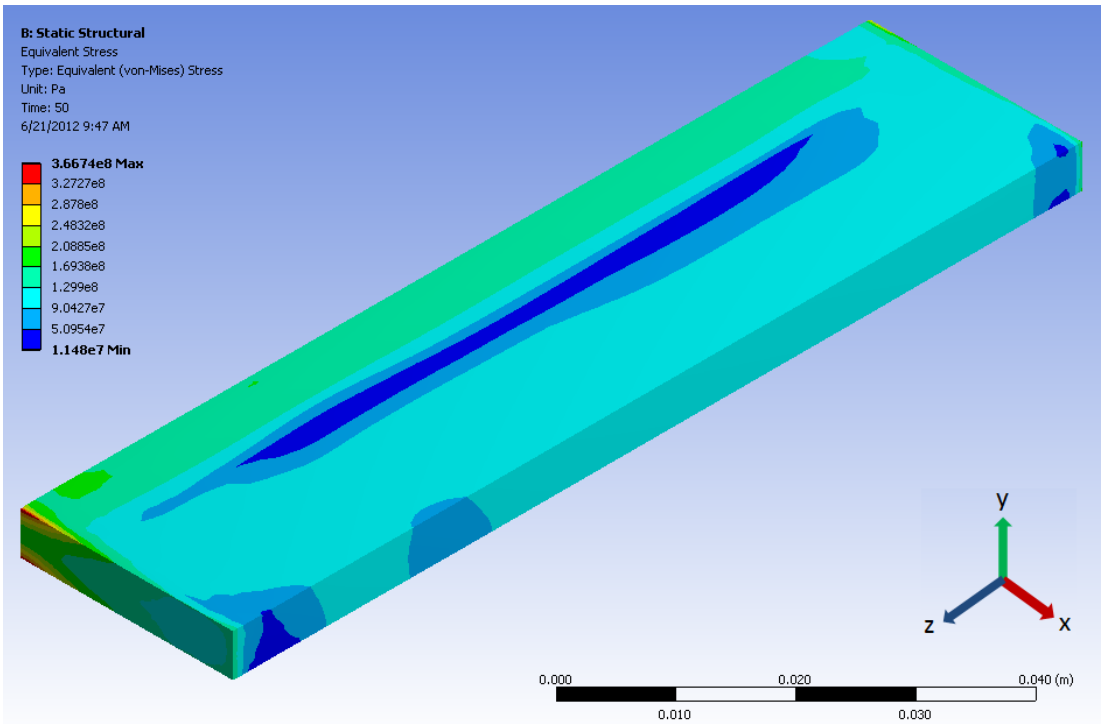


Figure 5.65: Distribution of von-Mises stress. Faces AA'BB' and CC'DD' are fixed.

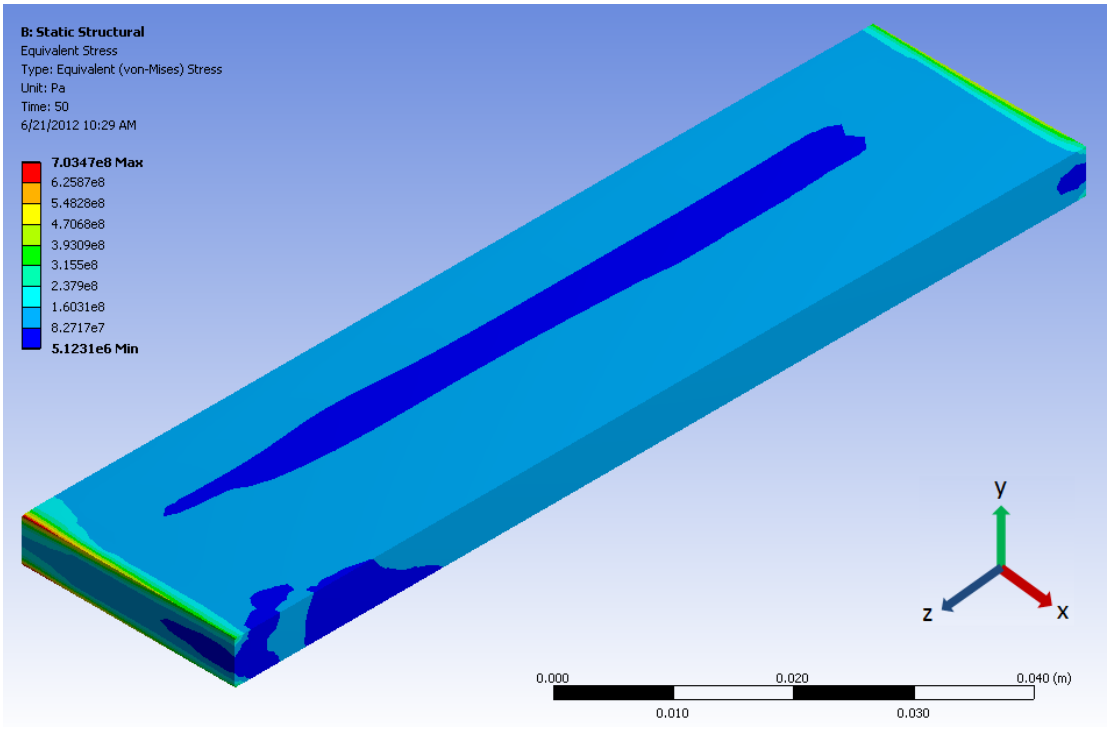


Figure 5.66: Distribution of von-Mises stress. Edges AA', BB', CC' and DD' are fixed.

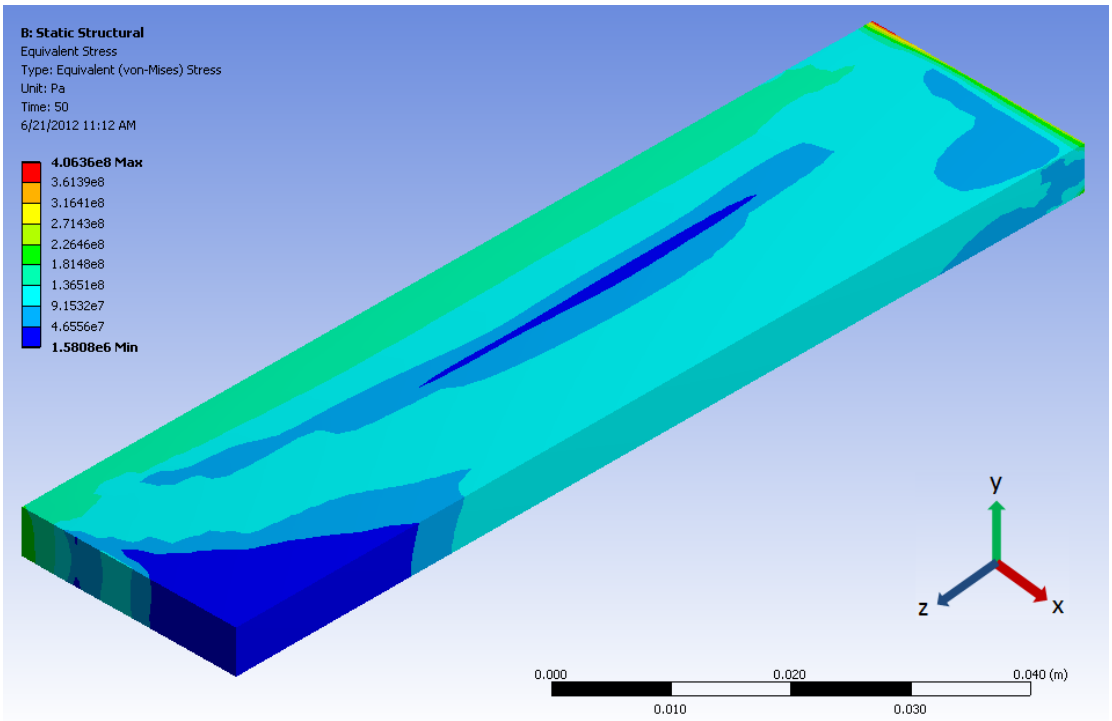


Figure 5.67: Distribution of von-Mises stress. Edges AA' and BB' are fixed.

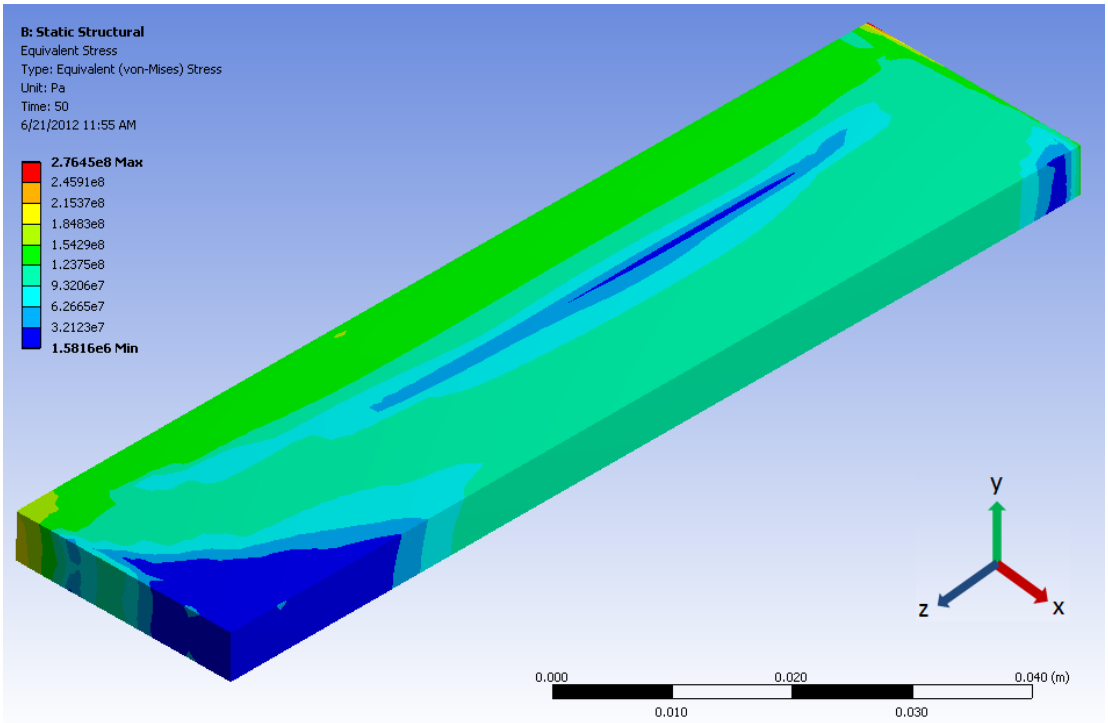


Figure 5.68: Distribution of von-Mises stress. Face AA'BB' is fixed.

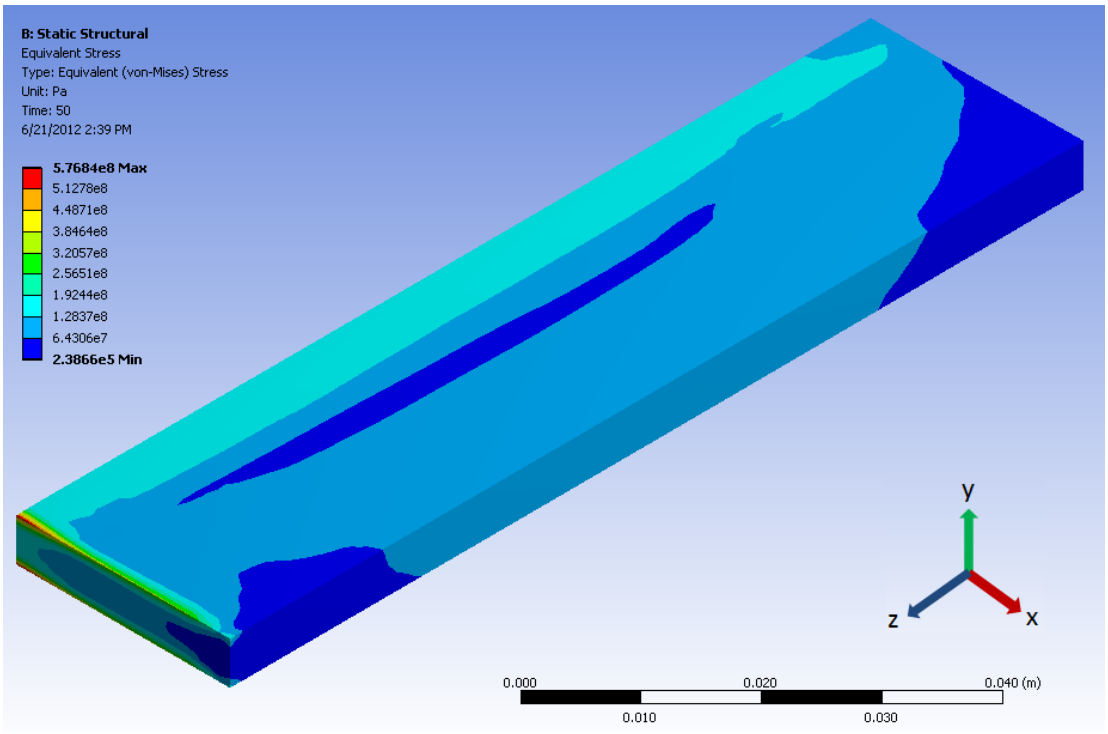


Figure 5.69: Distribution of von-Mises stress. Edges CC' and DD' are fixed.

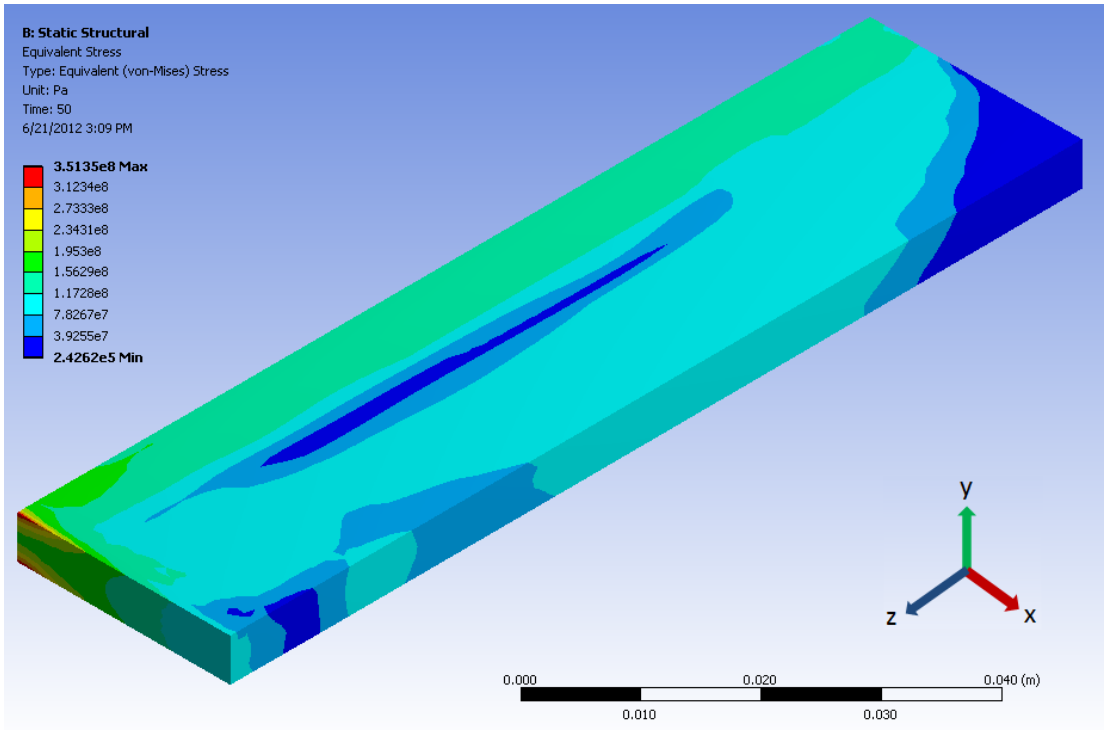


Figure 5.70: Distribution of von-Mises stress. Face CC'DD' is fixed.

# Chapter 6

# Conclusion and Future Work

The specific contributions of this dissertation include (i) incorporating the thermal energy redistribution due to weld pool dynamics into the thermo-mechanical modeling of welded joints by coupling the weld pool dynamics field with the remaining fields in the welding process, (ii) incorporating all the major and contributing driving forces into the weld pool dynamics modeling, (iii) incorporating the effects of arc length/electrode gap and electrode angle on the arc heat flux and current density distributions, (iv) indirectly incorporating the microstructure influence on mechanical behavior through material modeling, and (v) showing through simulations that employment of temperature-dependent thermophysical properties give better weld D/W ratio prediction.

In the present investigation, a numerical model has been developed for the coupled field analysis of GTA welding process. The arc heat flux and current density distribution on the workpiece have been compared with experimental data from existing literature. They agree well and prove correct incorporation of arc effects in the weld pool dynamics model. The weld D/W ratio obtained from the simulations has been compared with experimental data. The agreement is better when temperature-dependent thermophysical properties were employed instead of constant values.

Detailed parametric studies have been performed to delineate the effects of various welding parameters on the weld D/W ratio. Simulations are run with temperature-dependent thermophysical properties. The results have been compared with experimental data. Also, the percent error in prediction of weld D/W from the present model has been calculated. The parameters of particular interest are welding current, welding speed, arc length or electrode gap, electrode angle, and surface active agent content. For each of these parameters, simulations were run for both low (≤40ppm) and high (≥150ppm) surface active agent content. When current is varied, the weld D/W ratio slightly increases and then gradually decreases to a value of ~0.16 at 30ppm of oxygen. However, at 150ppm of oxygen, the weld D/W ratio increases and then

remains constant at ~0.45 over welding current of 160A. The error in prediction is ≤10% till 160A for both low and high oxygen content. However, beyond 160A, the error is between 10-15% for low surface active agent content. When the welding speed is varied, the weld D/W ratio almost remains the same at low (≤40ppm) of oxygen. However, under high (≥150ppm) oxygen content, the weld D/W ratio decreases with increasing welding speed. Under low surface active agent content, the error is ≤15% at lower welding speeds. The error is ≤10% at higher speeds. However, under high surface active agent content, the error is ~10% at low welding speeds and the error reduces ≤5% at higher welding speeds. When the arc length or electrode gap is varied, the weld D/W ratio almost remains the same at low (≤40ppm) of oxygen. However, under high (≥150ppm) oxygen content, the weld D/W ratio decreases with increasing arc length. Under low surface active agent content, the error is ≤12% at lower arc lengths. The error is ≤10% at higher arc lengths. The weld D/W ratio increases very weakly with increasing electrode tip angle. Making the electrode tip blunter achieves better arc constriction which helps to slightly enhance the weld D/W ratio. The weld D/W ratio increases from 0.42 to 0.5 for electrode tip angle increase from $30^{o}$ to $90^{o}$. However, the weld D/W ratio undergoes significant increase when the surface active agent content is increased. Based on the operating parameters used, decreasing the oxygen content below 40ppm has no effect on the weld D/W ratio. Similarly, increasing the oxygen content beyond 150ppm has no effect on D/W ratio. When oxygen content is ≤40ppm, the weld D/W ratio remains constant at ~0.2. When the oxygen content is ≥150ppm, the weld D/W ratio remains constant at ~0.45. These values are true for the operating conditions used. For other operating parameters, the trend/behavior of weld D/W ratio will be the same, but values will differ.

The present investigation also predicts the weld solidification mode by analyzing weld pool dynamics simulation results. The temperature gradient at the weld fusion line and centerline decreases with increasing welding speed. However, temperature gradient at the fusion line is greater. This holds true for the welding parameters used. It has been calculated that with increase in welding speed, the value of $G*R$ is increased while the value of $G/R$ is reduced at the weld pool centerline. Hence, with increase in welding speed finer substructures would be obtained. Also, with increase in welding speed dendritic microstructures may be obtained.

Variation of weld D/W ratio with heat input per unit length of weld is also calculated. The heat input is varied in two ways – (a) varying the welding current and (b) varying the welding speed. When welding current is changed, in case of high oxygen content, it is seen that with increasing heat input the weld D/W ratio increases steadily and then levels off. Beyond 750J/mm the weld D/W ratio remains constant at ~0.45. Hence, increasing the heat input beyond this value would only increase the HAZ with no desired increase in weld D/W ratio. In case of low oxygen content, it can be seen that with increasing the heat input the weld D/W ratio decreases. The rate of decrease of weld D/W ratio lowers from 750J/mm onwards. The maximum weld D/W ratio is obtained around 500-550J/mm. When welding speed is varied, in case of high oxygen content, it is seen that with increasing heat input the weld D/W ratio increases steadily. The rate of increase of weld D/W ratio lowers from 750J/mm onwards. Beyond 750J/mm the percent increase in weld D/W ratio is ~14% for ~87% increase in heat input per unit length of weld. Since increasing the heat input results in slower cooling rate and enlarges the HAZ, the benefits of increasing the heat input per unit length beyond 750J/mm is not justified. In case of low oxygen content, it can be seen that with increasing the heat input the weld D/W ratio decreases quickly and then maintains a constant value of ~0.18. The maximum weld D/W ratio is obtained around 250J/mm. An important observation that has been made is that weld D/W ratio values do not correspond to each other for the same heat input per unit length value. Hence, changing the heat input value by either changing the welding current or welding speed has an influence on how the weld D/W ratio changes. Changing the heat input per unit length of the weld by varying either the current or speed will influence the important weld pool driving forces differently in a non-linear manner. The complex interplay of the driving forces determines the final weld D/W ratio. Hence, when analyzing weld D/W ratio plots versus heat input per unit length of weld, it is important that attention be paid as to how the changes in heat input were achieved.

Parametric simulation runs were also conducted using constant thermophysical properties. The weld D/W ratios are obtained with varying welding current, welding speed and arc lengths. In all the cases, it has been found that the weld D/W predictions are not as accurate as with temperature-dependent properties. The percent error between simulation and experimental data is high. Hence, based on the present simulations, it can be recommended that weld pool dynamics simulations be always conducted with temperature-dependent thermophysical properties.

Structural analysis of the welded joint highlights the deformation of the welded butt joint under various constraint configurations. The effect of welding direction (toward/away from) the fixed edge/face has also been studied. The von-Mises stress distributions under these constraint configurations have also been highlighted. The longitudinal and transverse stress distributions across and on the top of the weld have also been calculated. Along the weld line, a high tensile longitudinal stress is developed near the weld centerline, decreases to zero and then becomes compressive in nature on moving away from the weld bead. The transverse stress is tensile in nature near the weld centerline, and decreases close to zero as the distance from the weld bead increases. The longitudinal and transverse stress distributions highlighted from the present study represent the same distribution trends as seen from previous experiments and FEM simulations. The coupled field modeling of GTA welding provides a more accurate thermal energy distribution for structural analyses. Through material modeling the effects of microstructure evolution on mechanical behavior has been indirectly incorporated. Thermally-induced stress distribution and workpiece deformations have been reported. The mathematical framework developed here provides us with the tools to study the multi-physics problem of welding.

The present model incorporated all the major factors that influence the weld pool dynamics and finally determine the weld D/W ratio. However, this model works very well for welding currents $\leq$200A. The predictions from the present model will not agree very well with thicker plates and higher welding currents. Hence, the present model needs to be extended to incorporate arc pressure effects and filler material addition. Also, with higher welding current, surface deformation becomes an issue. Using VOF method, the present method can be extended to include the surface depression effects during welding. A future goal is to study stress relief methods on welded joints.

# References


[1] Kou, S. (2002) "Welding Metallurgy," Second Ed., John Wiley & Sons Publication

[2] Rosenthal, D. (1941) "Mathematical theory of heat distribution during welding and cutting," Welding Journal, 20:5:220s-234s

[3] Rosenthal, D. (1946) "The theory of moving source of heat and its application to metal treatments," ASME Transactions, 48:848-866

[4] Woods, R. A. and Milner, D. R. (1971) "Motion in weld pool in arc welding," Welding Journal, 50:4:163s-173s

[5] Heiple, C. R. and Roper, J. R. (1982) "Mechanism for minor element effect on GTA fusion zone geometry," Weld. J., 61:97s-102s

[6] Heiple, C. R. and Roper, J. R. (1982) "Effects of minor elements of GTAW fusion zone shape," Trends in Welding Research in the United States, 489-520

[7] Atthey, D. R. (1980) "A mathematical model for fluid flow in a weld pool at high currents," J. Fluid Mech., 98:4:787-801

[8] Oreper, G. M., Eagar, T.W. and Szekely, J. (1983) "Convection in arc weld pools," Welding Journal, 62:11:307-312

[9] Oreper, G. M. and Szekely, J. (1984) "Heat- and fluid-flow phenomena in weld pools," J. Fluid Mech., 147:53-79

[10] Kou, S. and Sun, D. K. (1985) "Fluid flow and weld penetration in stationary arc welds," Metallurgical Transactions A, 16A:203-213

[11] Kou, S. and Wang, Y. H. (1986) "Weld pool convection and its effect," Welding Journal, 65:3:63s-70s

[12] Heiple, C. R., Roper, J. R., Stagner, R. T. and Aden, R. J. (1983) "Surface active element effects on the shape of GTA, Laser, and electron beam welds" Weld. J., 62:72s-77s

[13] Bennett, W. S. and Mills, G. S. (1974) "GTA weldability studies on high manganese stainless steel," Welding Journal, 53:12:548s-553s

[14] Heiple, C. R. and Roper, J. R. (1981) "Effect of selenium on GTAW fusion zone geometry," Welding Journal, 60:8:143s-145s

[15] Heiple, C. R. and Burgardt, P. (1985) "Effects of SO2 shielding gas additions on GTA weld shape," Welding Journal, 64:6:159s-162s

[16] Sahoo, P., Debroy, T. and McNallan, M. J. (1988) "Surface tension of binary metal – Surface active solute systems under conditions relevant to welding metallurgy," Metallurgical Transactions B, 19B:483-491

[17] Zacharia, T., David, S. A., Vitek, J. M. and Debroy, T. (1989) "Weld pool development during GTA and laser beam welding of type 304 stainless steel part I. Theoretical analysis," Welding Journal, 68:12:499s-509s

[18] Zacharia, T., David, S. A., Vitek, J. M. and Debroy, T. (1989) "Weld pool development during GTA and laser beam welding of type 304 stainless steel part II. Experimental correlation," Welding Journal, 68:12:510s-519s

[19] McNallan, M. J. and Debroy, T. (1991) "Effect of temperature and composition on surface tension in Fe-Ni-Cr alloys containing sulphur," Metall. Trans. B, 22:4:557-560

[20] Lei, Y., Shi, Y., Murakawa, H. and Ueda, Y. (1997) "Numerical analysis of the effect of sulphur content upon fluid flow and weld pool geometry for type 304 stainless steel," Trans. JWRI, 26:1:1-8

[21] Pierce, S. W., Burgardt, P. and Olson, D. L. (1999) "Thermocapillary and arc phenomena in stainless steel welding," Welding Research supplement, 45s-52s

[22] Limmaneevichitr, C. and Kou, S. (2000) "Visualization of Marangoni convection in simulated weld pools containing a surface-active agent," Welding Journal, 79:324s-330s

[23] Limmaneevichitr, C. and Kou, S. (2000) "Experiments to simulate effect of Marangoni convection on weld pool shape," Welding Journal, 79:8:231s-237s

[24] Chakraborty, N. and Chakraborty, S. (2005) "Influences of sign of surface tension coefficient on the turbulent weld pool convection in a gas tungsten arc welding (GTAW) process: A comparative study," J. Heat Transfer, 127:848-862

[25] Lu, S. P., Fujii, H., Sugiyama, H., Tanaka, M. and Nogi, K. (2002) Mater. Trans., 43:2926

[26] Lu, S. P., Fujii, H., Sugiyama, H. and Nogi, K. (2003) Metall. Mater. Trans. A, 34:1901

[27] Lu, S. P., Fujii, H. and Nogi, K. (2004) "Marangoni convection and weld shape variation in Ar-$O_2$ and Ar-$CO_2$ shielded GTA welding," Mater. Sci. Engg. A, 380:290-297

[28] Lu, S. P., Fujii, H. and Nogi, K. (2004) "Sensitivity of Marangoni convection and weld shape variations to welding parameters in $O_2$-Ar shielded GTA welding," Script. Mater. 51:271-277

[29] Lu, S. P., Fujii, H. and Nogi, K. (2004) "Marangoni convection in weld pool in $CO_2$-Ar-shielded Gas Thermal Arc Welding," Metall. Mater. Trans., 35A:2861-2867

[30] Wei, P. S., Yeh, J. S., Ting, C. N., Debroy, T., Chung, F. K. and Lin, C. L. (2009) "The effects of Prandtl number on wavy weld boundary," Int. J. Heat Mass Transfer, 52:3790-3798

[31] Sen, A. K. and Davis, S. H. (1982) "Steady thermocapillary flows in two-dimensional slots," J. Fluid Mech., 121:163-186

[32] Lucas, W. and Howse, D. (1996) "Activating flux – increasing the performance and productivity of the TIG and plasma processes," Weld. Metal Fabrication, 64:1:11-17

[33] Modenesi, P. J., Apolinario, E. R. and Pereira, I. M (2000) "TIG welding with single-component fluxes," J. Mater. Proc. Tech., 99:260-265

[34] Lu, S., Fujii, H., Sugiyama, H. and Nogi, K. (2003) "Mechanism and optimization of oxide fluxes for deep penetration in GTAW," Metall. Mater. Trans. A, 34A:1901-1907

[35] Savitskii, M. M. and Leskov, G. I. (1980) "The mechanism of the effects of electrically negative elements on the penetration power of an arc with a tungsten cathode," Avtom Svarka, 9:17-22

[36] Simonik, A. G. (1976) "The effect of contraction of the arc discharge upon the introduction of electro-negative elements," Svar. Proiz., 3:49-51

[37] Howse, D. S. and Lucas, W. (2000) "Investigation into arc constriction by active fluxes for TIG welding," Sci. Tech. Weld. Joining, 5:189-193

[38] Lowke, J. J., Tanaka, M. and Ushio, M. (2005) "Mechanisms giving increased weld depth due to a flux," J. Phys. D: Appl. Phys., 38:3438-3445

[39] Zhang, R. H. and Fan, D. (2007) "Numerical simulation of effects of activating flux on flow patterns and weld penetration in A-TIG welding," Sci. Tech. Weld. Joining, 12:1:15-23

[40] Xu, Y. L., Dong, Z. B., Wei, Y. H. and Yang, C. L. (2007) "Marangoni convection and weld shape variation in A-TIG welding process," Theo. Appl. Frac. Mech.

[41] Lu, S., Fujii, H. and Nogi, K. (2008) "Marangoni convection and weld shape variations in He-$CO_2$ shielded GTAW on SUS304 stainless steel," J. Mater. Sci., 43:4583-4591

[42] Lu, S., Dong, W., Li, D. and Li, Y. (2009) "Numerical study and comparisons of gas tungsten arc properties between argon and nitrogen," Comp. Mater. Sci., 45:327-335

[43] Domey, J., Aidun, D. K., Ahmadi, G., Regel, L. L. and Wilcox, W. R. (1995) "Numerical simulation of the effect of gravity on the weld pool shape," Weld. J., 74:8:263s-268s

[44] Kou, S. (2002) "Welding Metallurgy," Second Ed., John Wiley & Sons Publication

[45] Kim, W. H., Fan, H. G. and Na, S. J. (1997) "Effect of various driving forces on heat and mass transfer in arc welding," Numerical Heat Transfer A:Appli., 32:633-652

[46] Friedman, E. (1978) "Analysis of weld puddle distortion and its effect on penetration," weld. J., 57:161s-166s

[47] Choo, R. T. C., Szekely, J. and Westhoff, R. C. (1990) "Modeling of high current arcs with emphasis on free surface phenomena in the weld pool," Weld. J., 69:346s-361s

[48] Lin, M. L. and Eagar, T. W. (1983) "Influence of surface depression and convection on arc weld pool geometry," Trans. ASME, Transport Phenomena in Materials Processing, 10:63s-69s

[49] Wu, C. S. and Dorn, L. (1995) "Prediction of surface depression of a TIG weld pool in the full-penetration condition," Proc. Inst. Mech. Engg., 209:221-226

[50] Zhang, Y. M., Cao, Z. N. and Kovacevic, R. (1996) "Numerical analysis of fully penetrated weld pools in GTAW," Proc. Inst. Mech. Engg., 210:187-195

[51] Kim, S. D. and Na, S. J. (1994) "A study on the three-dimensional analysis of heat and fluid flow in GMAW using boundary-fitted coordinates," Trans. ASME, J. Engg. Industry, 116:2:78-85

[52] Rokhlin, S. I. and Guu, A. C. (1993) "A study of arc force, pool depression, and weld pool penetration during GTAW," Weld. J., 72:8:381s-390s

[53] Fan, H. G., Tsai, H. L. and Na, S. J. (2001) "Heat transfer and fluid flow in a partially or fully penetrated weld pool in GTAW," Int. J. Heat Mass Trans., 44:417-428

[54] Ko, S. H., Choi, S. K. and Yoo, C. D. (2001) "Effects of surface depression on pool convection and geometry in stationary GTAW," Welding Journal, 80:2:39s-45s

[55] Wu, C. S., Zhao, P. C. and Zhang, Y. M. (2004) "Numerical simulation of transient 3-D surface deformation of a completely penetrated GTA weld," Weld. Research, 330s-335s

[56] Wu, C. S., Zhao, P. C. and Zhang, Y. M. (2005) "Modeling the transient behaviors of a fully-penetrated GTA weld pool with surface deformation," Proc. IMechE B: J. Engg. Manuf., 219:99-110

[57] Hsu, K. C., Etemadi, K. and Pfender, E. (1982) "Study of the free-burning high-intensity argon arc," J. Appl. Phys., 54:3:1293–1301

[58] McKelliget, J. and Szekely, J. (1986) "Heat transfer and fluid flow in welding arc," Metall. Mater. Trans. A, 17:7:1139–1148

[59] Choo, R. T. C., Szekely, J. and Westhoff, R. C. (1992) "On the calculation of the free surface temperature of Gas-Tungsten-Arc Weld pools from first principles: Part I. Modeling the welding arc," Metall. Mater. Trans. B, 23B:357–369

[60] Lee, Y. S. and Na, S. J. (1996) "Numerical analysis of a stationary gas tungsten welding arc considering various electrode angles," Weld. J., 75:9: 269–279

[61] Goodarzi, M., Choo, R., Takasu, T. and Toguri, J. M. (1998) "Effect of the cathode tip angle on the gas tungsten arc welding arc and weld pool: II. The mathematical model for the weld pool," J. Phys. D: Appl. Phys. 31:5:569-583

[62] Fan, H. G. and Shi, Y. W. (1996) "Numerical simulation of the arc pressure in gas tungsten arc welding," J. Mater. Process. Tech. 61:3:302–308

[63] Kim, W. H., Fan, H. G. and Na, S. J. (1997) "Mathematical model of gas tungsten arc welding considering the cathode and the free surface of the weld pool," Metall. Mater. Trans. B, 28:4:679-686

[64] Ramirez, M. A., Trapaga, G. and McKelliget, J. (2003) "A comparison between two different numerical formulations for welding arc simulation," Modeling Simul. Mater. Sci. Eng., 11:675-695

[65] Lee, J. H., Cho, Y. T. and Na, S. J. (2002) "A numerical analysis of a GTAW considering the current density and temperature distribution on the electrode surface," Proc. Inst. Mech. Engg., 216:1115-1121

[66] Fan, H. G., Na, S. J. and Shi, Y. W. (1997) "Numerical simulation of current density in GTAW including the influence of the cathode," Proc. Inst. Mech. Engg., 211:321-327

[67] Cantin, G. M. D. and Francis, J. A. (2005) "Arc power and efficiency in GTAW of aluminum," Sci. Tech. Weld. Joining, 10:2:200-210

[68] Lawson, W. H. S. and Kerr, H. W. (1976) "Fluid motion in GTA weld pools – 1. Flow patterns and weld pool homogeneity," Welding Research International, 6:5:63-77

[69] Lawson, W. H. S. and Kerr, H. W. (1976) "Fluid motion in GTA weld pools – 2. Weld Pool Shapes," Welding Research International, 6:6:1-17

[70] Lin, M. L. and Eagar, T. W. (1985) "Influence of arc pressure on weld pool geometry," Welding Journal, 64:6:163s-169s

[71] Dong, W., Lu, S., Li, D. and Li, Y. (2009) "Numerical study for GTA weld shape variation by coupling welding arc and weld pool," Int. J. Modern Phys. B, 23:6,7:1597-1602

[72] Choo, R. T. C., Szekely, J. and David, S. A. (1992) "On the calculation of the free surface temperature of Gas-Tungsten-Arc Weld pools from first principles: Part II. Modeling the welding pool and comparison with experiments," Metall. Trans. B, 23B:371-384

[73] Tanaka, M., Terasaki, H., Ushio, M. and Lowke, J. J. (2002) "A unified numerical modeling of stationary tungsten-inert-gas welding process," Metall. Mater. Trans. A, 33A:2043-2052

[74] Ushio, M., Tanaka, M. and Lowke, J. J. (2004) "Anode melting from free-burning argon arcs," IEEE Trans. Plasma Sci. 32:1:108-117

[75] Yamamoto, K., Tanaka, M., Tashiro, S., Nakata, K., Yamazaki, K., Yamamoto, E., Suzuki, K. and Murphy, A. B. (2008) "Numerical simulation of metal vapor behavior in arc plasma," Surf, Coat. Tech. 202:5302-5305

[76] Dong, W., Lu, S., Li, D. and Li, Y. (2009) "Numerical study for GTA weld shape variation by coupling welding arc and weld pool," Int. J. Modern Phys. B, 23:6,7:1597-1602

[77] Lu, S. P., Dong, W. C., Li, D. Z. and Li, Y. Y. (2009) "Numerical simulation for welding pool and welding arc with variable active element and welding parameters," Sci. Tech. Weld. Joining, 14:6:509-516

[78] Chakraborty, N., Chakraborty, S. and Dutta, P. (2002) "Modeling of turbulent transport in arc welding pools," Int. J. Num. Meth. Heat and Fluid Flow, 13:1:7-30

[79] Chakraborty, N., Chakraborty, S. and Dutta, P. (2004) "Three-dimensional modeling of turbulent weld pool convection in GTAW processes," Num. Heat Transfer A, 45:391-413

[80] Zacharia, T., David, S. A., Vitek, J. M. and Debroy, T. (1989) "Weld pool development during GTA and laser beam welding of type 304 stainless steel part I. Theoretical analysis," Welding Journal, 68:12:499s-509s

[81] Zacharia, T., David, S. A., Vitek, J. M. and Debroy, T. (1989) "Weld pool development during GTA and laser beam welding of type 304 stainless steel part II. Experimental correlation," Welding Journal, 68:12:510s-519s

[82] Mishra, S. and Debroy, T. (2005) "A heat-transfer and fluid-flow-based model to obtain a specific weld geometry using various combinations of welding variables," J. Applied Physics, 98:4:44902-1-10

[83] Zhang, W., Roy, G. G., Elmer, J. W. and Debroy, T. (2003) "Modeling of heat transfer and fluid flow during gas tungsten arc spot welding of low carbon steel," J. Applied Physics, 93:5:3022-33

[84] Zacharia, T., T. David, S. A., Vitek, J. M. and Debroy, T. (1991) "Computational modeling of stationary gas-tungsten-arc weld pools and comparison to stainless steel 304 experimental results," Metall. Trans. B, 22,:2:243-257

[85] Thompson, M. E. and Szekely, J. (1989) "The transient behavior of weld pools with a deformed surface," Int. J. Heat Mass Transfer, 32:6:1007-1019

[86] Wu, C. S. and Yan, F. (2004) "Numerical simulation of transient development and diminution of weld pool in gas tungsten arc welding," Modeling Simul. Mater. Sci. Eng., 12:13-20

[87] Farzadi, A., Serajzadeh, S. and Kokabi, A. H. (2008) "Prediction of solidification behavior of the weld pool through modeling of heat transfer and fluid flow during GTAW of commercial pure aluminum," Mater. Sci. Tech., 24:12:1427-1432

[88] Aval, H. J., Farzadi, A., Serajzadeh, S. and Kokabi, A. H. (2009) "Theoretical and experimental study of microstructures and weld pool geometry during GTAW of 304 stainless steel," Int. J. Adv. Manuf. Tech., 42:1043-1051

[89] Hibbitt, H. D. and Marcal, R. V. (1973) "A Numerical Thermo-Mechanical Model for the Welding and Subsequent Loading of a Fabricated Structures," Comp. Struc., 3:1145–1174

[90] Lai, C. K. F., Koeing, H. A. and Morral, J. E. (1986) "Three Dimensional Thermal Stress Analysis of a Welded Plate by the FEM," Trans. CSME, 10:153–165

[91] Sheppard, S. D. (1990) Weld. Res. Council Bull., 356:34-41

[92] Sluzalec, A. (1990) "Thermal effects in friction welding." Int. J. Mech. Sci., 32:467-478

[93] Khandkar, M. Z. H. and Jamil, K. (2003) "Predicting residual thermal stresses in friction stir welding," ASME IMECE, 374:355-360, Washington, DC, Nov 15-21

[94] Lin, Y. C. and Lee, K. H. (1997) "Effect of preheating on the residual stress in type 304 stainless steel weldment," J. Mater. Proc. Tech., 63:797-801

[95] Yang, L. J. and Xiao, Z. M. (1995) "Elastic-plastic modeling of the residual stress caused by welding," J. Mater. Process. Technol., 48:589-601

[96] Canas, J., Picon, R., Paris, F., Blazquez, A. and Marin, J. C. (1996) "A simplified numerical analysis of residual stresses in aluminum welded plates," Computers and Structures, 58:1:59-69

[97] Goldak, J. A., Breiguine, V., Dai, N., Hughes, E. and Zhou, J. (1997) "Thermal stress analysis in solids near the liquid region in welds," Mathematical Modeling of Weld Phenomena by Cerjak, H., 3rd Ed., The Institute of Materials, pp543-570

[98] Oddy, A. S., Goldak, J. A. and McDill J. M. J. (1990) "Numerical analysis of transformation plasticity relation in 3D finite element analysis of welds," European J. Mechanics, A/Solids, 9:3:253-263

[99] Oddy, A. S., McDill, J. M. and Goldak, J. A. (1990) "Consistent strain fields in 3D finite element analysis of welds," J. Pressure Vessel Tech., 25:1:51-53

[100] Yuan, F. and Sun. H. (1991) "Transient temperature fields and residual stress fields of metallic materials under welding," Appl. Math. Mech., 12:595-599

[101] Murakawa, H., Luo, Y. and Ueda, Y. (1998) "Theoretical prediction of welding deformation at groove in narrow gap welding," ASM Proceedings of the Int. Conference: Trends in Welding Research, 993-998, Pine Mountain, GA

[102] Chidiac, S. E. and Mirza, F. A. (1993) "Thermal stress analysis due to welding processes by the finite element method," Comput. Struct., 46:407-412

[103] Sunar, M., Yilbas, B. S. and Boran, K. (2006) "Thermal and stress analysis of a sheet metal in welding," J Mater. Proc. Tech., 172:123-129

[104] Kong, F, and Kovacevic, R. (2010) "3D finite element modeling of the thermally induced residual stress in the hybrid laser/arc welding of lap joint," J. Mater. Proc. Tech., 210:941-950

[105] Goldak, J. A. and Akhlaghi, M. (2005) "Computational Welding Mechanics," Springer Inc.

[106] Voller, V. R. and Prakash, C. (1987) "A Fixed-Grid Numerical Modeling Methodology for Convection-Diffusion Mushy Region Phase-Change Problems," Int. J. Heat Mass Transfer, 30:1709-1720.

[107] Tsai, N. S. and Eagar, T. W. (1985) "Distribution of the heat and current fluxes in gas tungsten arcs," Metall. Trans. B, 16B:841-846.

[108] Bejan, A. (1995) Convective Heat Transfer, 2nd Ed., Wiley, New York

[109] Aboutalebi, M. R., Hassan, M. and Guthrie, R. I. L. (1995) "Numerical study of coupled turbulent flow and solidification for steel slab clusters," Numerical Heat Transfer, 28:279-299.

[110] Chen, T. F., Chen, Y. R. and Wu, W. (1998) "Properties of Cu-Si enriched type 304 stainless steel welds," Sci. Tech. Weld. Joining, 3:75-79

[111] Yan, J., Gao, M. and Zeng, X. (2010) "Study on microstructure and mechanical properties of 304 stainless steel joints by TIG, laser and laser-TIG hybrid welding," Opt. Lasers Eng., 48:512-517

[112] Muthupandi, V., Srinivasan, P. Bala, Seshadri, S. K. and Sundaresan, S. (2003) "Effect of weld metal chemistry and heat input on the microstructure and properties of duplex stainless steel welds," Mater. Sci. Eng., 358:9-16

[113] Jana, S. (1992) “Effect of heat input on the HAZ properties of two duplex stainless steels,” J. Mater. Proc. Tech., 33:247-261

[114] Nowacki, J. and Rybicki, P. (2005) “The influence of welding heat input on submerged arc welded duplex steel joints imperfections,” J. Mater. Proc. Tech., 164-165: 1082-1088

[115] Zumelzu, E., Sepulveda, J. and Ibarra, M. (1999) “Influence of microstructure on the mechanical behavior of welded 316L SS joints,” J. Mater. Proc. Tech., 94:36-40

[116] Durgutlu, A. (2004) “Experimental investigation of the effect of hydrogen in argon as a shielding gas on TIG welding of austenitic stainless steel,” Mater. Des., 25:19-23

[117] Lee, W. S., Tzeng, F. T. and Lin, C. F. (2005) “Mechanical properties of 304L stainless steel SMAW joints under dynamic impact loading,” J. Mater. Sci., 40:4839-4847

[118] Korinko, P. S. and Malene, S. H. (2001) “Considerations for the weldability of types 304L and 316L stainless steel,” Pract. Fail. Anal., 4:61-68

[119] Lee, D. J., Jung, K. H., Sung, J. H., Kim, Y. H., Lee, K.H., Park, J. U., et al. (2009) “Pitting corrosion behavior on crack property in AISI 304L weld metals with varying Cr/Ni equivalent ratio,” Mater. Des., 30:3269-3273

[120] Milad, M., Zreiba, N., Elhalouani, F. and Baradai, C. (2008) “The effect of cold work on structure and properties of AISI 304 stainless steel,” J. Mater. Proc. Tech., 203:80-85

[121] Shyu, S. W., Huang, H. Y., Tseng, K. H. and Chou, C. P. (2008) “Study of the performance of stainless steel A-TIG welds,” J. Mater. Eng. Perform., 17:193-201

[122] Kumar, S. and Shahi, A. S. (2011) “Effect of heat input on the microstructure and mechanical properties of gas tungsten arc welded AISI 304 stainless steel joints,” Mater. Des., 32:3617-3623

[123] Lumsden, J. B. and Stocker, P. J. (1981) “Composition of grain boundaries of type 304 stainless steel in low temperature sensitization condition,” Scr. Metall., 15:1295-1298

[124] Bruemmer, S. M. and Charlot, L. A. (1986) “Development of grain boundary chromium depletion in type 304 and 316 stainless steels,” Scr. Metall., 20:1019-1024

[125] Mozhi, T. A., Juhas, M. C. and Wilde, B. E. (1987) “Modeling low temperature sensitization of austenitic stainless steels,” Scr. Metall., 21:1547-1552

[126] Richard, J. and Valerie, R. (2010) “Sensitization behavior of grain boundary engineered austenitic stainless steel,” Mater. Sci. Eng. A, 527:4275-4280

[127] Lindgren, L. E. (2001) “Finite Element Modeling and Simulation of Welding. Part 1: Increased Complexity,” J. Thermal Stresses, 24:2:141-192

[128] Lindgren, L. E. (2001) “Finite Element Modeling and Simulation of Welding. Part 2: Improved Material Modeling,” J. Thermal Stresses, 24:3:195-231

[129] Sheng, I. C. and Chen, Y. (1992) “Modeling welding by surface heating,” J. Eng. Mater. Technol., 114:439-449

[130] Chen, Y. and Sheng, I. C. (1993) “On the solid-fluid transition zone in welding analysis,” J. Eng. Mater. Technol., 115:17-23

[131] Leblond, J. B. and Devaux, J. C. (1984) “A kinetic model for anisothermal metallurgical transformation in steels including effect of austenite grain size,” Acta Metall., 32:137-146

[132] Leblond, J. B., Mottet, G. and Devaux, J. C. (1986) “A theoretical and numerical approach to the plastic behavior of steels during phase transformations: I. Derivation of general relations,” J. Mech. Phys. Solids, 34:395-409

[133] Leblond, J. B., Mottet, G. and Devaux, J. C. (1986) “A theoretical and numerical approach to the plastic behavior of steels during phase transformations: II. Study of classical plasticity for ideal-plastic phases,” J. Mech. Phys. Solids, 34:411-432

[134] Oddy, A. S., Goldak, J. A. and McDill, J. M. (1990) “A general transformation plasticity relation for 3d finite element analysis of welds,” Eur. J. Mech. A-Solids, 9:253-263

[135] Oddy, A. S., Goldak, J. A. and McDill, J. M. (1992) “Transformation plasticity and residual stresses in single-pass repair welds,” J. Pressure Vessel Technol.-Trans. ASME, 114:33-38

[136] Ronda, J., Murakawa, H., Oliver, G. J. and Ueda, Y. (1995) “Thermo-mechano-metallurgical model of welded steel: II. Finite element formulation and constitutive equations,” Trans. JWRI, 14:1-21

[137] Kim, J. W., Im, S. Y. and Kim, H. G. (2005) “Numerical implementation of a thermo-elastic-plastic constitutive equation in consideration of transformation plasticity in welding,” Int. J. Plast., 21:1383-1408

[138] Deng, D. and Murakawa, H. (2006) “Prediction of welding residual stress in multi-pass butt-welded modified 9Cr-1Mo steel pipe considering phase transformation effects,” Comput. Mater. Sci., 37:209-219

[139] Lee, C. H. (2008) “Computational modeling of the residual stress evolution due to solid-state phase transformation during welding,” Modeling Simul. Mater. Sci. Eng., 16:1-16

[140] Lee, C. H. and Chang, K. H. (2009) “Finite element simulation of the residual stress in high strength carbon steel butt weld incorporating solid-state phase transformation,” Comp. Mater. Sci., 46:1014-1022

[141] Lindgren, L. E. (2007) "Computational Welding Mechanics (Thermomechanical and Microstructural Simulations)," First Ed., Woodhead Publishing.

[142] Kim, C. S. (1975) "Thermophysical Properties of Stainless Steel," Argonne National Laboratory, Report No. ANL-75-55.

[143] Deng, D. and Kiyoshima, S. (2010) "FEM Prediction of Welding Residual Stresses in a SUS304 Girth-Welded Pipe with Emphasis on Stress Distribution near Weld Start/End Location," Comput. Mater. Sci., 50:612-621.

[144] Dong, W., Lu, S., Li, D. and Li, Y. (2009) "Modeling of the Weld Shape Development During the Autogenous Welding Process by Coupling Welding Arc with Weld Pool," J. Mater. Engineering and Performance, 19:7:942-950.

[145] Lu, S. P., Fujii, H. and Nogi, K. (2005) "Influence of Welding Parameters and Shielding Gas Composition on GTA Weld Shape," ISIJ Intl., 45:66-70.

[146] Nestor, O. H. (1962) "Heat Intensity and Current Density Distributions at the Anode of High Current, Inert Gas Arc," J. Appl. Phys., 33:5:1638-1648.

# Vita

Debamoy Sen, son of Arun Kumar and Banani Sen, was born in Calcutta, India, on March 18, 1984. In August 2006, he received his B.Tech in Mechanical Engineering from West Bengal University of Technology, Calcutta, India. He joined Cognizant Technology Solutions in October 2006, as a Programmer Analyst, specializing in Object Oriented Programming. He received certifications from Cognizant in Java and SQL 8i. He also earned a Sun Certified Java Programmer certification.

In August 2007, he joined the Mechanical and Aerospace Engineering Department at the Missouri University of Science and Technology, Rolla, MO, USA, as a graduate research assistant under Dr. K. M. Isaac. In August 2009, he received his M.S. degree, specializing in Computational Fluid Dynamics. His thesis was titled "Modeling and Numerical Simulation of Electrochemical Magnetohydrodynamics". His pioneering work reproduced the electrochemical Cyclic Voltammograms for the first time through CFD simulations. His M.S research contributed to three conference and one journal publication.

After earning his Masters, he joined the Mechanical Engineering Department at Virginia Tech for his doctoral degree in August 2009. His doctoral work has resulted in five conference proceedings and has two journal articles submitted for review. This dissertation represents the culmination of his research conducted while enrolled at Virginia Tech. While at Virginia Tech, he undertook a 7-month co-op in the Advanced R&D group at Volterra Semiconductor Corp., Fremont, CA as a System Design Engineer intern. His work involved thermal design/optimization of integrated QFN and CSP voltage regulators using chip, board and system level thermal simulations. After graduation, he is scheduled to join the same group as a Sr. Thermal Engineer.